1-1-2007

Wrinkling failure of steel pipelines under monotonic load and deformation.

Yonghong Zhang
University of Windsor

Wrinkling Failure of Steel Pipelines under Monotonic Load and Deformation

by Yonghong Zhang

A Thesis
Submitted to the Faculty of Graduate Studies and Research
Through
The Department of Civil and Environmental Engineering
in Partial Fulfillment of the Requirements for
the Degree of Master of Applied Science at the
University of Windsor

Windsor, Ontario, Canada

January, 2007

Your file Votre référence
ISBN: 978-0-494-42307-3
Our file Notre référence
ISBN: 978-0-494-42307-3

ABSTRACT

The objective of this study was to determine failure conditions and failure modes of energy pipelines when subjected to axi-symmetric axial monotonic load and deformation. This study involved three components: (i) development of finite element models, (ii) determination of a fracture failure criterion, and (iii) conduction of detailed parametric study to determine the influence of parameters: (a) internal pressure, (b) diameter to thickness ratio, and (c) material behavior on failure conditions and failure modes.

This thesis discusses the development and calibration of the finite element models and the data obtained from all the parametric studies. The finite element model was validated using tests data. The fracture failure criterion for the pipe specimens was derived based on a shear failure model. It was found that the failure conditions and failure modes of the energy pipelines depend largely on internal pressure, diameter to thickness ratio, and the ductility of the material.

ACKNOWLEDGEMENTS

I would like to thank Dr. Sreekanta Das for supervising me for the study. I also thank to Dr. Murty Madugula for his assistance.

I must acknowledge the financial assistance and scholarship that I received from the Department of Civil and Environmental Engineering and the Faculty of Graduate Studies and Research of the University of Windsor.

At last, I would like to thank especially to my husband, Guangqian, and my two little sons, Raymen and Cary. Without their love and support, I would never be able to successfully finish the journey of the study.

TABLE OF CONTENTS

LIST OF TABLES

LIST OF FIGURES

LIST OF SYMBOLS

Latin Symbols

A	Current area on the shell's reference surface
A_o	Original area on the shell's reference surface
A_s	Pipe steel cross sectional area
D	Pipe nominal diameter; Outside pipe diameter in Chapter 2; Mid-thickness diameter in Chapter 6
D/t	Diameter over thickness ratio
E	Young's modulus
E_s	Modulus of elasticity
F_{xc}	Mean axial compression load
F_y	Yield load
f_y	Yield stress of the pipe material
{F}	Vector of applied loads
$\{F_i^{In}\}$	Structure's internal force
h	Overclosure of the surfaces (the interpenetration of the surfaces)
i	Subscript representing the current equilibrium iteration
k	Strength coefficient
K]	Stiffness matrix
$\lfloor K_i^T \rfloor$	Stiffness matrix
$[K^T]^{-1}$	Invert tangent stiffness matrix
L	Original length of the pipe specimen
L_{ex}	Original length of the extensometer
M_c	Characteristic bending moment value
N	Axial load
n	Strain hardening exponent
Ny	Axial force correspondent to the yield stress
P	Maximum external pressure in Chapter 2; internal pressure in Chapter 6
P/Py	Internal pressure ratio
p_c	Contact pressure between two surfaces at a point
P_i	Maximum internal design pressure in Chapter 2;internal pressure in Chapter 3
P_e	Minimum external hydrostatic pressure in Chapter 2; Compensating compressive axial force on the end plates in Chapter 3
P_{max}	Maximum MTS load

P_{MTS}	Axial load through MTS P_{MTS}
P_t	Compressive force to simulate a temperature differential
P_y	Internal pressure causing yielding in the circumferential direction of the pipe
P_υ	Tensile axial load in the pipe wall due to the Poisson ratio effect
$\{R_i\}$	Force residual for the iteration
r_i	Internal radius of the pipe
t	Thickness of the pipe wall ; Current shell section thickness in Chapter 3
t_o	Original shell section thickness
t_2	Pipe wall thickness except for pressure containment resistance
$\{u\}$	Vector of DOF (degree of freedom) values
u_x, u_y, u_z	Translational degrees of freedom about three axes (x, y, z)

Greek Symbols

ΔL	Change in the length of the pipe specimen
ΔL_{ex}	Change in the length of the extensometer
ΔT	Temperature difference
α	Coefficient of thermal expansion
α_{gw}	Girth weld factor
α_h	Maximum allowed yield to tensile ratio
ϕ_{sc}	Resistance factor for compressive strain
ε_b	Bending strain
ε_{bc}	Characteristic bending strain
ε_c	Critical strain
ε_c^{crit}	Ultimate compressive strain capacity of the pipe wall
ε_{ex}	Extensometer strain
ε_f	Factored compressive strain in the longitudinal of hoop direction
ε_g	Global strain or overall strain
$\bar{\varepsilon}^{pl}$	Equivalent plastic strain

$\dot{\bar{\varepsilon}}^{pl}$	Equivalent plastic strain rate
$\bar{\varepsilon}_0^{pl}$	Initial equivalent plastic strain
$\bar{\varepsilon}_f^{pl}$	Logarithmic strain
$\bar{\varepsilon}_{\max}^{pl}$	Maximum equivalent plastic strains
$\bar{\varepsilon}_{C\max}^{pl}$	Maximum equivalent plastic strain at contact
ε_{nom}	Nominal stress or engineering stress
$\Delta\bar{\varepsilon}^{pl}$	An increment of the equivalent plastic strain
$\sum\Delta\bar{\varepsilon}_{pl}$	Summation of increment of the equivalent plastic strain
$\max\bar{\varepsilon}_f^{pl}$	Maximum equivalent plastic strain at failure
η	Usage factor
$\theta_x, \theta_y, \theta_z$	Rotational degrees of freedom about three axes (x, y, z)
μ	Friction coefficient
σ_e	Equivalent stress
σ_h	Hoop stress
σ_l	Longitudinal stress
σ_{nom}	Nominal stress or engineering stress
σ_{true}	True stress
σ_y	Yield stress of the pipe material
τ_1, τ_2	Two orthogonal components of shear stress
τ_c	Characteristic torsion sheer stress
τ_{crit}	Critical stress
τ_{eq}	Equivalent frictional stress
υ	Poisson's ratio
ω	Damage parameter

1 INTRODUCTION

Energy and energy industry plays important role in our economy and energy has become the lifeblood of the economy. The demands of more energy resource such as oil and natural gas initiates exploiting and developing these reserves in very remote regions, especially in arctic and sub-arctic regions in northern Canada and United States. Transportation of these natural resources from their supply to demand safely, efficiently and cheaply is a critical and important issue. It is now well accepted that the use of steel pipelines is the safest, most reliable, and most cost-effective way of transporting the large amounts of oil and natural gas that must be moved around world each day.

In Canada, almost all of Canada's crude oil and natural gas production makes all or part of its journey to market by pipeline, and most of these pipelines are buried underground. Canada has nearly 700,000 kilometers of underground pipeline that transport virtually all the country's daily crude oil and natural gas production to consumers in Canada and the United States (CERI 2001, PCF 2000). Parts of these buried pipelines are in north Canada, permafrost area. The pipeline segments in these areas are subjected to more severe load and/or deformation conditions. These load conditions usually are various combinations of axial force, internal pressure and bending moment.

The internal pressure is cause by the action of the fluid that the pipeline carries inside. Because of the internal pressure, the pipeline tends to expand in circumferential direction and cause the circumferential tensile stress, called hoop stress. The hoop stresses are permitted to develop about 80% of SMYS (Specified Minimum Yield Strength) in today's pipeline (CSA-Z662-03). Thus, the maximum internal pressure in the oil and gas pipeline is controlled by the maximum hoop stress permitted.

The axial loads acting on pipe segment come from several sources. One source of these axial loads is from the thermal effects caused by construction and operation temperature differential. In order to achieve high flow rates in pipelines, the pipeline is always operated in temperature and internal pressure as high as it permitted. Pipelines are

normally laid with near zero axial loads, at the temperature of the environment. In the north Canada, pipelines are usually laid during winter months at a of -30°C, when the ground is frozen and could support the heavy equipments required for installation, while the typical pipeline operation temperature is +15°C. The typical differential temperature between the installation and operation is approximately +45°C. When the pipeline is heated, it will try to expand. However, it is constrained by geotechnical factors, such as soil friction for buried pipeline or structural factors within the pipeline system such as compression station and neighboring pipe segments and inducing compressive axial forces in the pipe.

The Poisson's ratio effect also cause axial load. Because of the Poisson's ratio effect, the pipeline attempts to shorten in longitudinal direction when it subjects to the circumferential hoop stress. However, the pipeline shortening is prevented by the same restriction factors as discussed in previous section. As a result, tensile axial forces are introduced in the pipe.

Besides of axial force and internal pressure, another load condition often found on buried pipelines is bending caused by geotechnical movements. These geotechnical movements may results from actions such as slope movements, frost heave, and discontinuous permafrost, etc. These geotechnical movements often impose displacement on pipeline resulting beam bending, inducing compressive longitudinal strains on the concave side of the bends.

These loads and/or various combinations of these loads would result in global buckling or local buckling in the pipeline. These buckling causes development of large stresses and stains in the pipe wall, and this may affect the integrity and safety of the pipeline. A more detailed description on the concept of global and local buckling is discussed in Chapter 2.

1.1 STATEMENT OF PROBLEM

During last 30 years, significant researches have been undertaken to understand the behavior of buried pipelines under theses load conditions and combinations. Most of these studies were directed towards the understanding of mechanics behind initiation and stable growth of wrinkles. A few studies have also been undertaken to understand the post-wrinkling behavior and ultimate failure either due to excessive deformation or due to formation of fracture (Das *et al.* (2002)).

The wrinkle in those studies can use the definition by Souza *et al.* (1999) "a wrinkling is a local buckle of large amplitude that is clearly visible to the naked eye and possesses the following attributes: (i) its wave form is localized and restricted to approximately a single half-wave, or similar primitive shape; (ii) it is formed from plastic deformation; and (iii) the amplification of the single primitive wave form occurs coincidently with softening".

As stated above, the current wrinkle investigated usually is half-wave, and the correspondent analytic and experimental researches were also mostly carried out by this stage. The design failure criteria for local buckling or wrinkling are often coped with permitting magnitude of the deformation that can occur, such as limit strain or critical buckling strain, defined as the stain occurred in the pipe wall at the onset of the buckling.

Experimental study by Das *et al.* (2002) on X52 (SMYS of 358 MPa or 52 ksi) grade steel pipe with D/t of 45 shows that this pipe specimen is highly ductile and does not fail in fracture when it is subjected to monotonically increasing axi-symmetric compressive axial deformation with constant internal pressure. Instead, an accordion type (formation of multiple wrinkles in a short distance) of local buckling failure is expected to occur. This type of deformation failure may not pose any threat to the pipeline operation. However, this type of failure may introduce difficulty in operating inspection and cleaning tools (such as GeoPig or SmartPig) inside the pipeline, and it may also act as the initiation point for more catastrophic failures. Observation by Das *et al.* (2002) is based on two full scale tests on a specific pipe type and thus, it may not be prudent to make a

conclusion based on their study that other energy pipelines with various operating fluid pressure will also behave same way and fail same way. Thus, this study was initiated to find a reasonable answer to this question.

The experimental method is undoubtedly the most reliable method to investigate the post buckling behavior of wrinkled energy pipes subjected to axi-symmetric axial load and deformation. However, experimental method is expensive and time consuming and thus, experimental method becomes unviable and unrealistic for a situation when a parametric study on large number of test specimens is required. Experimental method also becomes less preferred when detailed information on how the pipe wall folding inside the pipe and when monitoring of strain history for locations on inside wall of the pipe is necessary. In this situation, numerical tools such as finite element (FE) method and analysis seems to be a better choice. However, complete elimination of experimental method may never be possible since FE models need to be validated and this can be done using test results from experimental study.

1.2 OBJECTIVES AND SCOPES

This project was initiated and designed to address the concerns identified in Section 1.1 and find an acceptable solution that the pipeline industry is able to use for making an informed decision on when a wrinkled pipeline under axi-symmetric axial deformation needs to be repaired to avoid the problem of inspection and cleaning inside the pipeline, loss of pipeline integrity, and occurrence of any subsequent environmental disaster Thus, the objective of the current study is to determine the following information.

1. Dependence of type of failure (accordion or others such as rupture in the pipe wall) on the operating internal pressure of the fluid.

2. Dependence of type of failure (accordion or others such as rupture in the pipe wall) on the D/t ratio, and

3. Dependence of type of failure (accordion or other such as rupture in the pipe wall) on material behavior of pipe steel.

A detailed parametric study using FE method has been conducted to accomplish the objectives of this research project. A general purpose FE code, ABAQUS/Standard and ABAQUS/Explicit, version 6.6-2 (ABAQUS (2006)) has been used for modeling and parametric study. The FE models for pipe analyses and coupon material analyses have been validated using the test data that were obtained from two full-scale tests and coupon laboratory tests by Das *et al.* (2002), respectively.

1.3 ORGANIZATION OF THESIS

The reminder of this thesis consists of several chapters. Chapter 2 presents the literature review on the current design guidelines and practices for local and global buckling and studies on this area that have been undertaken by other researchers. Chapter 3 describes the development of a FEA model to simulate the accordion type local buckling. Chapter 4 describes the validation the developed FEA model by using the collected experimental data. Chapter 5 describes the coupon material tests and numerical analyses to obtain the material properties. Chapter 6 performs parametric study using validated FEA model and failure criterion obtained from coupon numerical analyses. Chapter 7 is the summary, conclusion of this report.

2 LTERATURE REVIEW

This chapter provides literature and recommendations provided by various design standards on both global buckling and local buckling behavior of onshore energy pipelines. However, main focus of literature review is on deep understanding of formation and ultimate behavior of local buckling (wrinkling) in the pipe wall. From the following section, it can be seen that the current design standards /codes are revised based on most current researches to meet the demand of more effective and economic design, operation, and maintenance. Although the stress based design philosophy is still dominated in pipe design, a more unconservative strain based design concepts have been included in some design standards and already been used in real practices. Numerous researches have been conducted to investigate the capacity of the pipes subjected to different loads and its combinations. As a result, current design standards have been updated to a more reasonable level. It is generally accepted that the current design standards are conservative, Vitali, L. *et al.* (2005), however suggested that the Norway design standard (DVN-OS-F101-2000) critical strain formula may be non-conservative in some cases as sufficient experimental tests and numerical studies are not yet available. It is noticed that majority of recent research concentrates on behavior in strain hardening and stable post-buckling behavior and no specific attention has been paid to ultimate post-buckling behavior (Das *et al.* (2002)).

2.1 CURRENT DESIGN STANDARDS/CODES

In order to fully understand the current design criteria regarding pipeline integrity, five design standards from four countries/organizations are reviewed. They are: (1) DVN-OS-F101: Offshore Standard for Submarine pipeline system published in 2000 and amended latest in October 2005 by Det Norske Veritas, Norway, (2) PD 8010-1: Code of Practice for Pipelines, Part 1, Steel pipelines on land published in 2004 by British Standards Institution, (3) ASME B31.8: Gas transmission and distribution piping systems by American Society of Mechanical Engineering published in 2003, (4). ASME B31.4: Pipeline transportation system for liquid hydrocarbons and other liquids by American

Society of Mechanical Engineering published in 2002, and (5) CSA-Z662-03, Oil and Gas Pipeline Systems by Canadian Standards Association published in 2003.

It can be seen that, at present safe and conservative methodologies, the stress-based design methods are still widely used in pipeline design. However, their counterparts strain-based design methods which use strain limits to take the advantage of steel's well-known ability to deform plastically, but remain a stable structure are being used increasingly in pipeline design. A list of recent pipelines that have used strain-based design is shown in Table 1. That list is only a small sample of the worldwide projects that have used strain-based design. Many current design standards have adopted strain-based design philosophy. DNV 2000 and PD8010-1 (2004), for example include requirements for both stress- and strain-based design, B31.8-2003 also allows strain-based design but do not provide extensive provisions related to strain-based design. Detail discussions are made next.

2.1.1 Norway Design Standard

DVN-OS-F101 in general provides design guidelines/recommendations for offshore pipelines. This standard is based on limit states design criteria. Section 5 Clause D100 recommends four various limit states need to be considered in pipeline design. These limit states are Serviceability Limit State (SLS), Ultimate Limit State (ULS), Fatigue Limit State (FLS) and Accidental Limit State (ALS). In SLS, ovalisation/ratcheting limit, accumulated plastic strain limit, and damage due to or loss of weight coating are considered; in ULS, bursting limit, ovalisation/ratcheting limit if causes total failure, local buckling limit (pipe wall buckling limit state), global buckling, unstable fracture and plastic collapse limit, and impact should be accounted while in FLS, fatigue due to cyclic loading and in ALS, ultimate limit due to infrequent loading must be checked.

DVN-OS-F101 design format is mainly based on Load and Resistance Factor Load (LRFD) format. It also provides an equivalent more conservative Allowable Stress Design (ASD) form in Section 12F. For control of local buckling, Section 5 Clause D 500

recommends three criteria: system collapse caused by external pressure, combined loads criteria, and buckling propagation should be fulfilled. Large accumulated plastic strain should be accounted since it may aggravate local buckling. Clause D 507 provides characteristic strain or critical strain ε_c for displacement controlled local buckling of pipe members subjected to longitudinal compression strain (bending moment and axial force) and internal overpressure. LRFD format relates to this critical strain ε_c value with local buckling is specified as:

$$\varepsilon_c = 0.78\left(\frac{t_2}{D} - 0.01\right)\left(1 + 5\frac{\sigma_h}{f_y}\right)\alpha_h^{-1.5}\alpha_{gw} \qquad (2.1)$$

where t_2 is pipe wall thickness except for pressure containment resistance, σ_h is hoop stress, f_y is the yield stress of the pipe material, α_h is maximum allowed yield to tensile ratio, and α_{gw} is girth weld factor, Clause 12 F900 proposes girth weld factor values for the pipes of *D/t* ranges between 0-60 based on the research results of Yoosef-Ghodsi *et al.* (1994) that girth weld has a significant impact on compressive strain capacity.

DNV-OS-F101 (Section 12 F 1200) also provides ASD format to check the local buckling in the early design stage for internal over pressure. The following stress conditions shall be satisfied:

$$\sigma_e \le \eta \times f_y \qquad (2.2)$$

$$\sigma_l \le \eta \times f_y \qquad (2.3)$$

where σ_e is the equivalent stress, σ_l is longitudinal stress, η is usage factor. However, ASD format does not supersede the LRFD format which shall be applied in final design. Adding moment factor shall also be considered when check local buckling according to Clause F 1300.

For global buckling, Section 5 Clause 600 gives guidelines for both load-controlled and displacement controlled global buckling conditions, although total failure caused by load-controlled buckling is not allowed.

DNV adopts strain based design format, LRFD format as the final design format for local buckling. It also adopts girth weld factor and material characteristic factor α_h in critical strain formula. However, initial imperfection and other factor such as residual stress are not accounted in this standard.

2.1.2 British Design Standard

British standard PD 8010-1-2004 adopts the allowable stress design criteria to design the pipe that hoop stress and equivalent stress should not exceed allowable hoop stress and allowable equivalent stress respectively that all are within the elastic range (Clause 6.4.2). For buckling, Clause 6.4.4 provides general guidelines on local buckling of the pipe, propagation buckling, global buckling, and ovality.

Clause H.1.2 to H.1.7 provides the detailed formulations on calculating characteristic load/strain values (critical loads/strain limits). The local buckling of the pipe wall will be avoided if the various loads the pipe is subjected are less than these characteristic values. Clause H.1.3 provides design criteria for pipe member under pure axial compression. If D/t is less than 60, local buckling does not occur until mean axial compression load, F_{xc}, reaches the yield load, F_y, as shown in the following equation.

$$F_{xc}=F_y=\pi\ (D-t)t\,\sigma_y \qquad (2.4)$$

where σ_y is the yield stress of the pipe material.

Clause H.1.4 gives formulation to calculate characteristic bending moment value M_c required to cause buckling when pipes are under pure bending and corresponding characteristic bending strain ε_{bc}. Clause H.1.6 provides equation for maximum external pressure P when external overpressure, compressive axial force and/or bending moment are acting together. Clause H.1.7 provides the equation for corresponding bending strain ε_b in the same load condition.Characteristic torsion sheer stress τ_c when torsion is acting alone is listed in Clause H.1.5. However, no limit is given in other load conditions or load combination. Clause H.3, and Clause H.4 provide guidance to calculation of upheaval buckling and ovalization respectively, no specific design limits is provided in this code.

It should be noticed that British standard PD 8010-1-2004 has terms for local buckling of the pipe due to external pressure, axial tension or compression, bending and torsion, or a combination of these loads. No particular rules in this standard consider the characteristic strain/load value when pipe is under load of internal pressure or combination of other loads with internal pressure.

2.1.3 American Design Standard

ASME B31.8 is a stress based code. Clause A842.2 defined the strength consideration during operations such that pipeline should design against excessive yielding, buckling, fatigue failure, ductile fracture, brittle fracture, loss of in-plane stability, propagating fracture, corrosion, collapse, and impacts. Formulae for allowable hoop stress, longitudinal stress, and combined stress are supplied, alternative design for strain is allowed, however, no specific formats are given. General guides for preventing bucking and ovalization, fatigue, and fracture are also listed.

ASME B31.4, similar to ASME, is also a stress based code. Clause 402.3 pertains to tress criteria in the design of piping systems within the scope of this code. These design criteria are given in form of limit stress formulations. General guidelines for fracture propagation in pipeline are also defined in Clause 402.5. Clause A402.3 provides allowable stress and other stress limits for offshore pipeline. Clause A402.3.4 gives the guidelines for allowable stress value, buckling, fatigue, fracture, loss of in-place stability, impact, residual stress and flexible pipe during installation and testing. Clause A402.3.5 provides strength criteria during operation, including allowable stress value, strain, buckling, fatigue, fracture, loss of in-place stability, and impact. Limit formulations for allowable hoop stress, longitudinal stress, and combined stress are specified in Clause A402.3.5 (a) allowable stress value while in Clause A402.3.4 (a) just general guidelines are given. In both Clause A402.3.4 (a) and A402.3.5 (a) allowable strain limits are mentioned to be alternative design method to allowable stress limits, although no detailed formulae are given. American Standard B31.4 mentioned that when the pipeline experiences a predictable noncyclic displacement of its support (e.g., fault movement

along the pipeline rout or differential subsidence along the line) or pipe sag before support contact, the longitudinal and combined stress limits may be replaced with an allowable strain limit, so long as the consequences of yielding do not impair the serviceability of the installed pipeline. The permissible maximum longitudinal strain depends upon the ductility of the material, any previously experienced plastic strain, and buckling behavior of the pipe.

2.1.4 Canadian Design Standard

Canadian standard CSA-Z662-03 adapts both stress based and strain based design criteria in its recommends limit states design methods. In Clause C3.4, Limit states are grouped into two major categories: ultimate limit states and serviceability limit states. Ultimate limit states are concerned with burst or collapse of the pipeline; serviceability limit states are concerned with excessive deformation restricting flow or pigging operation or local damage affecting the long-term durability of the pipeline. Rupture and local buckling use limit strain criteria while yielding uses limit stress criteria.

Clause C6.3.3 provides detail design limits to prevent local buckling for combined loads in terms of compression strain limits.

$$\phi_{sc}\varepsilon_c^{crit} \geq \varepsilon_f \tag{2.5}$$

where ϕ_{sc} is resistance factor for compressive strain, ε_c^{crit} is ultimate compressive strain capacity of the pipe wall, and ε_f is factored compressive strain in the longitudinal of hoop direction. The ultimate longitudinal compressive strain shall be the strain that is coincident with the attainment of peak load capacity of the member. The equation for ε_c^{crit} is:

$$\varepsilon_c^{crit} = 0.5\frac{t}{D} - 0.0025 + 3000\left(\frac{(p_i - p_e)D}{2tE_s}\right)^2 \tag{2.6}$$

where t is the pipe wall thickness, D is outside pipe diameter, P_i is maximum internal design pressure, P_e is minimum external hydrostatic pressure, and E_s is modulus of elasticity, taken as 207000MPa.

CSA-Z662-03 considering for local buckling, compressive strain limit is defined for axial force, bending, and internal pressure, no other load situation is considered. The internal pressure is actually the difference of internal pressure and external pressure, $(P_i - P_e)$. The ultimate strain or the critical strain is taken at the critical point when peak load attains. This critical point is the most arguable point because where it should be taken significantly affects the value of the critical strain. The soften point of the pipe material is somehow more reasonable than limit points based on results of some researchers, for example Yoosef-Ghodsi *et al.* (1995), Murray (1997) which will present in following seciton . Another noticeable fact is that current Canadian standard does not take account of girth weld factor.

2.2 GLOBAL BUCKLING

Global buckling is the restrained pipe buckling due to axial compressive forces induced by high operation temperatures, pressure, and/or geotechnical reasons, (DVN (2000)). This type of buckling is also sometimes referred to as Euler buckling. When a pipeline is operated at high internal pressure and high temperature, it will attempt to expand for positive differential temperature. However, the pipe is not free to move because of the plane strain constrains in the longitudinal direction and soil friction effect. This causes an axial compressive load and when this load reaches the critical value the pipe may experience vertical (upheaval buckling) or lateral (snaking buckling) as show in Figure 2.1 and Figure 2.2. The buckling is accelerated due to the presence of the initial imperfections. In particular, upheaval buckling occurs in buried pipelines whereas snaking buckling occurs in above ground pipelines.

Since the early eighties, a series of theoretical analysis by Hobbs (1981, 1984), Taylor and Ben Gan (1986) has proposed analytical tools to predict the occurrence and the

consequence of in-service global buckling. In early nineties, numerical models started to take place of the analytical tool to solve buckling problems since nonlinear analysis is required to account for the nonlinear state of stress. In the following subsection, research in the area of numerical modeling is reviewed.

Yoosef-Ghodsi *et al.* (2002) developed a two-dimensional, numerical model for the analysis of pipelines under various loading conditions, and, in particular, under thermal loading. Finite element model features a new elastic-plastic, isoparametric C^1 beam element capable of modeling large displacements and finite strains using an updated Lagrangian Formulation. This numerical model is able to handle highly irregular pipe and ground profiles in order to cover most practical cases. This finite element model was implemented in the computer program ABP (Analysis of Buried Pipelines) developed by Zhou and Murray (1993). This finite element model was verified through several examples by comparing the analytical results to those of closed-form solutions, experimental data, or other finite element programs. Finally, Application of the thermal analysis of this model was proved by three thermal buckling case studies. The first one was a parametric study with the initial out-of-straightness as the variant, the other two were stemmed from the investigations carried out on actual pipelines have the underground thermal buckling.

It is known that global buckling and local buckling is somewhat related, since local buckling sometimes is the results of the further deformation of the global buckling locally. This is evident in the recent studies conducted by Einsfield *et al.* (2003), and Song *et al.* (2003).

Einsfield *et al.* (2003) presented a numerical procedure for analysis of global and local buckling behavior of high temperature pressurized buried pipelines. This model provides an analysis tool to evaluate the susceptibility to buckling of pipeline under different load conditions. This technique consists of using a pipe-soil interaction formulation (named ABP program) for the determination of the global buckling configuration, and a commercially available FE code, ABAQUS, for local buckling evaluation. The pipe buckling is modeled by two anchor length segments and a buckling segment in the

middle of them (see Figure 2.3). The pipe-soil-slip occurred at the end of the anchor length segments due to a temperature change is solved by a closed-form differential equation. It was plotted in the form of end force vs. end axial displacement curve for certain temperature change (see Figure 2.4). The corresponding curve of internal resistance force vs. the shortening of the buckling segment is obtained by FE analysis while the peak load in the curve corresponds to the limit point for the initiation of the local buckling. By superimposing the two curves, it can be determined that the pipe will buckle locally if the point of intersection between the two curves locates in the ascending part of the latter curve, that is before the limit point, otherwise, only global buckling will occur. It was demonstrated that the buckling length and expected deformed post-buckling pipeline configuration were obtained with a good approximation using this model in a snaking buckling analysis.

Song *et al.* (2003) further validate the ability of the ABP program to model large displacement and finite strains particularly in global upheaval buckling by comparison the numerical solutions with Hobbs' (1984) differential equation solutions for pipeline upheaval buckling, and the differential equation solutions for pipe-soil slip mechanisms. Numerical analyses were carried out to investigate the upheaval and fracture phenomenon that occurred in a gas pipeline in Northern Alberta by using ABP program, a commercial code ABAQUS, and a spreadsheet for the pipe-soil slip mechanisms, based on the data in hand from the field. The numerical analysis procedure to determine the local behavior of pipes is similar to that conducted by Einsfield *et al.* (2003). The fracture simulation is based on the research by Das *et al.* (2002). Song *et al.* (2003) conducted the thermal cyclic analysis by using ABAQUS and estimated the number of cycles to cause the fracture failure of the pipe by using the formulae proposed by Das *et al.* (2002). A close agreement was got between the computed results and the events occurred at the fracture site.

2.3 LOCAL BUCKLING

In this section, literature on recent studies on local buckling behavior of the energy pipes is provided. These papers are discussed in four research groups: Canada, USA, Europe, and other areas.

Local buckling in this work indicts local buckling (wrinkling) in pipe wall either in an inward diamond shape or an outward bulge shape, see Figure 2.5 and Figure 2.6. Formation of local buckling (wrinkling) can occur under either a displacement controlled condition or load controlled condition. For a pipe bounded by the surrounding medium such as to prevent it from developing additional bending, other than that imposed by the boundaries, additional strains are fully controlled by the fixed geometry of external boundaries. This condition is usually classified as strain or displacement controlled. For a pipe free to bend under the action of external loads, the development of bending depends strictly on the capacity of internal stress to balance the external loads, and is controlled for internal actions within the elastic domain of the material behaviour. External loads, causing internal bending actions exceeding the elastic limit might cause unbounded deformations and the uncontrollable and non-localized achievement of failure conditions. This condition is usually classified as stress or Load Controlled (Bruschi *et al.* (2005)).

Local buckling is affected by several parameters, such as:

(a) Diameter over wall thickness (D/t) ratio
(b) Material stress-strain relationship
(c) Axial load ratio N/Ny (N is the axial force, Ny is the axial force correspondent to the yield stress)
(d) Internal pressure ratio P/Py (P is the internal pressure, Py is the internal pressure correspondent to a hoop stress equal to the yield stress)
(e) Welding (longitudinal as well as circumferential)
(f) Geometrical deviations e.g. initial out of roundness
(g) Reduction in wall thickness
(h) Cracks (in pipe and/or welding)

(i) Local stress concentration

(j) Additional loads and their amplitude

(k) Temperature

During last 30 years, many studies have been conducted to investigate local buckling behavior of pipes subjected to bending, axial load with or without internal pressure or combination of these loads. In the late seventies and early eighties, Bouwkamp and Stephen (1973), Sherman (1976) and Gresnight (1986) carried out a few experimental tests to investigate the buckling mechanism of pipes subject to combined loads. Subsequently Mohareb *et al.* (1993, 1994, and 2001), Yoosef-Ghodsi *et al.* (1995), DelCol *et al.* (1998), Smith, M. Q. *et al.* (1998), Dorey *et al.* (2002), carried out more experimental studies for better understanding buckling mechanism of the pipe, as well as the limit bending capacity and limit deformation of the pipes with or without girth, or corrosion of buried energy pipelines. Gresnigt *et al.* (2001) conducted experimental studies to investigate the effect of fabrication procedure on pipe strength capacity, Das *et al* (2002) determined the mechanism of pipe fracture of wrinkled pipe under load reversals, Yatabe *et al.* (2004) carried out experiments to investigate the strain-stress behavior and the pipe geometry on the deformability of high grade line pipe. Vitali *et al.* (2005) studied the strength capacity of the thick wall pipes. These will be discussed detailed later in this chapter.

Finite Element (FE) modeling and analysis have also been performed by investigators, such as Mohareb *et al.* (1993, 1994, 2001), Yoosef-Ghodsi *et al.* (1995), Souza *et al.* (1999),), DelCol, P. R. *et al.* (1998), Smith, M. Q. *et al.* (1998) , Hauch, S; Bai, Y (1998, 2000), Das *et al.* (2002) ,Vitali, L. *et al.* (1999, 2005), Dinovitzer, A *et al*, (2004). Torselletti, E. *et al.* (2005). These studies showed that FE analysis is capable of closely predicting the behaviour of the pipe wrinkling and post-wrinkling behavior subjected to various load conditions.

Research in local buckling area world wide can be grouped into to four regions, that are Canada, USA, Europe, and other areas.

2.3.1 Research in Canada

Mohareb *et al.* (1993, 1994, and 2001) conducted a series of seven full-scale tests to investigate the localized deformational behavior (wrinkle) of the plain pipe subjected to axial loads, internal pressure, and monotonically increasing curvature. Four NPS20 pipe (Nominal pipe size of 20 inch) specimens with nominal diameter of 508 mm , thickness of 7.9 mm and three NPS12 pipe (Nominal pipe size of 12 inch) specimens with nominal diameter of 324mm, thickness 6.4 mm were used. These pipe specimens had diameter-to-thickness ratios *D/t* of 64 and 51, respectively. All specimens had a length of 1690 mm. The settlement effects were considered by reactive case (the two ends of the specimens are fully constrained from moving in the axial direction due to high friction forces along pipe) and active case (the ends of the segments may move without altering the internal force at the segment boundaries when the friction forces along pipe are low). Five active tests and two reactive tests were performed. The internal pressures in the tests are of 0, 0.36, 0.72 and 0.80 Specified Minimum Yield Strength (SMYS), and these simulated zere pressure, medium pressure and maximum operation field pressure.

The experiment setup is shown in Figure 2.7. The free body diagram for loadings acting on the specimen is shown in Figure 2.8. Generally, the internal pressure and the axial load are keep constant throughout the test and the curvature is monotonically increased by controlling the displacements associated the eccentric jack. This rotated the loading arms at the top and bottom of specimen in responsible to viable, *F*. The similar experiment setups were also used by following researchers, such as, Yoosef-Ghodsi *et al.* (1995), DelCol *et al.* (1998), Dorey *et al.* (2001) and Das *et al.* (2002) to investigate the full size pipe specimen under combined loading.

Two distinct modes of local buckling, namely, a diamond shape mode and an outward bulging mode developed in the final post bulking shapes. The diamond shape mode occurred in the unpressured specimens while the outward bulging mode occurred in the all pressured specimens. Similar buckling shapes were also observed by Yoosef-Ghodsi

et al. (1995), Dorey *et al.* (2002), and Das *et al.* (2002). For fully pressured specimens, four to five buckling lobes were formed on the compression side of the pipe at onset buckling. As deformation increased, only one of the bulges progressed into a wrinkle while the other bulges decreased in amplitude and gradually disappeared. However, for the unpressured specimens, only one localized buckle (wrinkle) occurred and in the middle third of the specimen.

Finite element model using commercially available codes ABAQUS was developed to predict pipe deforming behavior. Comparison between the numerical analysis and experiment results showed that the finite element model was capable of reproducing the buckling modes and their location in 6 out of 7. Reasonable agreement is obtained in moment versus curvature for three unpressured pipe specimens, and better agreement is got in three pressured pipe specimens. However, one full pressured specimen could not get satisfied agreement because of the Bauschinger effect.

Yoosef-Ghodsi *et al.* (1995) tests the same number (seven) and size of specimens of full size line pipe as Mohareb *et al.* (1994) with addition of a girth-weld at mid-length, however, only in active condition. The specimens were subjected to constant axial force, constant internal pressure, and monotonically increasing curvatures. The tests set-up and procedure are identical to those used in plain pipe tests by Mohareb *et al.* (1994). The tests results show that the critical compressive strains (the strain when the wrinkle initiates and corresponding point in the moment-curvature curve is called softening point) of the girth-weld pipe were approximately 60% of those for plain pipe by Mohareb *et al.* (1994). The results also indicated the present accepted limits on pipe deformation appear to be conservative. It was found that end moment pass through a limit point (the point when the moment reaches its peak value) before it reach the softening point. So the limit point for the total specimen is length dependent and is not a proper benchmark on which to base pipe properties on basis of the global moment-curvature curve, however, the softening points will coincide with the limit points of the local moment-curvature curve and become independent of the overall specimen length. Limit strains for both plain pipes

and girth-welded pipes were derived using global-local strain plot to define the softening point.

Souza *et al.* (1999) investigated to use finite element package ABAQUS to analysis full-sized girth-welded line pipe subjected to constant axial force, internal pressure, and monotonically increasing curvatures In order to predict the deformed configurations correctly in post-buckling range for girth-welded pipe, the "best" type model was the model that use four-node, doubly curved, reduced-integration, finite-membrane-strain, S4RF shell element and the girth-welded effect was considered by mesh refinement: (*i*) weld element of approximately the same dimensions as the weld size; (*ii*) a gradual increase in the element dimensions of the mesh as one recedes from the weld elements; *(iii)* the effects of geometric mismatch imperfection between the pipe cross sections at the junction of the pipe cans; and (*iv*) the residual stressed generated by the welding process. The rigid connections in the experiment between the ends of pipe segment(at which the cross section is maintained in its original shape by rigid end plates welded to the pipe) and the knife edge (about which the end fixture was constrained to pivot by the test setup) was modeled by the cone with triangle STR13 element. The fine mesh (near weld area) connected with coarse (uniform) mesh by constrained the middle nodes on the common circumferential lines to have displacements and rotations with quadratic polynomial passing through three adjacent nodes in the uniform mesh. The mesh has 1440 quadrilateral finite strain S4RF elements, 36 triangle STR13 elements, 36 rigid constraint elements and 1535 nodal points.

The model was verified by comparing to the two series of published full-sized experimental results in terms of the moment-curves and the post-buckled deformed shapes: one on plain pipe (Mohareb *et al.* 1993), and the other on girth-welded pipe (Yoosef-Ghodsi *et al.* 1995). The shapes of the deformation from the numerical model are same as the experimental results. The numerical model confirmed that the locations of the wrinkles were incorporated with the girth-weld and the mechanism of the formation of the wrinkle through evolution process.

Detailed comparison with two girth-welded specimens (one unpressurized pipe UGA12W and one pressurized pipe DGA12W) was reported. It was observed that the numerical solution and the experimental results of unpressurized pipe UGA12W bear a striking resemblance, not only in terms of moment-curves, but also in terms of the deformed configuration which has a diamond pattern. However, the location of the dimples in wrinkle is in the vicinity of the girth-weld while the pattern exhibited by the experiment straddles in the girth-weld. For pressurized pipe DGA12W, the moment-curves results do not correlate as well as those for the unpressurized specimen, but are still considered to be adequate. The final configuration which is called bugling mode from the numerical results closely resembles that from the experiment.

The best model was also demonstrated that can be served as a guide for producing finite element models which will give realistic simulations for pipe behavior in other situation. This was proved by using this model to simulating NPS20 unpressured plain pipe and comparing the moment versus curvature results with other five different meshes was given.

DelCol *et al.* (1998) conducted four full size NPS30 pipes with diameter (762 mm) to thickness (8.3 mm) (*D/t*) ratios of 92 to investigate the behaviour of pipelines deformed into the post-buckling range under combinations of internal pressure, axial compression and imposed curvature. The specimens were subjected to internal pressure causing hoop stresses of 0, 20, 40 and 80 percent of yield strength of the pipe material to determine the effect on the local buckling mode. It was found the non-pressurized specimen failed in a "diamond shape" mode whereas the pressurized pipes failed in a single "outward bulge" mode. It was also found increased internal pressure lower the buckling moment but stabilize the post-buckling behaviour. Non-linear finite element models which incorporate measured initial imperfections and material properties were developed using commercially available FE code ABAQUS. Good correlation between the analytical and test results was observed. Based on analytical study of initial imperfections, it was concluded that the increased magnitude of initial imperfections causes a significant reduction in peak moment and buckling curvature. It is also found that initial

imperfections dictated the location of the local buckling and an unsymmetrical diamond buckling mode instead of a symmetrical diamond mode for unpressurized pipe specimen.

Dorey *et al.* (2001) conducted a total of 15 full-scale experimental tests on NPS30 pipe with a D/t ration of approximately 92 under a combination of axial load, internal pressure and monotonically increasing curvature to investigate the critical buckling strain. The influence of circumferential girth weld and initial imperfection was investigated in the tests. A finite element model capable to incorporate initial imperfection was developed using ABAQUS and validated by comparing the analytical results with not only his own tests but also some typical results from literature, i.e. Mohareb *et al.* (1995) and Yoosef-Ghodsi *et al.* (1995) for specimens with D/t of 54 and 61. A good agreement is achieved between the analytical results and test results. Four important parameters that influence the development of load capacity and critical buckling strain of the pipe segment were identified, which are diameter-to-thickness (D/t) ratio, internal pressure (p/p_y) ratio, material properties and initial imperfections. Finally critical buckling strain equations for both plain pipe and girth weld pipe (D/t ratio up to 92) were proposed based on the parameter study, although the predictive ability of those equations should be further validated.

Das *et al.* (2002) conducted 12 full-scale Norman Wells NPS12 pipe tests using both plain pipe and girth welded pipe to study limit strains and fracturing behavior of wrinkled pipe specimens under monotonic or cyclic load, two tested under pure axial compression and internal pressure, six tested under cyclic axial load and internal pressure, and four under cyclic axial load, cyclic moment and internal pressure. It was mainly observed that:

(a) The pipe specimens are highly ductile and don't fail in fracture when they are subjected to monotonically increasing axi-symmetric compressive axial load.

(b) When pipe specimen is subjected to strain reversal, the fracture can occur in the wrinkled region in a very few cycles (less than 10).

(c) The Maximum strain values that occurred in these test are much higher than permissible strain values in the design standards and current practice in pipeline industry.

(d) The fracture pattern observed in the tests is similar to that in the field observation.

A numerical simulation then was developed to predict the pipe behavior under cyclic loading. This model used general purpose 4 node shell element S4R, non-linear isotropic hardening material model using a modified true strain-stress curve and symmetry boundary conditions, girth weld was also considered. It was found that the prediction of deformation patterns by numerical model is very good for cyclic axial specimens and reasonable for cyclic bending.

In order to develop a fracture criteria model for a wrinkled pipe under cyclic loading, 16 strip tests were performed. A failure criteria based on 24 tests results, eight of the tests done by Mayholm (2001), was provided to predict the residual life of the wrinkled specimens which were subjected to low cycle fatigue loading, although this criteria seems to be conservative.

Dinovitzer *et al.* (2004) developed a non-linear finite element (FE)-based wrinkle and buckle formation and growth model under combined load using commercial FE code LS-DYNA. The model used finite membrane strain shell element with appropriate mesh size and Ramberg-Osgood stress-strain material formation, as such,

$$\varepsilon(\sigma) = \frac{\sigma}{E} + (\frac{\sigma}{K})^{1/n} \tag{2.7}$$

where, n is the strain hardening exponent, k is the strength coefficient.

The internal pressure and axial load (compression) were applied first and keep constant; a bending load is imposed to the center node at the end section of the model. The model is symmetry in one or two planes depends on the load condition. Last circumferential strip of shell element is modeled as linear elastic. The central nodes are rigidly connected to the shell nodes on the end section by rigid beam.

The model was validated by comparison with two full-scale test results performed by Mohareb *et al.* (1994), FE models by Mohareb *et al.* (1994), Hauch & Bai (1998), and Bruschi *et al.* (1995) in terms of moment-curvature relations and better agreement is got by this model. The stress-strain and deformation patterns predicted by this model also

follow the trends observed in the experiment trails. Maximum bending moment prior to the onset of buckling or wrinkling predicted by the model is agreed with the estimation using analytical equations proposed by Bai & Hauch (1998).

2.3.2 Research in USA

Smith, M. Q. *et al.* (1998) conducted four full-scale wrinkling tests of large diameter, corroded pipe specimens subjected to simulated in-service loads from internal pressure, axial compression from thermal difference, and longitudinal bending from settlement. The tests used 48 inch (1220 mm) diameter X65 pipe. Corrosion is represented in each as a region of thinner wall thickness, the size and shape of which attempted to bound the dimension of general corrosion found in serve. The tests were performed in the four-point bending and axial loading test facility. The tests were carried out in the sequence of one nominal test, and three following tests by varying internal pressure and the size of the corrosion. The experiment research by Smith was used to provide data essential to development and validation of the finite element (FE) simulation by using commercially available FE code ABAQUS. Smith identified that the FE analysis could predict the correct trend in behavior up to and at wrinkling, however it under-predicted the wrinkling moment produced in the tests probably attributed to the softer representation of the material properties in the FE model.

Hauch and Bai (1998) developed a finite element model to simulate the local buckling/collapse. The purpose is to find the possibility to use FE analyses in local buckling design as an alternative to rule-based design. Hauch and Bai's FE model adopted S4RF shell element and Ramberg-Osgood strain-stress relationship material model, also introduced imperfections such as initial ovlisation and corrosion. This FE model was validated by the experiment results conducted by previous presented Mohareb *et al* (1994), the analytical solution for the calculation of the maximum allowable bending moment for a corroded pipe by Bai & Hauch (1998), and a previous validated FE model for infinite long pipes by Bai *et al.* (1993). Bai & Hauch found generally a good agreement between this FE model and the experiment results, however, the accuracy gets

less in the post-buckling phase even the deformation pattern seems to be in good agreement with what is seen from the full-scale tests, and for high internal overpressure, initial ovalization has almost no influence on the moment capacity while for low internal overpressure and external overpressure ovality is thought important and the direction of the ovalization and the position of the corroded area are to be combined to give the worst condition. It was suggested that FE analyses maybe applied in design by selection of proper partial safety factors.

Hauch and Bai (2000) also presented an analytical equation to predict the ultimate bending moment capacity for pipes subjected combined pressure, longitudinal force, and bending. The equation is account for initial out-of-roundness, longitudinal factor and internal/external over pressure for either isotropic or anisotropic material. Characteristics of the ultimate strength for pipes subjected to single loads, i.e. pure bending, pure external pressure, pure internal pressure, pure tension and pure compression were also investigated. These characteristics of the ultimate strength as well as the ultimate bending moment were compared with the results by previous described FE models for a *D/t* from 10 to 60. It was found that the FE results were in good agreement with the analytically deduced results. However, the analytical solution gave unconservative results for external pressure very close to the collapse pressure. It was also found that the geometrical imperfections (excluding corrosion) that are normally allowed in pipeline design will not significantly influence the moment capacity for pure bending. Finally it was concluded that by choosing proper safety factor, these criteria may be used in pipe design.

2.3.3 Research in Europe

Gresnigt *et al.* (2001) carried out four full-scale 20 inch (508mm) pipe bending tests to investigate the effect of the manufacturing process (seamless, UOE) on the local buckling behavior of pipe. In their research program, three UOE manufactured pipes and one seamless pipe with *D/t* ratios 45, 27, 22, and 29 have been subjected to four point bending tests to determine the maximum moment capacity, the curvature at maximum moment and the ultimate curvature. The steel grade was X65. By comparing the critical

strain from the tests with the predictions calculated from the literature formulae, it was found that for the tested *D/t* ratio, cold expansion (UOE) is good for the critical strain capacity (bending), although, the combination of the load conditions. The test results and other relevant experimental data related to buckling of pipes were grouped to a database by different loading conditions and compared with the design formulae proposed in the literature. Statistical and probabilistic evaluations were carried out to determine the best design formulae and appropriate safety factors. Finally two design formulae applicable for *D/t* values between 15 and 50 for offshore pipes and *D/t* ratio up to 100 for onshore pipes were proposed, one is bending strain at maximum moment (critical bending strain) without external pressure based on Murphey-Langner and the other is bending moment capacity (ultimate bending moment) without external pressure which was base on DNV (1996).

Vitali, L. *et al.* (1999) created a finite element model to investigate the buckling mechanisms and limit state formulations of pipes subjected to internal pressure, bending moment and axial compression. This model does not consider any local pipe imperfection and the pipe material modeled as isotropic. The mesh consists of a refined region which is 0.5 diameters long and consists of 16 elements of constant length. After this refined region, the longitudinal element dimension increases gradually from the left end side to the right end side of the finite element model. The FE model was calibrated by comparison between the FE results and the full-scale experimental tests from previous investigation by Mohareb *et al* (1994). Vitali, L. *et al.* conducted a total of 120 parametric numerical analyses in which the *D/t* ratio, material, internal pressure ratio (P_i/P_y) and the axial load are variables. *D/t* ratio used were of 20, 30, 40 and 60, however, this model was validated using experimental data with *D/t* ratio of only 50 and 63. It is acknowledged that this model may be not applicable to the lower *D/t* ratios. This concern is fulfilled by the following experimental tests by Vitali, L. *et al* (2005) in which the *D/t* ratios are lower than 40. Based on comprehensive FE analysis, predictive equations for $D/t<60$ in terms of limit bending moment and limit longitudinal compressive strain for the wrinkling limit states were proposed. A number of deformation limits with the

objective to provide a conservative estimate of longitudinal strain at bursting for thick pipes $D/t<30$ exposed combined load have been proposed as well.

Vitali, L. *et al.* (2005) performed four full-scale bending tests on pressurized pipes to investigate the buckling mechanisms of pipes with outer diameter to thickness ratio (D/t) lower than 40. The pipe specimens are subjected to internal pressure, axial force and bending moment. Two 16 inch (406 mm) seamless pipes with $D/t=25.6$ and two 16 inch (406 mm) welded UOE pipes with $D/t=34.2$ were used in their tests, girth weld was also presented. The steel pipe material was an X65 with a specified minimum yield stress (SYMS) and a specified minimum tensile stress (SYTS) of 450 and 530 MPa, respectively. Material testing shows anisotropic in both seamless and UOE pipes. Pipe specimen geometry characterization i.e. diameter, thickness, fabrication ovalization was measured before tests. Pipe specimens are grouted outside the test region to avoid local buckling at the load positions. The length of the un-grounted mid-span of the specimen is approximately 4 times the out diameter. A misalignment offset was introduced at the girth weld. The specimens subject to constant internal pressure up to 80% yield pressure and axial force and bending moment by four-point bending up to reach the maximum bending moment. A few cyclic variations (5-10 cycles) of the internal pressure and bending moment for pipe specimen are also tried. However, it was found the ratcheting was not significant due to cyclic load. It was also found in the tests,

(a) The experimental tests confirmed that thick-walled pipes ($D/t<40$) subject to internal overpressure developed large strain at the limit bending moment. Due to internal pressure, the outward buckling mechanism has developed for the four pipe specimens tested, however, there are more than one outward bulges occurred in their pipe specimens. This is quite different from observation by previous research, i.e.

(b) The limit bending capacity of specimen with the girth weld at mid section including an offset is reached at loads lower than for the specimen (the same pipe) without weld. Same as that discovered by Yoosef-Ghodsi *et al* (1995).

(c) The girth weld is located in the buckle "valley", of both specimens with girth weld. This indicates that the local higher wall thickness from the weld beads and /or the overmatch in yield strength to the parent material affect the development of buckling.

Particularly they provide a higher radial stiffness than the nominal pipe- restricting outward local buckling.

(d) One pipe specimen failed by tensile rupture close to the reinforced region, causing bursting at testing internal pressure. A considerable necking was noted: the wall thickness at the rupture was 7.6mm versus the nominal 16.5mm.

A FE model was then developed with shell elements using commercially available FE code ABAQUS and capable to predict the local buckling behavior of the girth weld pipe. The mesh is not constant mesh. The test conditions were matched as closely as possible: this includes the test configuration, the stress-strain curves (i.e. using measured curves as input), and the loading history. The offset misalignment has been investigated according to the experimental tests. Their FE results very realistically reproduce the observed failure mechanisms by formation and localization of wrinkles on the compression side of the pipe. They also found good agreement in the moment capacities (with predictions only 2.5 to 8% above measured values), but larger differences arose for the deformation capacity, suggesting that the DNV OS-F101 (2000) formulation for the characteristic bending strain (which is based on Vitali, L. *et al.* (1999)) may be non-conservative in certain cases.

Torselletti_*et al.* (2005) developed a three dimension FE model in ABAQUS to analysis the bending capacity of girth welded pipes under different load conditions. This FE model is based on the model of Vitali *et al.* (1999), considering the presence of girth weld and its related imperfect such as misalignment and weld material mechanical characteristics mismatch. Their model consists of 41 elements around half of the circumference and 172 elements in the longitudinal direction. A refined region is graduated longitudinally in proximity of the weld of the model where the buckling occurs. This refined region is 0.5 diameters long and consists of 32 elements of constant length. After this refined region, the longitudinal element dimension increases gradually from the centre to each end side of the finite element model. The material model uses Ramgerg-Osgood equation without Lüder's plateau.

A parametric analysis was also carried out to study the effect of the relevant parameters i.e. load combination (pure binding, bending and internal differential pressure equal to 35% and 72% of the yield pressure), pipe geometric characteristics (*D/t*) ranging from 35 to 60, pipe material (X65, X70, X80), geometric imperfection (offset misalignment and ovality misalignment). By comparison their FE analysis results in terms of limit bending moment and corresponding curvatures and compressive longitudinal strains with the DNV OS-F101 (2000) design equation and with full scale experimental data available in the literature, Yoosef-Ghodsi *et al.* (1994), it was found that the FE model results are shown to compare reasonably well with full scale experiments performed for on-shore pipelines. It was also found: (i) the DNV OS-F101 (2000) design formats for local buckling failure are applicable up to D/t ratio equal/ lower than 55, (ii) pipes with *D/t* ratio between 45 and 55 probably more sensitive to girth weld misalignment than pipes with D/t ratio less than 45, (iii) FE calculations show a reduction of the limit bending moment from the one calculated using DNV OS-F101 (2000) design equation when the pipe is modeled in combining bending and internal pressure condition and weld misalignment is considered. Such reduction ranges from 5% to 10%. However, this is no explicitly covered by DNV OS-F101 (2000) moment based equation (iv) the effect of weld misalignment on the compressive strain at limit bending moment appears conservatively included in the design equations.

2.3.4 Research in Other Area

Yatabe, H. *et al.* (2004) carried out six axial compression experiments to investigate the strain-stress behavior and the pipe geometry on the deformability of high grade line pipe. The pipe specimens used in the tests were API 5L X80 line pipe with 406.4 mm outer diameter, varying by *Y/T* values (*Y/T*=0.8~0.96) and wall thickness (*D/t*=43.2 and 64.0). Of the six specimens tests, one was unpressured and the other five were pressured so that the circumferential stress generated 0.4 SMYS or o.3 SMYS and then remained steady. The experiments were carried out until the applied load decreased to 75% or less of the maximum loads due to local wrinkle had formed. A finite element analyses model was also developed using ABAQUS version 5.8 and verified by using the tests results. The FE

models were built with 4-node, 2D and axisymmetrical solid elements, and the yielding condition followed the von-Mises yield criterion for isotropic hardening. Comparing the FE analyses with the experiment results, Yatabe found that the deformability of the linepipe decreased with an increase in *D/t* and *Y/T*, however, it also dependent on the shape of the stress-strain curves. Yatabe also confirmed the complementary energy concept (Ohata, M. *et al.* 1999) and proposed that this concept could be used to improve the deformability of high-grade pipelines.

2.4 PIPELINE MAINTENANCE AND INSPECTION

Pig is the one of the important tools for inspection and maintenance of pipeline and to its integrity. Pig is a generic term signifying any independent, self-contained device or vehicle that moves through the interior of a pipeline for the purposes of inspecting, dimensioning, and cleaning that pipeline or for transporting (batching) pipeline product. There are two major types of pigs, utility pig and inline inspection tool (ILI), which is called intelligent pig, or smart pig.

2.4.1 Inline Inspection Pig

One of the most popular intelligent pigs is GEOPIG® as shown in Figure 2.9. This section mainly discusses the detail aspects of this kind of pig. Pipeline deformation and movement can be accurately and efficiently achieved by this Inertial Geometry Inspection System GEOPIG®. It has been successfully used for inspecting pipeline for more than 17 years in order to prevent pipeline failures (Czyz, J. A. *et al.* 2003). It can inspect oil and gas pipelines in permafrost areas, deserts, deep sea and many other areas around the world. It can provide high accurate three dimensional geographic and geometric data of pipeline in one run inspection. (Czyz, J. A. *et al.* 1996)

Usually the GEOPIG® is equipped with following sensor systems:

(a) The Inertial Navigation System (INS) comprises inertial angular velocity sensors (gyroscopes) and linear accelerometer. The system measures the precise path the pig

has taken when it travels through the pipeline. This system is used to produce a detailed map of pipeline, measure curvature, and identify any potentially serious out of straightness. This system is also used to locate welds and dents.

(b) Odometer measures the pig's distance moved along the line (chainage), and instantaneous speed in the pipeline.

(c) Weld Detect Sensors use eletromagnetic variation to provide data on weld location and individual joint length.

(d) Pressure and Temperature Sensors measure pressure and temperature of the pipeline during the pig running.

(e) Sonar Calipers measure internal diameter, ovality, and dent size and shape of the pipeline.

Other inspection techniques such as ultrasonic inspection tool, direct magnetic response sensor are also used in pipeline recently.

2.4.2 Utility Pig

Utility pigs can perform various functions, such as removal of debris, cleaning the rust, gauging, filling, de-watering, drying, separation (batching), removal of condensate, meter proving, product conversion, gel pigging, and coating application (PESC 1999).

Utility pigs can be divided into five groups based on their construction characteristics:

(a) Metal bodied pigs (often referred to as 'mandrel' pigs).

(b) Solid cast pigs – single piece polyurethane casting – usually 'dumb-bell' shaped.

(c) Foam pigs – made by moulded polyurethane foam.

(d) Spheres – manufactured from cast polyurethane and various rubbers.

(e) Special pigs including dual diameter pigs, articulated pigs, and high differential pigs.

2.4.3 Pig Fitting

Most of the metal pigs are able to accommodate up to 5% -10% reduction of the pipeline internal diameter. Some foam pigs can even cope with reduction of 65% in the pipeline (PESC 1999).

Pipeline design standards also have rules for pig dimensions. For example, as for Clause 10.15of British Standard, BSI PD-8010-1-2004, gauging pigs should be equipped with a soft metal disc of diameter not less than 95% of the smallest internal diameter of pipeline up to 508 mm nominal and 25 mm clearance of larger pipes. As for Clause 13.2.2 of BSI PD-8010-1-2004, a pigging philosophy should be established for each pipeline system as part of the design, and should confirm that the pipeline is free of restraints or obstructions for the passage of pigs. Norway design standard (DVN-OS-F101-2000) also has similar rules for pigs. According to Clause O408 of DVN-OS-F101-2000, the basic requirement for gauging is to run a metallic gauge plate with a diameter of 97% of the nominal inner diameter through the pipeline.

The dimension of a pig is obviously restricted based on its design and usage. Therefore, severe pipe wall deformation caused by accordion type of wrinkling will restrict the movements of pigs and cause maintenance and inspection problem using various pigs.

2.5 SUMMARY

A large numbers of studies have been undertaken by various researchers to investigate the local buckling behavior of the energy pipes up to stable and strain-hardening post buckling stage, the research tools includes experimental, theoretical and numerical methods. The main purpose of these studies is either to understand the mechanism of the pipe under relevant loads or to investigate more reasonable and nonconservative formulations for pipe engineering practice. This is reflected in current codes, several of them adopts combined stress-based and strain based design philosophy. When buckling is load controlled, limit bending moment or limit stress formula is needed to prevent failing,

whereas buckling is displacement controlled, correspondent limit strain is need. However, current studies were concentrated in onset of local buckling (wrinkling). No research has ever been conducted further to concern the pipe behavior when its wrinkle develops far beyond onset point, for example, inner surface contacts which may cause rupture of pipe or maintenance and inspection problems in pipeline operation. Consequently an extensive research is needed to carry out to understand pipe behavior in this stage.

Table 2.1 Examples of Pipelines that have Used Strain-Based Design
(Edison Welding Institute Report on Project No. 45892GTH, 2003)

Pipelines Built with Strain-Based Designs	
Northstar for BP	Shallow subsea in Alaskan arctic
Haltenpipe for Statoil	Design strain limits near 0.5%, mostly for spanning on uneven seabed
Norman Wells for Enbridge	On-shore pipeline across permafrost, strain based acceptance of on-slope design
Badami for BP	River crossings in Alaskan arctic
Nova Gas Transmission Line in Alberta	train-based acceptance for discontinuous permafrost
TAPS fuel gas pipeline	Strain-based acceptance of upheaval buckling in permafrost
Ekofisk II pipelines for ConocoPhillips	Limit state design over subsiding seabed
Malampaya for Shell	Shell Limit state design for seismic events and seabed movement
Erskine replacement line for Texaco	Limit state design for HP/HT pipe-in-pipe replacement
Elgin/Franklin flowlines and gas export line	Limit state design for pipeline bundles
Mallard in North Sea	Limit state design for pipe-in-pipe
Pipelines Considered or in Process with Strain-Based Designs	
Sakhalin Island for ExxonMobil	On-shore pipelines in seismic area
Liberty in offshore Alaska for BP	Shallow water Arctic pipeline
Thunder Horse for BP	Limit state design for HP/HT flowlines

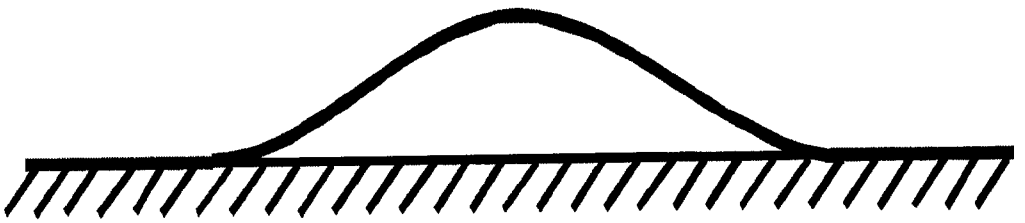

Pipeline elevation

Figure 2.1 Upheaval Buckling (vertical mode) of Pipeline (Song *et al.* (2003))

Figure 2.2 Snaking Buckling (lateral mode) of Pipeline (Song *et al.* (2003))

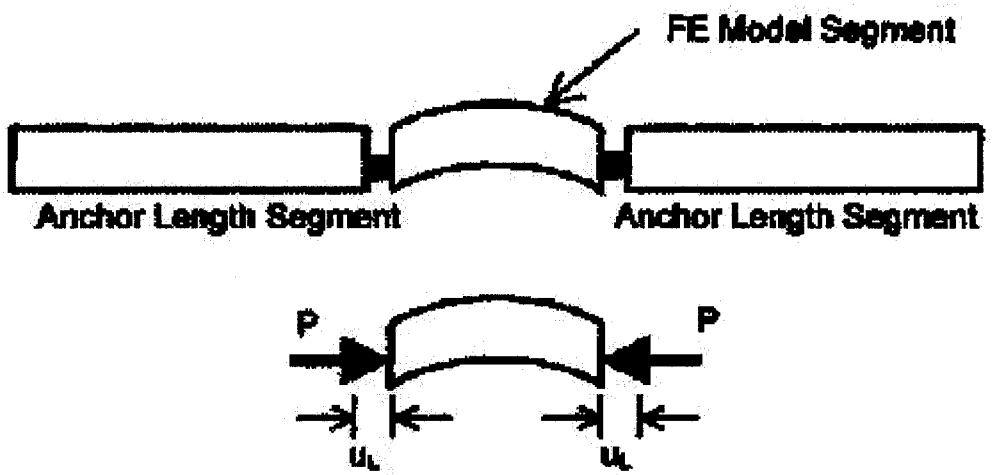

Figure 2.3 Idealized Interaction of Anchor length Segments and FE Model Segment (Einsfield *et al.* (2003))

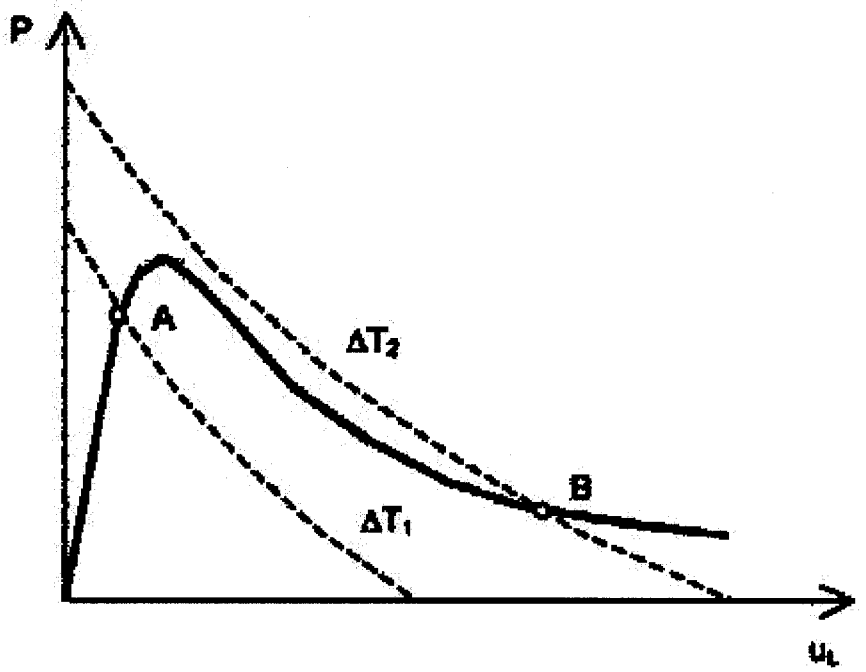

Figure 2.4 Compatibility Solutions for End Axial Forces and End Axial Displacement (Einsfield *et al.* (2003))

Figure 2.5 Outward Bulge Shape of Local Buckling of Pipeline (Mohareb *et al.* (1994))

Figure 2.6 Inward Diamond Shape of Local Buckling of Pipeline (Mohareb *et al.* (1994))

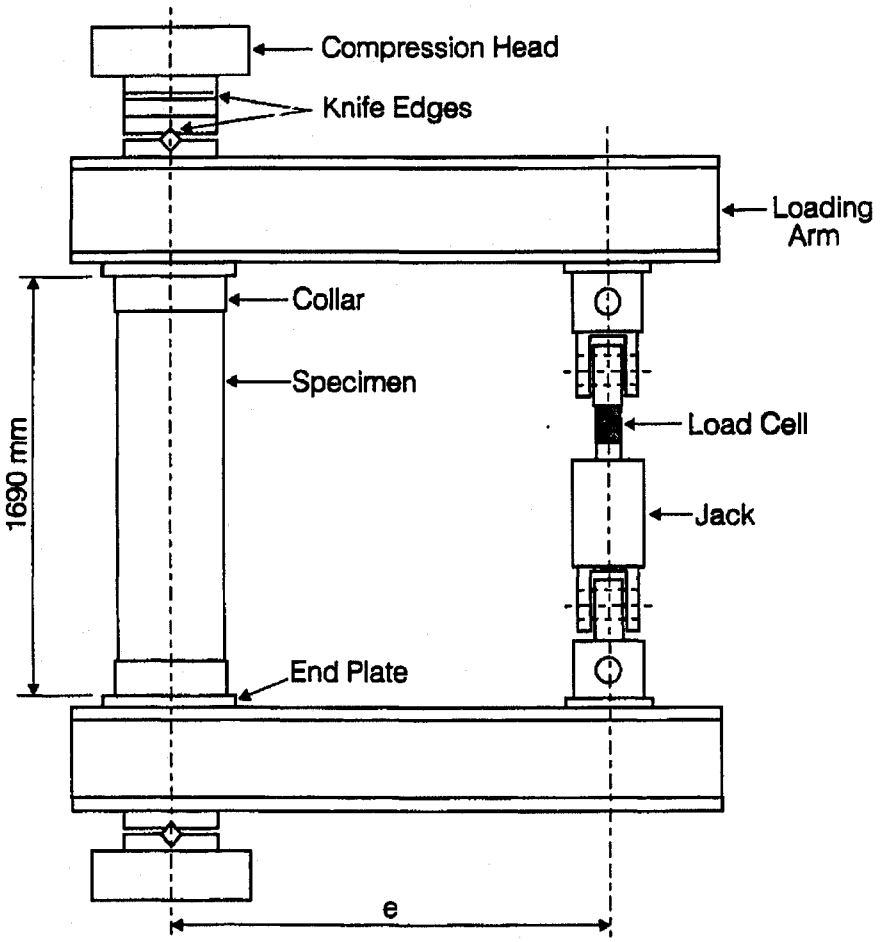

Figure 2.7 Experiment Setup (Mohareb *et al.* (1994))

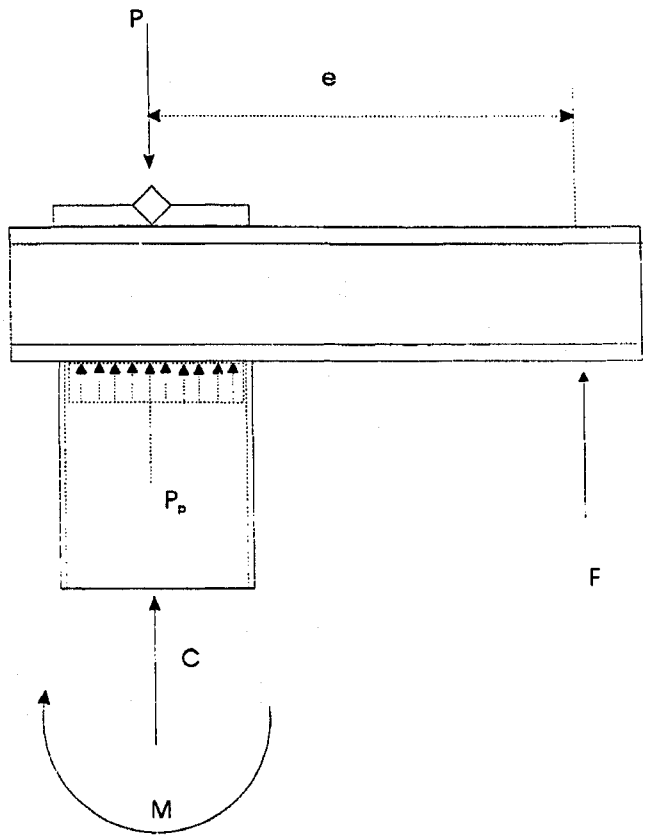

Figure 2.8 Free Body Diagram for Loads Acting on Specimen (Mohareb *et al.* (1994))

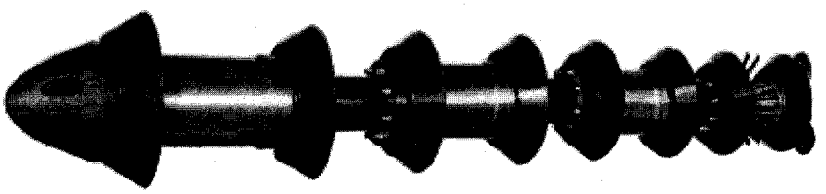

Full View of NPS 8 Geopig

Figure 2.9 Full View of the Example Geopig from Michailides, P. *et al.* (1998)

3 DEVELOPMENT OF THE FINITE ELEMENT MODEL

Experimental testing method is undoubtedly the most trusty and traditional way to study and understand the local buckling (wrinkle) behavior of the pipelines, and it has been used since 1970s. However, this method has its limits in studying post buckling behavior of energy pipe under axial-symmetric loading and deformation. Tests are expensive and time-consuming, and it is unrealistic to consider full scale tests for various possible axi-symmetric loading cases and other parameters. Nevertheless, tests could not provide all the information that were required for thorough study such as the information inside of the pipe could not be obtained using experimental methods. Following the development and easy availability of the computer and technology, an alternative method to study and predict the pipeline structure behavior using numerical tools such as Finite Element Analysis (FEA) method has become more popular. FEA method was effectively used by former researchers, for example, Mohareb *et al.* (1993), DelCol *et al.* (1998), Hauch and Bai (2000), Dorey *et al.* (2002), Das *et al.* (2002) for reliable prediction local and global buckling behaviors of energy pipelines.

In this study, a nonlinear FEA numerical modeling technique is employed to simulate the behavior of the two test specimens using the commercially available finite element analysis software code ABAQUS/Standard and ABAQUS/Explicit Version 6.6-2 distributed by ABAQUS, Inc (which will be called as ABAQUS in the subsequent discussion). This software code was chosen to accomplish the simulation for several reasons. First of all, it supports nonlinear stress analysis which contained material nonlinearity, geometric nonlinearity, and boundary nonlinearity. It allows pipe under large deformation using nonlinear geometry and finite strain formulation. It also offers models for a wide range of nonlinear material behaviors with various hardening rules. It offers finite sliding formation with strict slave and master algorithm for modeling pipe contact with various contact models, namely, constitutive model, damping model, and friction model.

Furthermore, ABAQUS code also supports different shell elements for thin and thick problems. Another advantage of the ABAQUS is that it offers both Standard and Explicit solution techniques. The Explicit solution method was required to determine the fracture failure criterion for pipe models which were analyzed using Standard solution method. ABAQUS offers both load controlled and displacement controlled solution strategies. The load controlled strategy could be used to only model the initial elastic loads (initial MTS load and pressure) applied to the pipes, and the displacement controlled strategy could be used to pass the ultimate load point and carry out to elastic-plastic analysis range. In addition, ABAQUS also allows to control on the solution process and convergence criteria.

The objectives of developing the numerical models are to (i) predict the pipe behavior under axi-symmetric axial deformation and constant internal pressure, and, (ii) conduct detailed parametric study for various *D/t* ratios, internal pressures and material for developing failure guidelines for pipeline industry.

3.1 CONCEPT OF FINITE ELEMENT METHOD

The powerful finite element method began in the 1950s, and with the widespread use of the digital computer it has since gained considerable favor relative to other numerical approaches. This method is applied in a wide scope of application from structural analysis, fluid problem, to electrical field and other engineering areas.

In structure area, the finite element method may be viewed as an approximate Ritz method combined with variational principal applied to continuum mechanics. It permits the prediction of stress and strain in an engineering structure with unprecedented ease and precision. In the finite element method, the structure is discretized by a finite number of elements connected at their nodes. In addition to the nodal compatibility and equilibrium, the compatibility must also be satisfied along the boundaries between elements. Once the stiffness of each element is determined, all the elements are assembled through matrix algebra using force equilibrium and displacement

compatibility to obtain the global stiffness matrix of the structure. Then the necessary boundary conditions are applied. Finally, the loads and displacement are applied to the model and the global responses (reaction forces and displacements) and stresses/ strains are obtained by using global equilibrium equations for the structure. In nonlinear analysis, an incremental solution strategy is required to solve the equations of equilibrium. A more detailed description of FEA process can be reviewed in numerous references (for example, Cook, R. D. 1981).

3.2 FINITE ELEMNT MODEL

3.2.1 Element Selection

A general purpose shell element S4R was selected from ABAQUS three dimensional conventional shell element library to discretize the pipeline segment, since one dimension, the thickness of the pipe segment is significantly smaller than the other dimensions, length and diameter. This element is a four-node quadrilateral shell element with reduced integration and a large strain formulation. This element was used by many former researchers such as DelCol *et al.* (1998), Hauch and Bai (2000), Dorey *et al.* (2002), Das *et al.* (2002), and it was found to be a suitable element for nonlinear large deformation analysis of pipeline segments under different load, deformation and boundary conditions.

The S4R element provides solutions to both thin and thick shell problems, allows transverse shear deformation, and supports finite membrane strains. In other words, it uses thick shell theory as the shell thickness increases and become discrete Kirchhoff thin shell elements as the thickness decreases. The transverse shear deformation becomes very small as the shell thickness decreases.

The shell section thickness is changed as a function of the membrane strain based on user defined effective section Poisson's ratio, υ,

$$\frac{t}{t_o} = \left(\frac{A}{A_o}\right)^{\frac{\upsilon}{1-\upsilon}} \tag{3.1}$$

where, t, current shell section thickness, t_o, original shell section thickness, A, current area on the shell's reference surface, A_o, original area on the shell's reference surface. The reference surface of the S4R element is defined by nodes and shell normal.

The S4R element uses reduced (lower-order) integration to form the element stiffness, while the mass matrix and distributed loadings are still integrated exactly. Reduced integration usually can provide more accurate results (provided the elements are not distorted or loaded in in-plane bending) and significantly reduces running time. The numerical integration through the thickness is done by using Simpson's rule. Five integration points are used through shell section thickness, which allows nonlinear surface behavior of the pipe section to be followed through the load history.

The reduced integration may introduce hourglass modes. The enhanced hourglass control approach is used to provide hourglass control. This method represents a refinement of the pure stiffness method in which the stiffness coefficients are based on the enhanced assumed strain method and no scale factor is required. This method also provides increased resistance to hourglass for nonlinear materials and better coarse mesh accuracy in displacement solutions for linear elastic materials than other hourglass control methods.

This element has six degrees of freedom at all nodes, which are three displacement components (u_x, u_y, u_z) and three rotation components (θ_x, θ_y, θ_z).

Another shell element STRI3 was also used to model the end plates of the test specimens. The end plates were used to hold the pressure water in the tests, and were 75 mm in the thickness. The STRI3 element is a three node triangular facet thin shell element. The thin shell element means that the transverse shear flexibility is negligible. The element is a flat element, so the initial curvature is also ignored. This element also has six degrees of freedom at all nodes. This element could provide for arbitrarily large rotations but only small strains. The change in thickness with deformation is ignored in this element. Since

the end plates did not experience inelastic deformation in the test, this element for modeling the end plates is reasonable.

3.2.2 Symmetry of the Model

The test specimens had symmetry in geometry, boundary condition and loading. Therefore only a half of pipe as shown in Figure 3.1 was considered to model for numerical analyses of pipe tests and parametric study. Thus, the degrees of freedom of the whole model were reduced to almost half, and thereby, the computing time for numerical analyses was reduced significantly.

3.2.3 Boundary Conditions

The boundary conditions used in the numerical model followed the physical and kinematic boundary conditions used in the tests. Boundary conditions for modeling symmetry conditions were also applied (Figure 3.1) in FEA model.

Figure 3.2 is the schematic of the test set up. A multi point constraint (MPC) was used to model the boundary condition at the top end of the pipe. The master node is at the centre line of pipe specimen and located at 333 mm away from the top end plate, the slave nodes are the top end nodes of the pipe model as shown in Figure 3.1. A Rigid beams is set between the master node and each slave node so that the displacement and rotation at the slave node is constrained to the displacement and rotation at the master node. Therefore the top end nodes of the pipe experienced same kinematic boundary conditions (deformations and rotations) as the master node. The bottom end of the pipe in the test was fully constrained and hence, all the degrees of freedom of the nodes at the bottom end of pipe model were constrained. However, it caused some problem to retain the responding load. To solve this problem, another multi point constraint (MPC) was also used at the bottom boundary condition of the model. The master node was set at the center line 333mm (same distance as the top master node) below the bottom end plate,

and the slave nodes were the bottom end nodes of the pipe. The fully constrained bottom master node would supply the same physical boundary condition as that in the full scaled tests.

The symmetry boundary conditions were applied to the numerical model. The pipe is symmetry along its length. The displacement in the x axis direction and rotation about y axis and z axis were constrained in the symmetry plane. Thus, the u_x, θ_y, and θ_z were set to zero for all the nodes on the plane of symmetry. The top master nodes were set to move in the direction of length only.

3.2.4 Material Model

The material used in the tests exprienced large plastic deformation. Therefore, an elastic-plastic material model using von Mises yield criterion and isotropic hardening with associated plastic flow rule was used.

The material model was defined by giving the value of the uniaxial yield stress as a function of uniaxial equivalent plastic strain in this model. The material property determined from the uniaxial coupon test is in terms of nominal stress and strain. However, in the ABAQUS material model, true stress (Cauchy stress) and logarithmic strain (true strain) are required. A simple conversion from nominal strain and stress to true stress and logarithmic strain for isotropic material that is adopted by ABAQUS is shown in Equation (3.2) and Equation (3.3).

$$\sigma_{true} = \sigma_{nom}(1+\varepsilon_{nom}) \tag{3.2}$$

$$\varepsilon_{\ln}^{pl} = \ln(1+\varepsilon_{nom}) - \frac{\sigma_{true}}{E} \tag{3.3}$$

Where σ_{true} is the true stress, $\varepsilon_{\ln}^{pl}$ is the logarithmic strain, σ_{nom} is the nominal stress or engineering stress, ε_{nom} is the nominal strain or engineering strain, and E is the Young's modulus. Material properties from the coupon test are list in Table 3.1 and Figure 3.3 shows the nominal stress-strain plot. True stress and strain behavior is shown in Figure

3.4. The collar of the pipe and end plates were modeled as elastic material, because they did not experience large deformation in the test.

A yield surface is the surface inside which the material will stay unyielding, Figure 3.5 shows a typical two dimensional von Mises yield surface. The three dimensional von Mises yield surface has a cylindrical shape, centered on the hydrostatic stress line. As a result, yielding of the metal is independent of the equivalent pressure stress. This is good enough for initially isotropic metals like the one used in the pipe structure. Therefore, von Mises yield criterion was chosen in the numerical model.

The flow rule defines the inelastic deformation that occurs when the material is no longer responding purely elastically. ABAQUS uses associated plastic flow rule which means that, as the material yields, the inelastic deformation rate is in the direction of the normal to the yield surface (the plastic deformation is volume invariant). This assumption is generally acceptable for most calculations with metals including the pipe material in the current model.

Hardening is the way in which the yield and/or flow definitions change as inelastic deformation occurs. Perfect plasticity (no hardening) is available in ABAQUS, which means that the yield stress does not change with plastic strain. This is obviously not appropriate for the material used in the tests. Another hardening available in ABAQUS is kinematic hardening, however, it is provided for material subjected to cyclic loading. Isotropic hardening was used in this model. In isotropic hardening, the yield surface changes size uniformly in all directions such that the yield stress increases (or decreases) in all stress directions as plastic straining occurs as shown in Figure 3.5. Isotropic hardening is generally considered to be a suitable model for problems in which the plastic straining goes well beyond the incipient yield state where the Bauschinger effect is noticeable (Rice, 1975).

3.2.5 Loading Procedure

The loading scheme consisted of a series load steps in the ABAQUS model and same test loading procedure was followed. The load steps are discussed next.

The first step in the loading procedure was application of the internal pressure P_i. Two different internal pressures were applied: (i) 1830 psi or 12.6 MPa for 80%P_y and (ii) 915 psi or 6.3 MPa for 40% P_y. P_y is the internal pressure causing yielding in the circumferential direction of the pipe, calculated as follows.

$$P_y = \frac{\sigma_y t}{r_i} \tag{3.4}$$

σ_y is the yield stress of the pipe material, t is thickness of the pipe wall, and the r_i is the internal radius of the pipe.

The second step was for the axial load through MTS (P_{MTS}) as it was applied in the tests. This axial load is applied considering the effects of the temperature differential, Poisson's ratio, and internal pressure.

$$P_{MTS} = P_t + P_\upsilon + P_e \tag{3.5}$$

in which,

$$P_t = A_s E \alpha \Delta T \tag{3.6}$$

$$P_\upsilon = -A_s \upsilon \sigma_h \tag{3.7}$$

$$P_e = \pi r_i^2 P_i \tag{3.8}$$

where, P_t is the compressive force to simulate a temperature differential of 45°C, A_s is pipe steel cross sectional area, E is the pipe material Young's modulus, α is the coefficient of thermal expansion, ΔT is the temperature difference, P_υ is the tensile axial load in the pipe wall due to the Poisson ratio effect, υ is the Poisson's ratio, σ_h is the hoop stress, and P_e is the compensating compressive axial force on the end plates.

In the next step, MTS load was increased keeping the internal pressure constant, since the pipe specimen did not yield under the combination of loading applied in the first and

second steps. For this load step, a stroke control method rather than a load control method was used.

3.2.6 Mesh Study

The total pipe geometry was divided into three regions, as shown in Figure 3.1, two collar regions at the ends of the pipe and the middle region. Each region has a uniform mesh. The mesh size of the collar region was relatively larger than the middle region, because collar regions did not experience large deformation. The larger mesh size reduced the total numbers degree of freedom of the FEA model. Five different mesh sizes were selected to study the effect of mesh size on load-deformation behavior of pipe specimen. The five sizes selected were 18×24, 18×29, 18×34, 24×34, and 24×38. These mesh sizes are refer to the model of the half pipe segment. The mesh sizes are expressed as a function of the size of an individual element used in the mesh, the first number refers to the number of elements in the circumferential direction and the second number refers to the number of elements in the longitudinal direction.

The mesh configurations that provided best correlation with the test data was finally chosen for the numerical modeling and parametric study. The final element aspect ratio was 1.1 for the collar region and around 2 in the middle region.

3.2.7 Contact Algorithm

Experimental study shows that the pipe specimens with internal pressure axi-symmetric continuing monotonic axial load and deformation form accordion type failure (Das *et al* 2002). Multiple wrinkle forms that looks like an accordion. The inside wall of the pipe makes self contact to develop the accordion deformation. A finite-sliding contact formulation was used to simulate this self-contact phenomenon.

The finite-sliding formulation allows for arbitrary separation, sliding, and rotation of the surfaces. Depending on the type of contact problem, two approaches are available to the

user for specifying the finite-sliding capability: (i) defining possible contact conditions by identifying and pairing potential contact surfaces or (ii) using contact elements. With the first approach, ABAQUS automatically generates the appropriate contact elements. Contact element approach is usually used when contact between two bodies cannot be simulated with the first approach which is a surface-based contact approach. In this model, surface based contact approach was used.

The strict "master-slave" algorithm was used to model this contact problem, as shown in Figure 3.6. In strict "master-slave" algorithm, each potential contact condition is defined in terms of a "slave" node and a "master" surface. The slave nodes are not able to penetrate into the master surface; however, the nodes of the master surface can, in principle, penetrate into the slave surface. The contact direction is always normal to the master surface.

The finite sliding contact formulation requires that master surfaces have unique surface normals at all nodes. Convergence problems can result if master surfaces that do not have smooth surface normals are used in finite-sliding contact analyses; slave nodes tend to get "stuck" at points where the master surface normals are discontinuous. ABAQUS/Standard automatically smoothes the surface normals of element-based master used in finite-sliding contact simulations.

The finite sliding contact formulation was used because this formulation can simulate two surfaces contacting with each arbitrarily without specifying the exact the contact areas which must be defined in other contact formulation.

Once the contact formulation is selected, the contact properties should be appropriately defined. Three contact properties were considered in the pipe contact problems: (i) a constitutive model for the contact pressure-overclosure relationship that governs the motion of the surfaces, (ii) a damping model that defines forces resisting the relative motions of the contacting surfaces, and (iii) a friction model that defines the force resisting the relative tangential motion of the surfaces.

The "hard" contact pressure-overclosure relationship was used in the model, as shown in Figure 3.7. Contact pressure between two surfaces at a point, p_c, is a function of h, overclosure of the surfaces (the interpenetration of the surfaces). Two models for $p_c=p(h)$ are available as described below.

$$p_c=0 \text{ for } h<0 \text{ (open)} \quad (3.9)$$

$$p_c>0 \text{ for } h=0 \text{ (closed)} \quad (3.10)$$

When surfaces are in contact (closed condition), any contact pressure can be transmitted between them. The surfaces separate (open condition) if the contact pressure reduces to zero. Separated surfaces come into contact when the clearance C between them reduces to zero.

The contact constraint is enforced with a Lagrange multiplier method representing the contact pressure in a mixed formulation, which allows no penetration of the slave nodes into the master surface.

Damping is not considered important in this model, since the contact surfaces could not experience resistant before contact established because of damping. Comparing the results with damping in modeling and those without damping, no difference has been noticed.

When surfaces are in contact they usually transmit shear as well as normal forces across their interface. There is generally a relationship between these two force components. The relationship, known as the friction between the contacting bodies, is usually expressed in terms of the stresses at the interface of the bodies. The default interaction between two bodies is frictionless. The frictionless model could not be used because it is understood that metal (steel) is not smooth enough to be frictionless. The classical isotropic Coulomb friction model was adapted as the friction model. In its general form it defines friction coefficient in terms of slip rate, contact pressure, average surface temperature at the contact point, and field variables.

The basic concept of the Coulomb friction model is to relate the maximum allowable frictional (shear) stress across an interface to the contact pressure between the contacting bodies as shown in the Figure 3.8. The isotropic friction model assumes that friction coefficient μ is the same in all directions. For a three-dimensional contact there are two orthogonal components of shear stress, τ_1 and τ_2, along the interface between the two bodies. These components act in the slip directions for the contact surfaces. These two shear stress components are combined into one equivalent frictional stress τ_{eq} as follow

$$\tau_{eq} = \sqrt{\tau_1^2 + \tau_2^2} \tag{3.11}$$

The standard Coulomb friction model assumes that no relative motion of the contact surfaces (stick) occurs if the equivalent frictional stress τ_{eq} is less than the critical stress, τ_{crit}, which is proportional to the contact pressure, p_c, in the form

$$\tau_{crit} = \mu p_c \tag{3.12}$$

where μ is the friction coefficient at the contact point. Beyond this point, the contact surfaces start to slide relative to each other. The stick/slip calculations determine a surface in the contact pressure- shear stress space when a point transitions from sticking to slipping or from slipping to sticking.

3.2.8 Solution Methods and Strategy

ABAQUS uses Newton's method to solve the nonlinear equilibrium equations. The motivation for this choice is primarily the convergence rate obtained by using Newton's method compared to the convergence rates exhibited by alternate methods (usually modified Newton or quasi-Newton methods) for the types of nonlinear problems most often studied with ABAQUS is higher.

In ABAQUS, The total time history for a simulation consists of one or more steps, and each step is broken into a number of increments in nonlinear analyses that the nonlinear solution path can be followed, at the end of each increment the structure is in

(approximate) equilibrium. The equilibrium solutions are attained by iteration using the Newton method to each time increment. The details of the Newton's method are described as follow.

The finite element method is solving a set of simultaneous equations in structural analysis:

$$[K]\ \{u\}=\{F\} \tag{3. 13}$$

where: $[K]$ is stiffness matrix, $\{u\}$ is vector of DOF (degree of freedom) values, and $\{F\}$ is vector of applied loads. When the coefficient matrix $[K]$ is itself a function of the DOF values (or their derivatives) then equation 3.13 is a nonlinear equation. The Newton's method is an iterative process of solving the nonlinear equations and can be written as (Bathe (1996)):

$$\left[K_i^T\right]\{\Delta u_i\}=\{F\}-\{F_i^{In}\} \tag{3.14}$$

$$\{\Delta u_i\}=\{u_{i+1}\}-\{u_i\} \tag{3.15}$$

$$\{F\}-\{F_i^{In}\}=\{R_i\} \tag{3.16}$$

where, $\left[K_i^T\right]$ is the tangent matrix, i is subscript representing the current equilibrium iteration, $\{F_i^{In}\}$ is the structure's internal force, $\{R_i\}$ is the force residual for the iteration. A single solution iteration is depicted graphically in _Figure 3.9.

If $\{R_i\}$ is zero at every degree of freedom in the model, point a in Figure 3.8 would lie on the load-deflection curve and the structure would be in equilibrium. In a nonlinear problem $\{R_i\}$ will never be exactly zero, so if $\{R_i\}$ is less than a force residual tolerance at all nodes, the solution would be accepted as being in equilibrium.

If $\{R_i\}$ is less than the current tolerance value, $\{F\}$ and $\{F_i^{In}\}$are considered to be in equilibrium and $\{u_{i+1}\}$ is a valid equilibrium configuration for the structure under the applied load. However, before ABAQUS/Standard accepts the solution, it also checks that the last displacement correction, $\{\Delta u_i\}$, is small relative to the total incremental

displacement. If is greater than a fraction of the incremental displacement, ABAQUS/Standard performs another iteration. Both convergence checks must be satisfied before a solution is said to have converged for that time increment. The iteration continues until convergence is achieved, as show in Figure 3.10, and the final solution could be obtained through the many above procedures.

In ABAQUS, both load control and displacement control are allowed. In load control method, the applied load, $\{F\}$, is known, unknown DOF, $\{u\}$, is found by solving the equation 3.14 in forms as following equation,

$$\{\Delta u\} = [K^T]^{-1}(\{F\}-\{F^{In}\}) \qquad (3.17)$$

where $[K^T]^{-1}$ is the invert tangent stiffness matrix. This method works well until the solution process reaches the maximum value point. At this point, the $[K^T]$ becomes singular and the solution path diverges. In displacement method, one or more DOF are known, and the remaining unknown increment of DOF could be solved using the same equation 3.17. The advantage of this method is that because one or more DOF is know, only reduced tangent stiffness matrix obtained from $[K^T]$ need to be inverted, and the $[K^T]$ will never turn out singular. Therefore, a solution will always be found with this method.

The key feature in the experiment is the loading case. From the loading-stroke curves, after the peak loading points, the loading capacity of the pipe specimen decreased while the deformation continued to increase. This is consistent with the displacement control scheme. Hence, displacement control method is used in the model.

3.2.9 Convergence

In ABAQUS/Standard structure stress analysis, four parameters checked for convergence are force, moment, displacement and rotation. For example, convergence is obtained when size of the residual (disequilibrium) force is less than a tolerance times a reference value and/or when the size of the increment in displacement is less than a tolerance times a reference value. In this model, only default tolerance values are used. For some difficult cases, it is often necessary to increase the number of increments and/or use some solution

controls. Sometimes nonmonotonic convergence may occur because of various nonlinearities interaction, for example, the combination of friction, nonlinear material behavior, and geometric nonlinearity may lead to nonmonotonically decreasing residuals. In this case, some controls in the time increment such as increase the number of equilibrium iterations for residual check and the number of equilibrium for a logarithmic rate of convergence check may be used to get convergence.

Automatic incrementation scheme is selected because ABAQUS/Standard will automatically adjust the size of the time increments to solve nonlinear problems more efficiently based on the initial time step defined. It may increase the time increment when convergence is easily obtained. On the other hand, ABAQUS/Standard will abandon the increment and starts again with the increment size set to 25% of its previous value if the solution has not converged within certain numbers of iterations or if the solution appears to diverge.

Table 3.1 Typical Material Properties from Coupon Tests by Das *et al.* (2002)

Nominal Strain (%)	Nominal Stress (MPa)
0.09	175
0.19	350
0.67	377
1.45	390
2.45	407
3.54	421.1
8.0	442.0
12.46	451.76
33.03	313.51

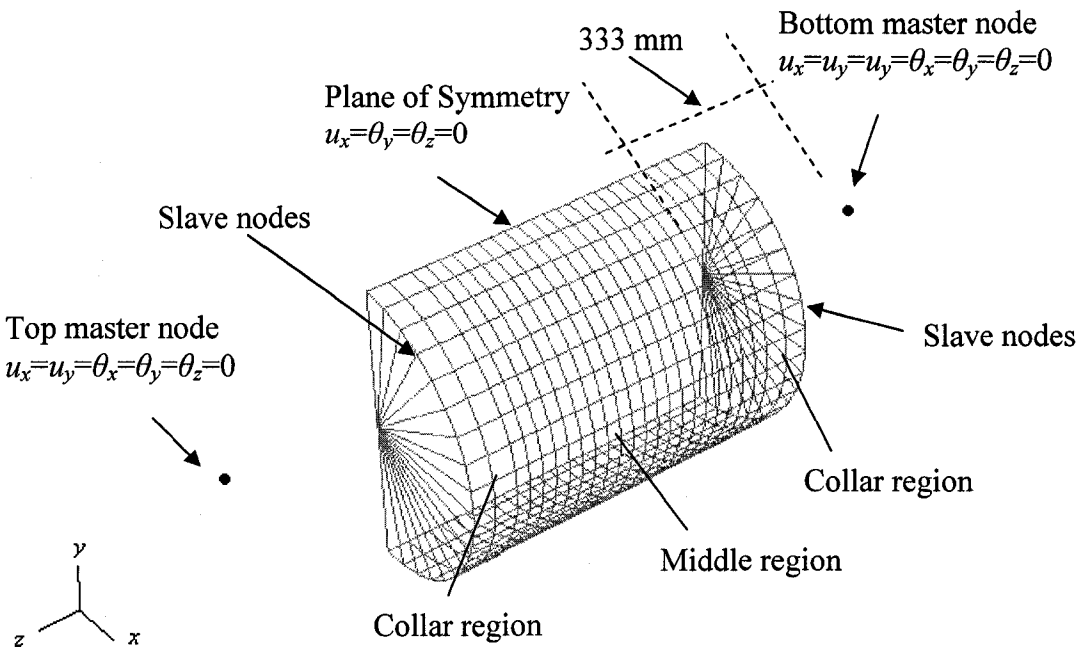

Figure 3.1 Typical Mesh and Boundary Conditions of the Pipe Segment

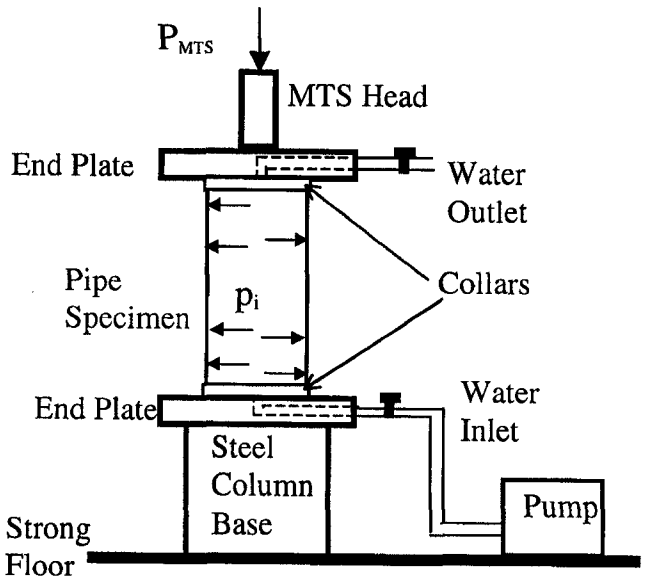

Figure 3.2 A schematic of test setup (Das *et al.* (2002))

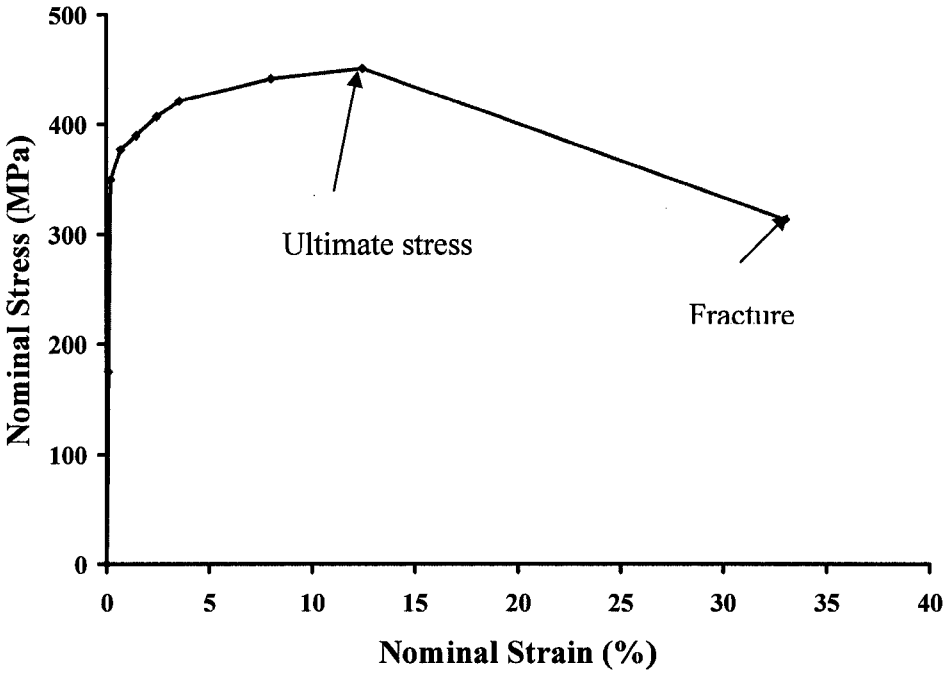

Figure 3.3 Typical Nominal Stress-Strain Behavior (Das *et al.* (2002))

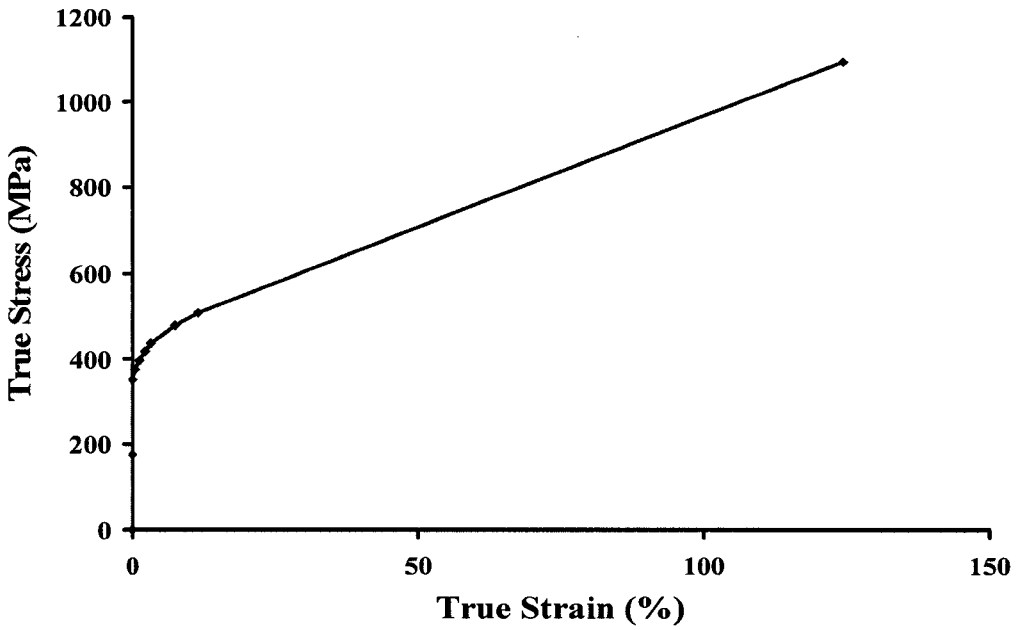

Figure 3.4 Typical True Stress-Strain Behavior (Das *et al.* (2002))

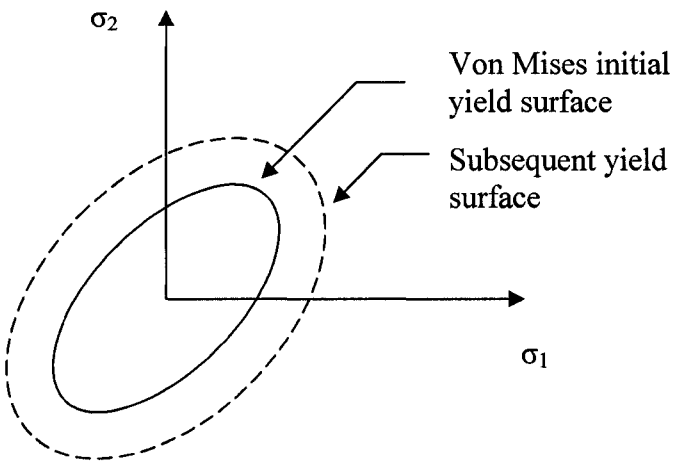

Figure 3.5 2-D Von Mises' Yield Surface and Isotropic Work Hardening

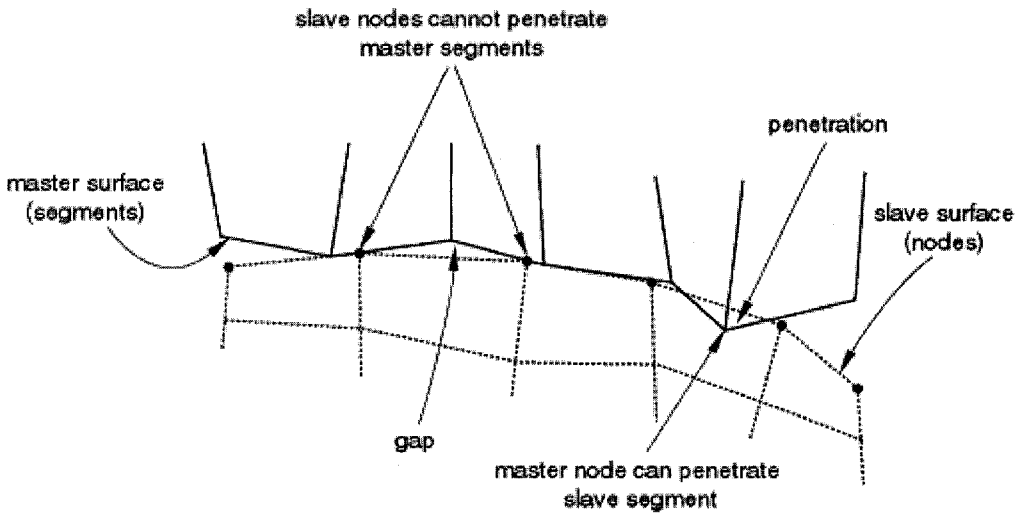

Figure 3.6 Slave-Master Contact Algorithm

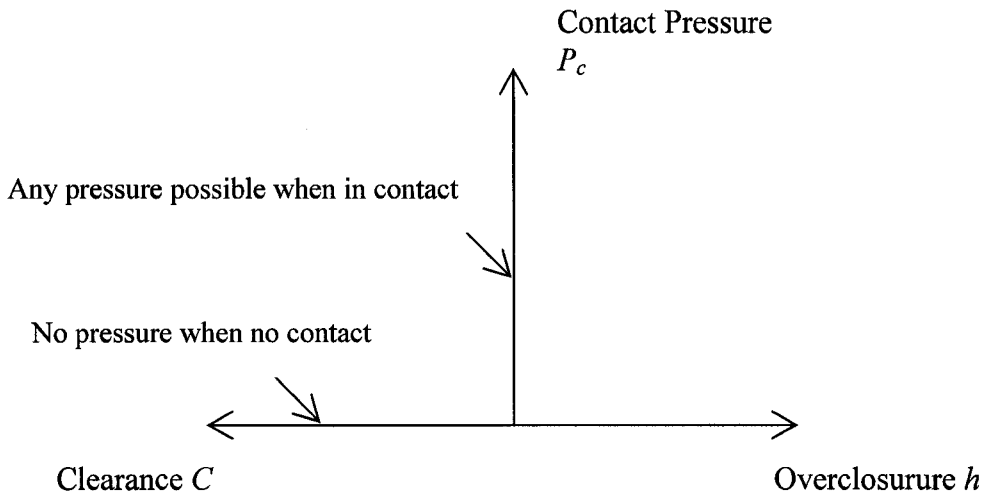

Figure 3.7 Pressure-overclosure Relationship for "Hard" Contact

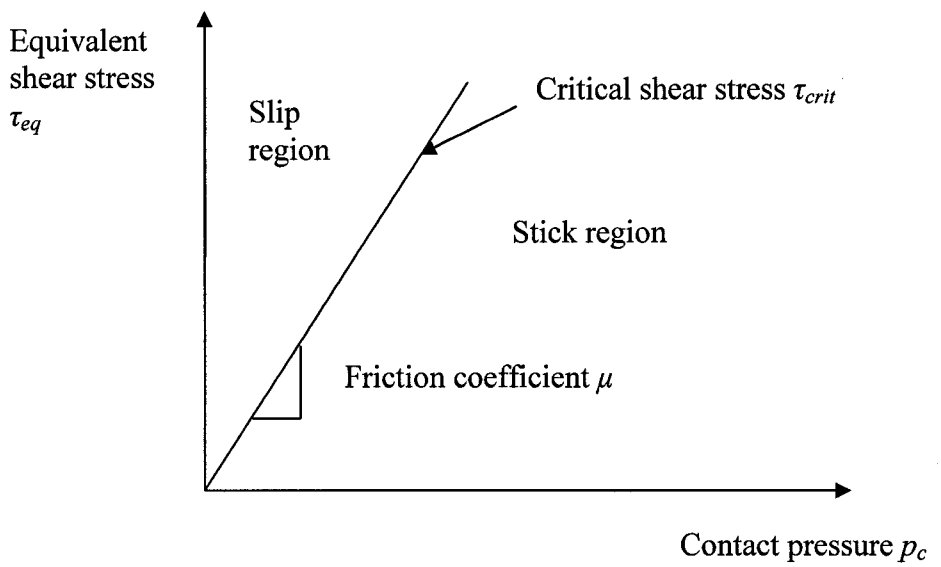

Figure 3.8 The Standard Coloumb Friction Model

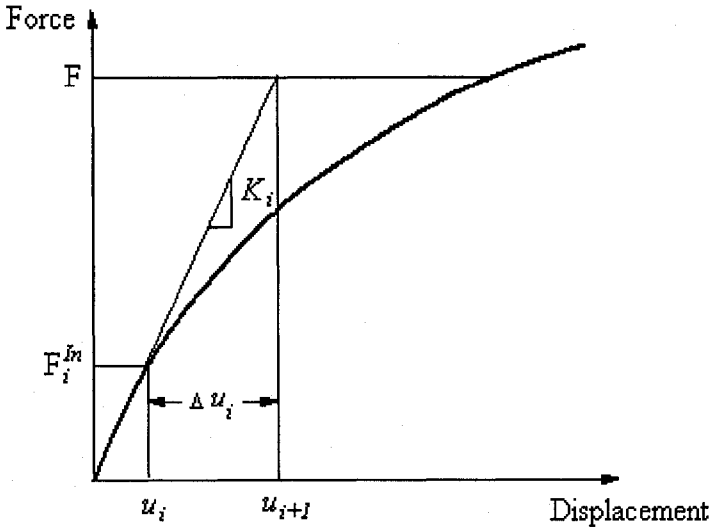

Figure 3.9 One Iteration in Newton Method

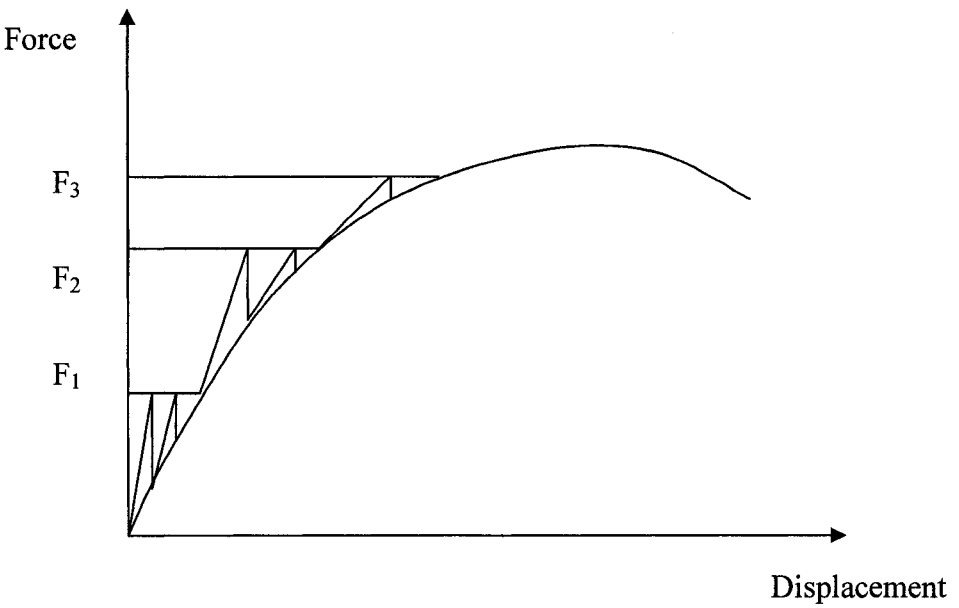

Figure 3.10 Newton Method

4 FINITE ELEMENT ANALYSIS MODEL VALIDATION

Test data obtained from laboratory tests (Das *et al.* (2002)) were used to validate FEA model. This chapter discusses the data obtained from FE analyses and compared these with those obtained from two specimen results. Wrinkling behavior, deformed shape, the load-global strain relationship, the load global stoke relationship, maximum compression and tensile strain, strain distribution, and extensometer strain are compared. Good correlation was obtained between results obtained from FEA and experiments.

4.1 INTRODUCTION OF EXPERIMENTAL PROGRAM

4.1.1 Test Setup

Two 16 inch (406 mm) NPS12 (nominal diameter of 12 in or 305mm) pipe specimens were used to carry out the tests by Das *et al.* (2002) under monotonic axi-symmetric axial load and internal pressure. The pipe wall thickness was 6.84 mm. The schematic of the test setup is shown in Figure 3.2. The axial load P_{MTS} was applied by the MTS loading machine and the internal pressure P_i was applied by the fluid pump. Two collars made of the same pipe specimen were installed at each end of the pipe to prevent buckling because of end effect (residual stress or stress concentration). Each collar was 50 mm long. The thickness of end plate was 75 mm each.

The first specimen was subjected to an internal pressure of 80% of P_y (also written as 0.8 P_y), where P_y is the required internal pressure to cause yield stress developed in the circumferential direction of the pipe material, then was applied to monotonic axi-symmetric axial force while internal pressure keeping constant until one wrinkle formed and the load from the load stroke curve start to increase again (Figure 4.1). The second specimen was subject to an internal pressure of $0.4P_y$. Next the pipe specimen was subjected to monotonic axi-symmetric axial force keeping internal pressure constant until two wrinkles formed (Figure 4.2).

4.1.2 Data Collection

Instruments such as strain gauge, clip gauge, and extensometer were used to record strains when pipe specimens deformed. Commercial electrical resistance strain gauges of 5 mm gauge length were used to measure local strains in longitudinal and circumferential directions. Figure 4.3 shows the relative locations of the strain gauges (Nos. 1 through 19 and Nos. 20 through 39), with respect to the wrinkle crest and feet. Extensometer is a custom-made stain measuring instrument. It was installed on the pipe specimen after the wrinkle formation was clearly visible. It measured the local strain over the entire length of the wrinkle. The axial load applied by MTS machine and the corresponding MTS stroke, which was same as the shortage of the length of the pipe specimen, were recorded by digital data acquisition system.

4.2 COMPARISON FEA AND EXPERIMENTAL RESULTS

4.2.1 Basic Concepts of Measurement

4.2.1.1 Global strain

The global strain describes the deformation of the pipe specimen as a whole. The global strain (ε_g) also called overall strain, is defined in percentage as

$$\varepsilon_g = \frac{L}{\Delta L} \times 100$$

where L is the original length of the pipe specimen, and ΔL is the change in the length of the pipe specimen.

The total change in the length of the pipe specimen ΔL obtained from the experimental data is the stroke added on the pipe specimen, while in the FEA model is same as the displacement of the top of the pipe.

4.2.1.2 Extensometer strain

The extensometer measured the wrinkle strain locally. This strain is also not the really material strain. The extensometer measured the change in the amplitude of the wrinkle in the longitudinal direction according to change of the relative displacement between the two feet of the wrinkle.

The extensometer strain (ε_{ex}) is defined in percentage as

$$\varepsilon_{ex} = \frac{\Delta L_{ex}}{L_{ex}} \times 100$$

where L_{ex} is the length of the extensometer, and ΔL_{ex} is the change in the length of the extensometer.

The ΔL_{ex} in the extensometer strain from the FEA model is by collecting the displacements of two points at the wrinkle feet, then calculating its relative displacement.

4.2.2 Specimen 1

The test 1 was discontinued when first winkle closed from inside the pipe wall. The FE analysis was stop discontinued at this stage. Comparison between the test and FEA results is discussion in following sections.

4.2.2.1 Load deformation relationship

The load deformation behavior of the first specimen that observed from Test 1 is presented in Figure 4.1, similar behavior is observed from the numerical analysis and the results are shown in Figure 4.4. A good correlation is observed from the tests and FE analysis in global load-stroke behavior. The maximum load obtained from the test is about 6.67% higher than the analytical value. The stiffness of the elastic curve that is obtained from the numerical analysis (See Figure 4.4) is generally higher than that from the test (See Figure 4.1). Subsequently, the stroke corresponding to the maximum MTS

load (P_{max}) for analytical model is a little lower than that for test specimen. These differences may be due to introduction of imperfection in the numerical model. The maximum load and the corresponding stroke are almost the same as those observed in the test if no imperfection is used. However, for this model with no imperfection, the wrinkle location is different from that observed in the test.

4.2.2.2 Deformed shape

In the test, a bulge wrinkle was formed near the bottom collar of the pipe. The mid-height of the bulge (wrinkle) is called the crest of the wrinkle. The two ends of the bulge (wrinkle) are feet of the wrinkle. Following the increasing stroke, the bulge (wrinkle) grew bigger in the circumferential direction while in the longitudinal direction the two feet of the pipe became closer. A similar behavior in wrinkle growth was observed from FE analyses. Deformed shapes obtained from FEA model corresponding highest load point (H_1), lowest load point (L_1), and one (Point I_1) in between these two points in Figure 4.1 and Figure 4.4 are shown in Figure 4.6 to Figure 4.8.

4.2.2.3 Strain gauge strain

The strain data obtained from the test indicates that the biaxial tension-tension strain condition exited at the crest of the wrinkle while biaxial tension-compression strain condition exited at two feet of the wrinkle. At the feet of the wrinkle, the biaxial tension-compression strains were circumferential tension strain and longitudinal compression strain. The FEA model also confirmed this. However, due to the limitation of the test, the strain distribution observed in the test was only outside of the pipe specimen. FE analysis, however, shows that the inside wall of the pipe specimen also experienced biaxial tension conditions. Inside wall of the pipe specimen, biaxial tension-tension strain condition was found in the feet of the wrinkle and biaxial tension-compression strain condition in the crest of the wrinkle.

The stroke-strain relationship for the strain gauge strain depending upon their position relative to the wrinkle configurations as shown in Figure 4.3. Three longitudinal and circumferential strain gauge strains at three different locations are selected to compare their stroke-strain relationships from tests with their corresponding FEA results.

The longitudinal stroke-strain relationship obtained from test and that obtained from FEA for gauges at Locations 18, 14 and 2 are compared as shown in Figure 4.9 and Figure 4.10, respectively. The gauges at Location 38, 25 and 30 are compared with their circumferential stroke-strain relationship from test results and that from FEA results as shown in Figure 4.11 and Figure 4.12 respectively. A good correlation is observed from these two groups of figures.

The gauges at Location 18 and 38 (see Figure 4.6) are remote from the wrinkle. The strains in these remote gauges remain constant once one passes the highest load limit point, as the bulge continues to deform under monotonic increasing stroke as shown in Figure 4.9 and Figure 4.11. Similar observation is obtained from FEA results (Figure 4.10 and 4.12).

The longitudinal gauge at Location 14 is at the foot of the wrinkle. The longitudinal strain increased nonlinearly until the end of this loading segment, the strain stabilizes, shows very little growth with additional stroke. Longitudinal gauge at Location 2 is slightly away from the foot of the wrinkle. Hence, the strain value continues to increase in a similar fashion but to al lower rate and then stabilizes. Similar strain behaviors are also observed FE analyses (Figure 4.9 and 4.10).

The circumferential gauge at Location 25 is close to the foot of the wrinkle. It is observed from Figure 4.11, after formation of the wrinkle began, the strain stabilized and did not change much even though wrinkle grew further. Similar result is also observed from FE analysis. The circumferential gauge at Location 30 is close to the crest of the wrinkle and hence, strain continues to increase until it reaches a relatively high strain value and then

the strain stabilizes. Similar relationship is observed from the FE analysis (Figure 4.11 and 4.12).

4.2.2.4 Extensometer strain

The extensometer strain was obtained from the test. The relationship between extensometer strain and global strain is shown in Figure 4.13. A linear relationship between global strain and extensometer strain is observed from Figure 4.13. The extensometer was installed after initiation of the wrinkle. Thus the start point of the extensometer strain in the plot is non-zero. The value of extensometer strain depends on the length of strain gauge. For the Test 1, 4 inch (100mm) extensometer stain gauge was used. Therefore the similar extensometer strain value to global strain relationship was obtained using the 4 inch (100mm) gauge length from numerical analysis as shown in Figure 4.14. Good correlation is observed between the experiment results and numerical analysis results.

4.2.2.5 Maximum strain

The maximum strains obtained from devices such as strain gages and the extensometer in Test 1 were compared with the results from the FEA model (Table 4.1). The maximum longitudinal compressive strain from strain gage observed from the test was 17.31% and the maximum circumferential tensile strain observed from this test was 7.92%. The maximum longitudinal compressive strains and the maximum circumferential tensile strains were obtained from outside pipe wall at the foot and the crest of the wrinkle, respectively, similar observation is obtained from the FEA modeling. However, the absolute maximum values of localized strains in the longitudinal and circumferential direction found from the FE analyses are 52.91% and 28.45%, respectively. This is because the strain gauges in the test were not located at the maximum (critical) strain locations.

4.2.3 Specimen 2

The Test 2 was discontinued when the second wrinkle closed from the inside the pipe wall. The FE analysis was also discontinued at this stage. Comparison between the test and FEA results is discussed in the follow sections.

4.2.3.1 Load and global stroke relationship

The load deformation behavior of the Specimen 2 that observed from Test 2 is presented in Figure 4.2, similar behavior is observed from the numerical analysis and the results are shown in Figure 4.5. A good correlation is observed from the tests and FE analysis in global load-stroke behavior. The first peak MTS load and second peak MTS load obtained from the test were 3026 KN and 2770 KN, respectively and the corresponding analytical peak MTS load were 2885 and 2779 KN, respectively (Figure 4.2 and 4.5). It is observed that the first peak MTS load obtained from the test is 6.17% higher than the analytical value while the second peak MTS load obtained from the test is almost same as the analytical one. As it is described in the Specimen 1, the stiffness of the elastic curve that is obtained from the numerical analysis before the first peak load (See Figure 4.5) is generally higher than that from the test (See Figure 4.2). Subsequently, the stroke corresponding to the first peak MTS load (P_{max1}) for analytical model is a little lower than that for test specimen. These differences may also due to the introduction of imperfection in the numerical model and collar effect during simulation. Since the collar was simulated with elastic material and twice thickness as the elastic-plastic material pipe, it triggered wrinkle to form closer to the collar.

4.2.3.2 Deformation shape

The deformed shapes of Specimen 2 at various load/deformation stages are displayed and compared with corresponding deformed shapes obtained from numerical analysis in Figure 4.15 to Figure 4.18. Figure 4.15 shows the deformed shape of Specimen 2 when the first wrinkle formed apparently. Subsequent deformed shapes obtained from FEA

model and test corresponding the first minimum loading point L_1, one (Point I_2) in between point H_2 (the second maximum loading) and point L_2 (the second minimum loading and also the end of the test), and at point L_2 in Figure 4.2 and Figure 4.5 are shown in Figure 4.16 to Figure 4.18. A reasonable correlation between deformed shapes obtained from the test and FE analyses are found from these figures.

4.2.3.3 Strain gauge strain

The strain distribution fashion in the Test 2 is similar to the observation that obtained from the Test 1. Biaxial tension-tension strain condition exited at the crest of the wrinkle while biaxial tension-compression strain condition exited at two feet of the wrinkle for both wrinkle formed in the test. At the feet of the wrinkle, the biaxial tension-compression strains were circumferential tension strain and longitudinal compression strain. The FEA model also confirmed this. The comparison between the strain distribution observed in the test and that from FEA model is only at outside wall of pipe specimen. FE analysis however, shows that inside wall of the pipe specimen also experienced biaxial tension-tension strain condition was at the feet of the wrinkle and biaxial tension-compression strain condition at the crest of the wrinkle.

Three longitudinal stroke-strain relationships obtained from test and their corresponding values obtained from FE analyses for gauges at Location 3, 18, and 19 were shown in Figure 19 and Figure 20, respectively. The circumferential strain gauge at Location 27 is compare its stroke-strain relationships obtained from test with that obtained from FE analyses as shown in Figure 20 and Figure 21, respectively. It is observed that good correlation is obtained between test and FE analyses.

The longitudinal gauge at Location 3 is close to the bottom foot of the first wrinkle and hence, it shows relatively high compressive strain. The strain increases nonlinearly to its maximum value (before the second wrinkle forms), after maximum strain point, it decreases rapidly linearly, then the strain remains constant at this location (since the MTS load reaches the second peak value) as shown in Figure 4.19. Similar observation is

obtained from analytical model as shown in Figure 4.20. The longitudinal gauges at Location 18 and 19 are remote from the first wrinkle location, and hence during the formation of first wrinkle, strains at these locations remain constant. With the formation of the second wrinkle, the locations of these gauges are changed to Location 5 and 16 respectively relative to the second wrinkle as shown in Figure 4.6. Therefore, the strains in these longitudinal gauges are increased. Similar strain behaviors were also observed from FE analyses (Figure 4.20). However, the maximum value of strain gauge 19 is higher than that observed from test, since the gauge 19 stopped working shortly before stopping add stroke.

The circumferential gauge at Location 27 is situated close to the crest of the first wrinkle and hence, it shows increase in tensile strain until it stabilizes. Then it reduces by a small value which shows a small strain release because of strain localization at crest of the wrinkle while wrinkle gets flatter. The strain remains almost constant during the process of the formation of the second wrinkle (Figure 4.21). Similar results are observed from the FE analyses (Figure 4.22).

4.2.3.4 Extensometer strain

The relationship between extensometer strain and global strain is shown in Figure 4.23. A monotonically increasing compressive strain until the second wrinkle starts to form was observed from Figure 4.23. The start point of the extensometer strain in the plot is similar to that in the Test 1. For Specimen 2, 3 inch extensometer stain gauge was used. Therefore, similar extensometer strain value to global strain relationship was obtained using the 3 inch gauge length from numerical analysis as shown in Figure 4.24. Good correlation is observed between the experiment results and numerical analysis. It is observed that the local extensometer strain obtained from FE analyses increases almost linearly with increasing of global strain which is a little different from the test results. It is coincident with the tendency of the wrinkle formation. When wrinkle forms, the distance between two feet is becoming closer and closer and corresponding extensometer

compressive strain is getting lower. The results observed in Figure 4.23 from the test may be caused by inaccurate movement of extensometer gauge.

4.2.3.5 Maximum strain

The maximum strains obtained from strain gages and extensometer for Test 2 were compared with the values obtained from the FE analyses (Table 4.2). The maximum longitudinal compressive strain and the maximum circumferential tensile strain observed from strain gauge in this test is 17.86% and 7.2%, respectively. The maximum longitudinal compressive strains and the maximum circumferential tensile strains were obtained at the foot and the crest of the wrinkle, respectively. However, the absolute maximum longitudinal compressive strain and circumferential tensile strain obtained from FE analyses which were 76% and 22.95% respectively are much higher than those obtained from test. This is because in the tests the strain gauges could not be located at the critical points and this is one of the limitations of the experimental study.

4.3 SUMMARY

The previous chapter presented numerical modeling and solution techniques of the monotonic axi-symmetric load test specimens. The model is able to simulate highly complicated plastic strain history of pipeline structure with accordion type of wrinkling. This chapter presented the results obtained from the FEA and compared those results with the test results. The comparisons show that a numerical tool like ABAQUS is able to simulate these test results successfully if might choices are made for various aspects of modeling and solution techniques. Comparisons between test results and FEA results are good for both specimens. To the best of knowledge of the author, no other work on this type of numerical modeling has been done elsewhere. This model is the first of its kind but may not the best possible numerical model.

Table 4.1 Comparison FEA and Experimental Maximum Strain Values for Specimen 1

Source of Results	Maximum Overall Strain (%)	Maximum Local Strain (%)		
		Longitudinal Strain from		Circumferential Strain from
		Strain Gauge	Extensometer (gauge length)	Strain Gauge
Experiment	-24.6	-17.31	-36.60 (4 inch)	+7.92
FEA	-25.8	-17.40	-36.76	+7.92

Table 4.2 Comparison FEA and Experimental Maximum Strain Values for Specimen 2

Source of Results	Maximum Overall Strain (%)	Maximum Local Strain (%)		
		Longitudinal Strain from		Circumferential Strain from
		Strain Gauge	Extensometer (gauge length)	Strain Gauge
Experiment	-43.6	-17.86	-52.0 (3 inch)	+7.2
FEA	-44.8	-17.90	-53.25	+7.2

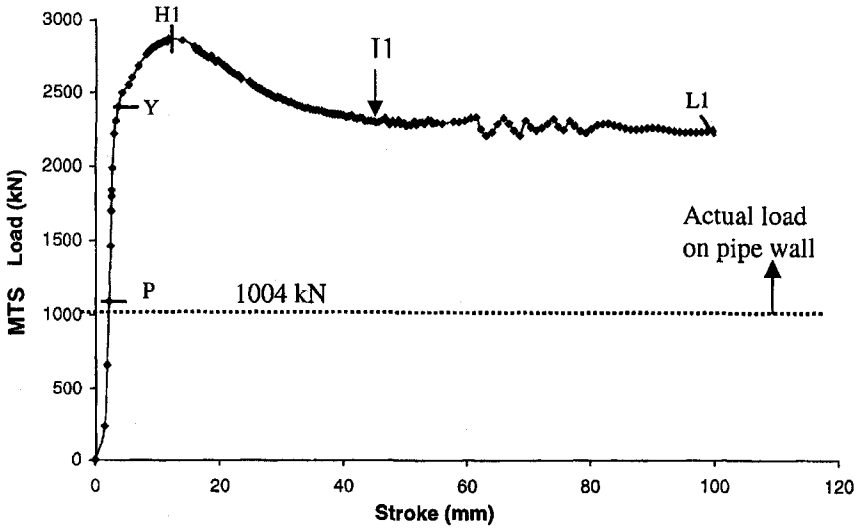

Figure 4.1 MTS Load vs. MTS Stroke for Specimen 1 from test (Das *et al.* (2002))

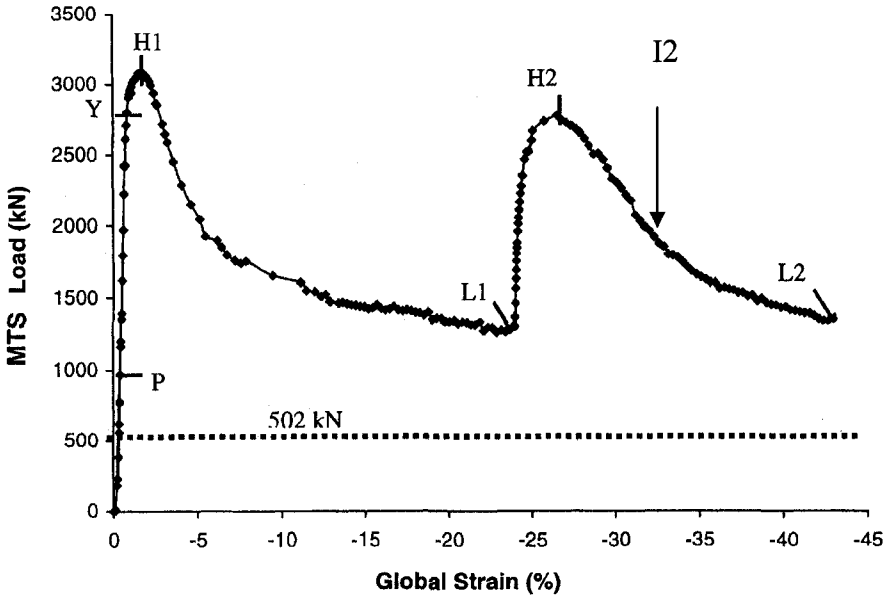

Figure 4.2 MTS Load vs. MTS Stroke for Specimen 2 from test (Das *et al.* (2002))

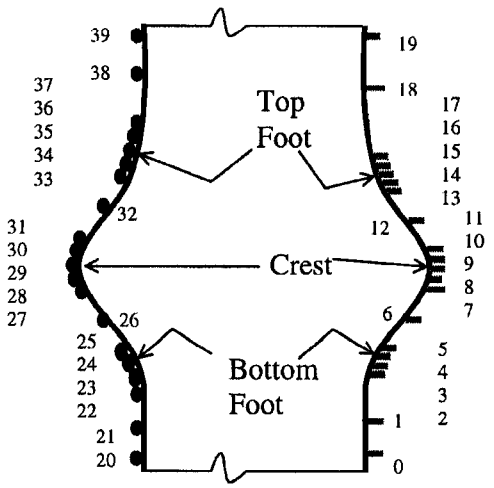

Figure 4.3 Typical Layout of Strain Gauges (Nos.0 to 19 are for longitudinal strains and 20 to 39 are for circumferential strains) from Das *et al.* (2002) tests

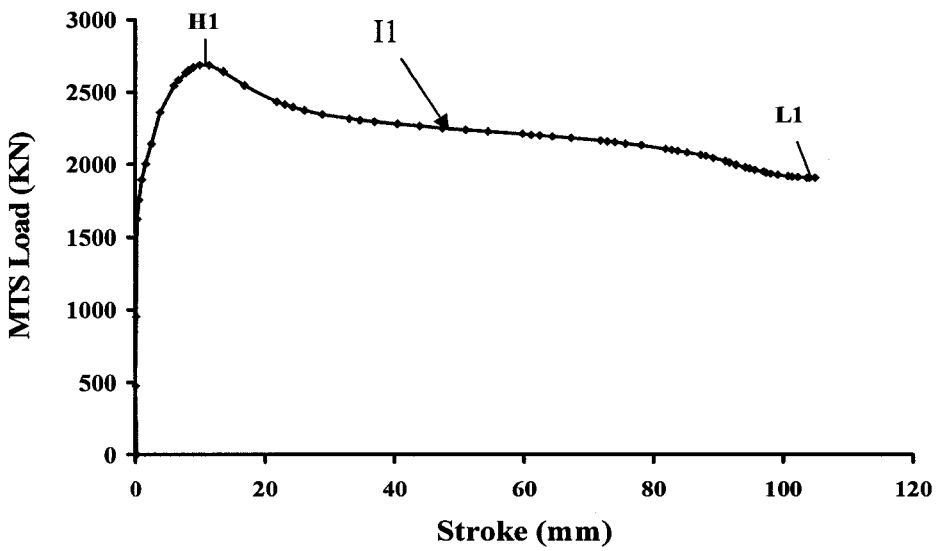

Figure 4.4 MTS Load vs. MTS Stroke for Specimen 1 obtained from FEA

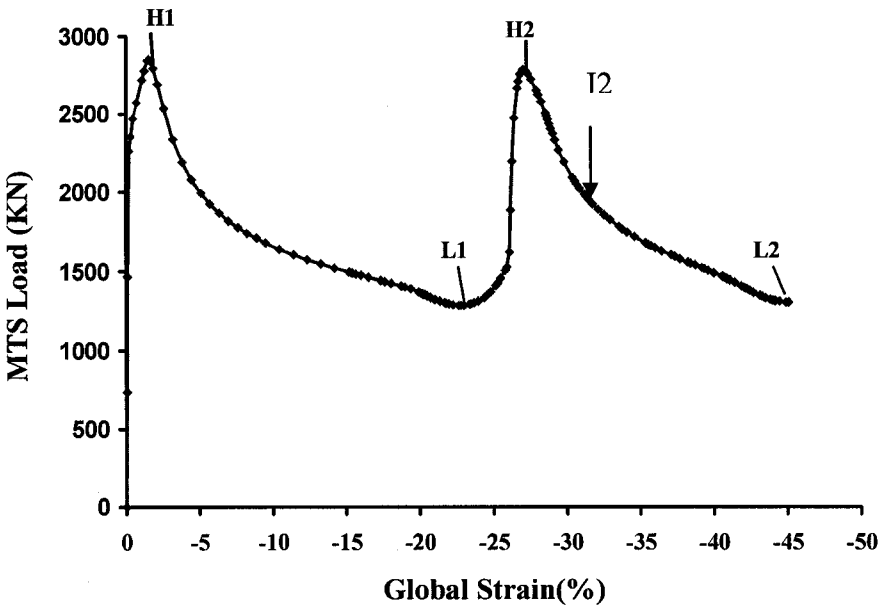

Figure 4.5 MTS Load vs. MTS Stroke for Specimen 2 obtained from FEA

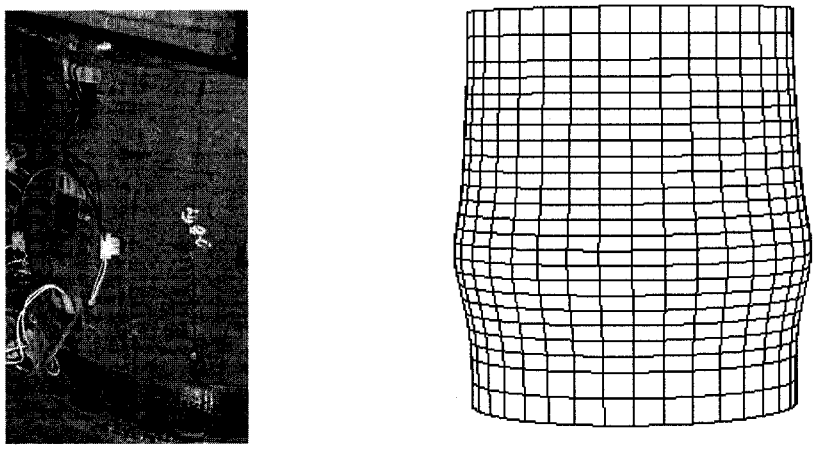

TEST FEA

Figure 4.6 Deformed Shape of Specimen 1 at Point H_1

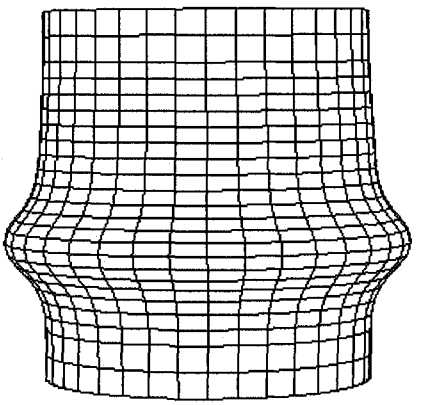

FEA

Figure 4.7 Deformed Shape of Specimen 1 at Point I_1

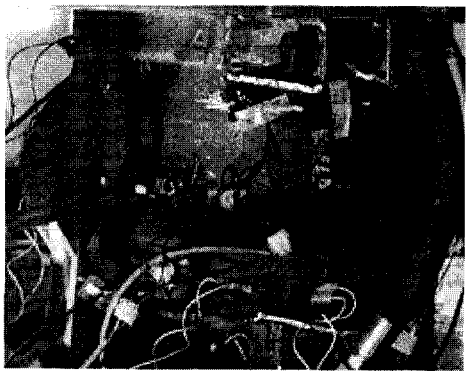

TEST

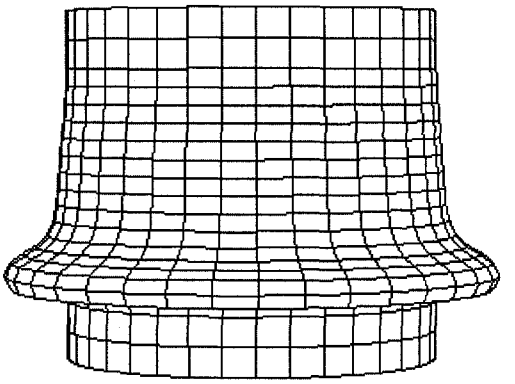

FEA

Figure 4.8 Final Deformed Shape of Specimen 1

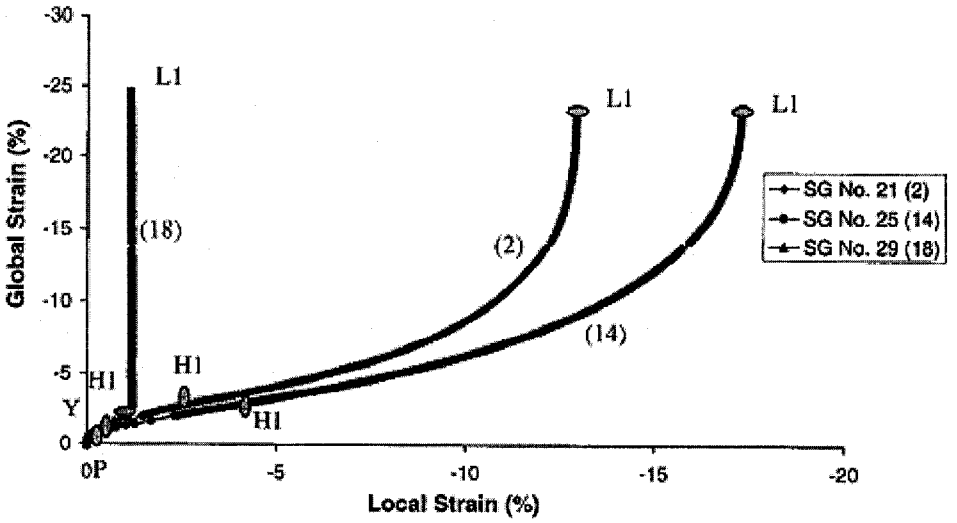

Figure 4.9 Local Longitudinal Strain vs. Global Strain for Specimen 1 from test (Das *et al.* (2002))

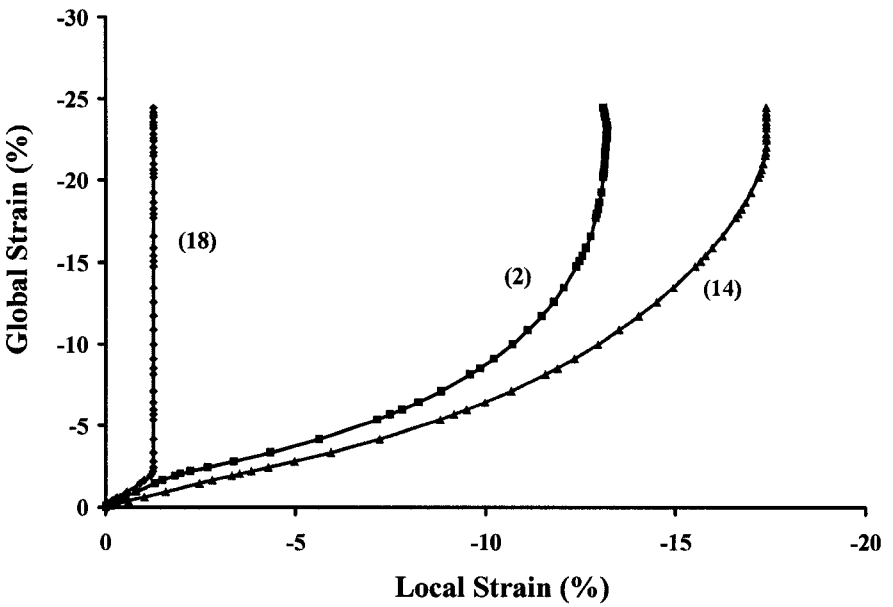

Figure 4.10 Local Longitudinal Strain vs. Global Strain for Specimen 1 from FEA

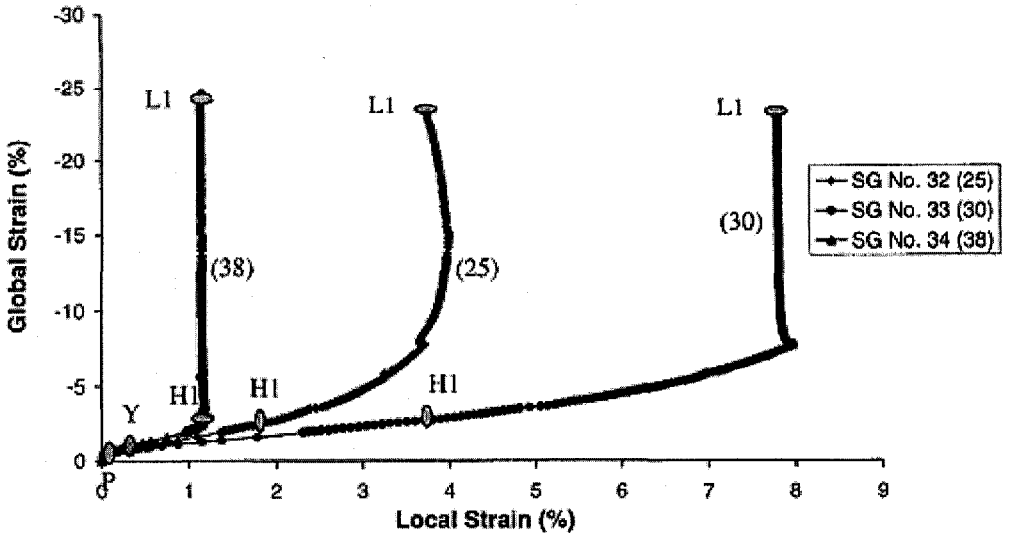

Figure 4.11 Local Circumferential Strain vs. Global Strain for Specimen 1 from test (Das *et al.* (2002))

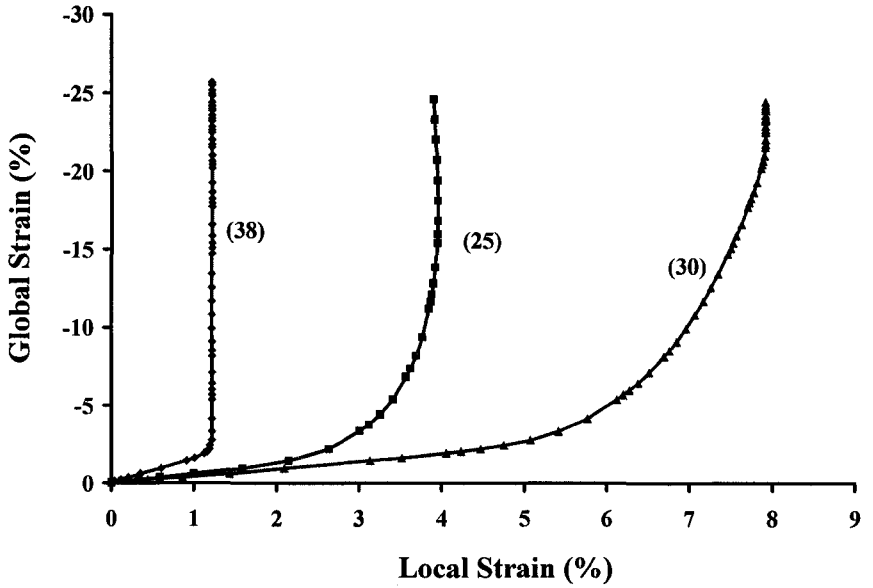

Figure 4.12 Local Circumferential Strain vs. Global Strain for Specimen 1 from FEA

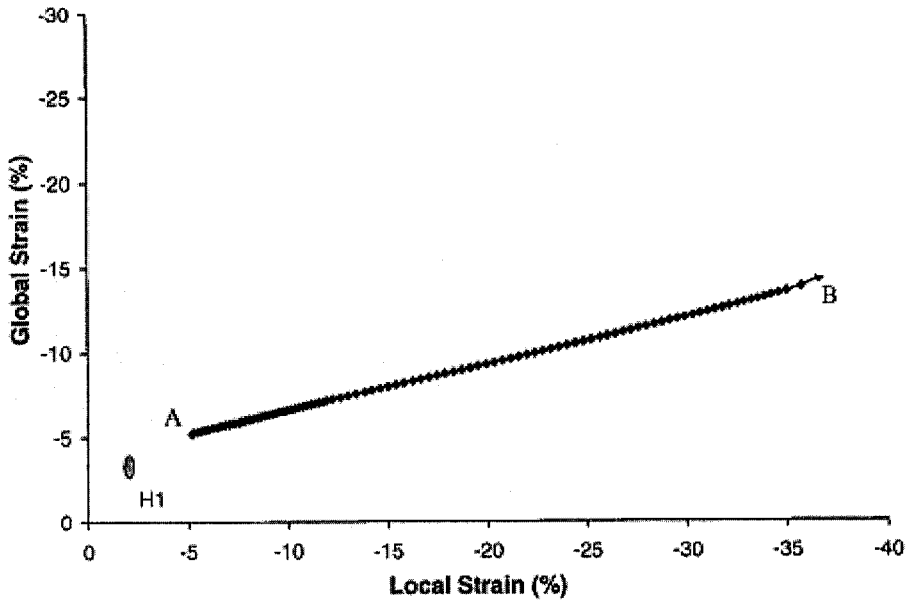

Figure 4.13 Extensometer Strain vs. Global Strain for Specimen 1 from test (Das *et al.* (2002))

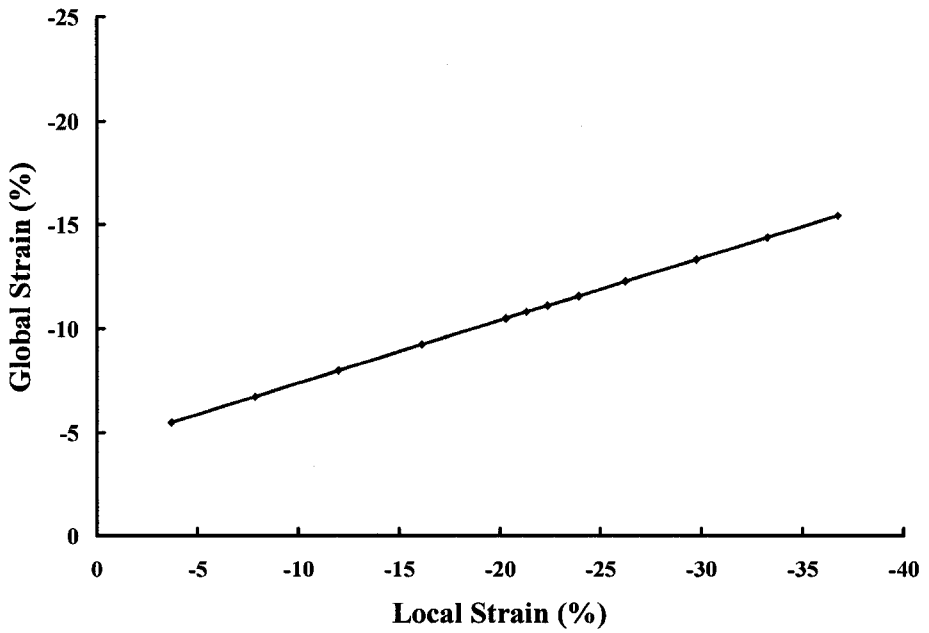

Figure 4.14 Extensometer Strain vs. Global Strain for Specimen 1 from FEA

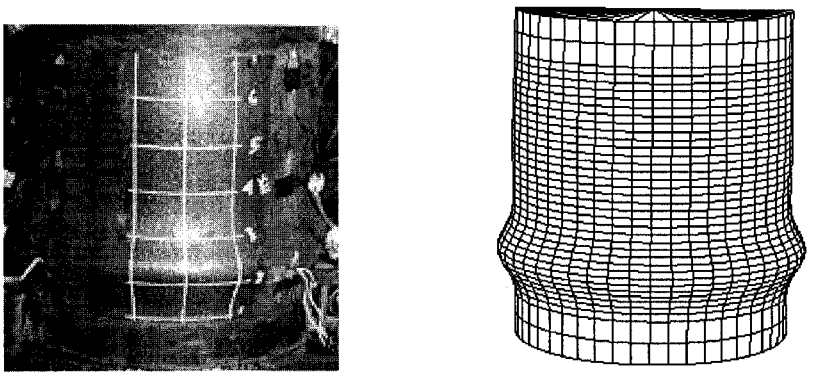

TEST FEA

Figure 4.15 Deformed Shape of Specimen 2 when one wrinkle forms

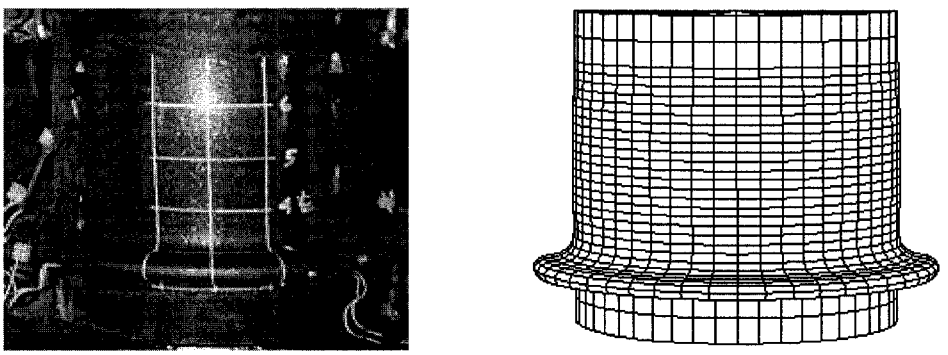

TEST FEA

Figure 4.16 Deformed Shape of Specimen 2 at Point L_1

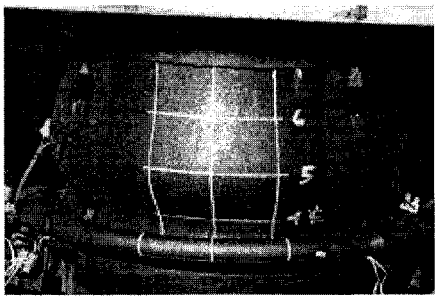

TEST

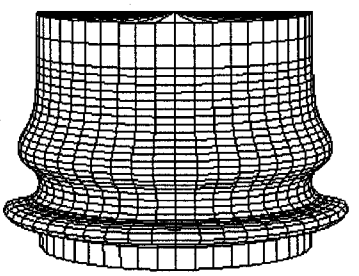

FEA

Figure 4.17 Deformed Shape of Specimen 2 at Point I_2

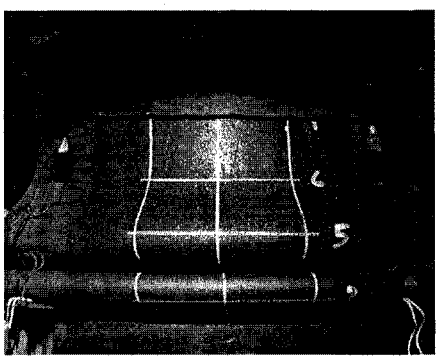

TEST

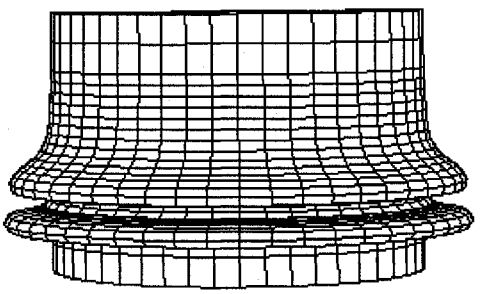

FEA

Figure 4.18 Final Deformed Shape of Specimen 2

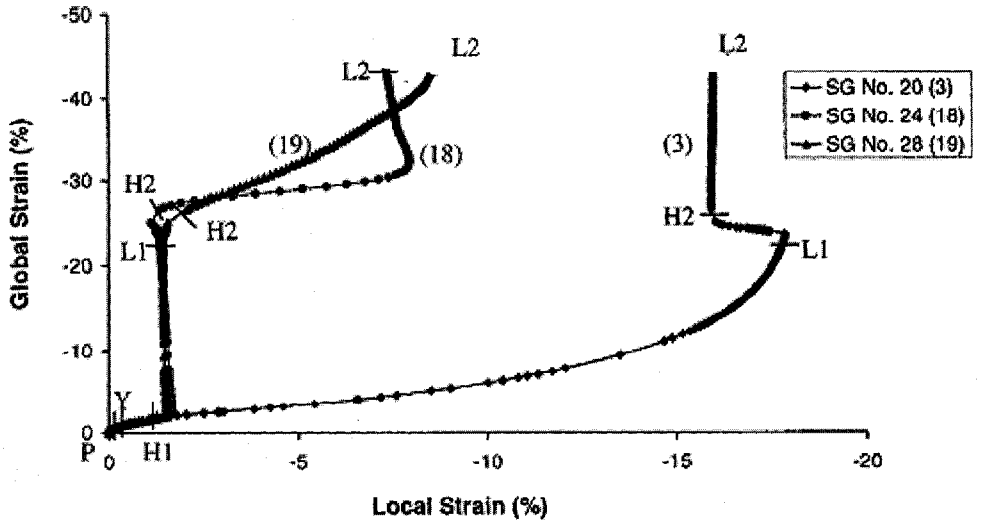

Figure 4.19 Local Longitudinal Strain vs. Global Strain for Specimen 2 from test (Das *et al.* (2002))

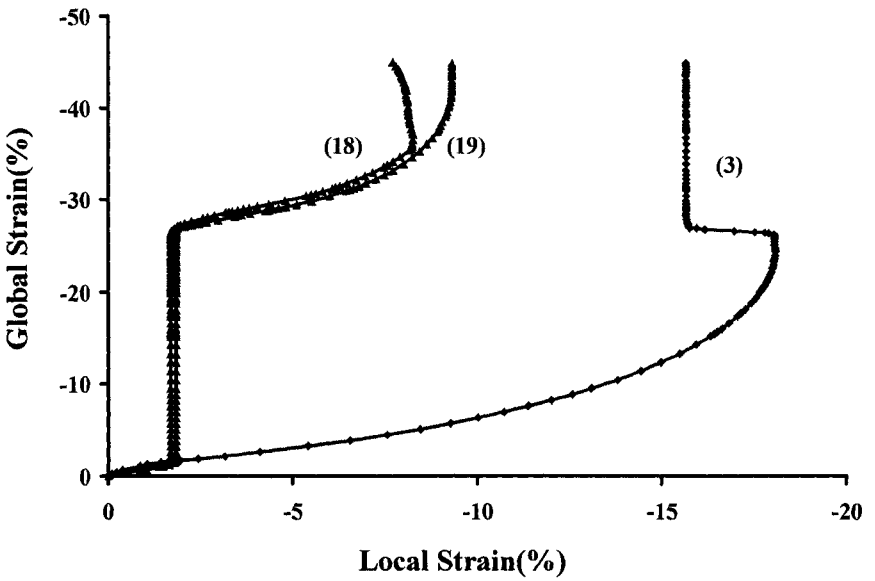

Figure 4.20 Local Longitudinal Strain vs. Global Strain for Specimen 2 from FEA

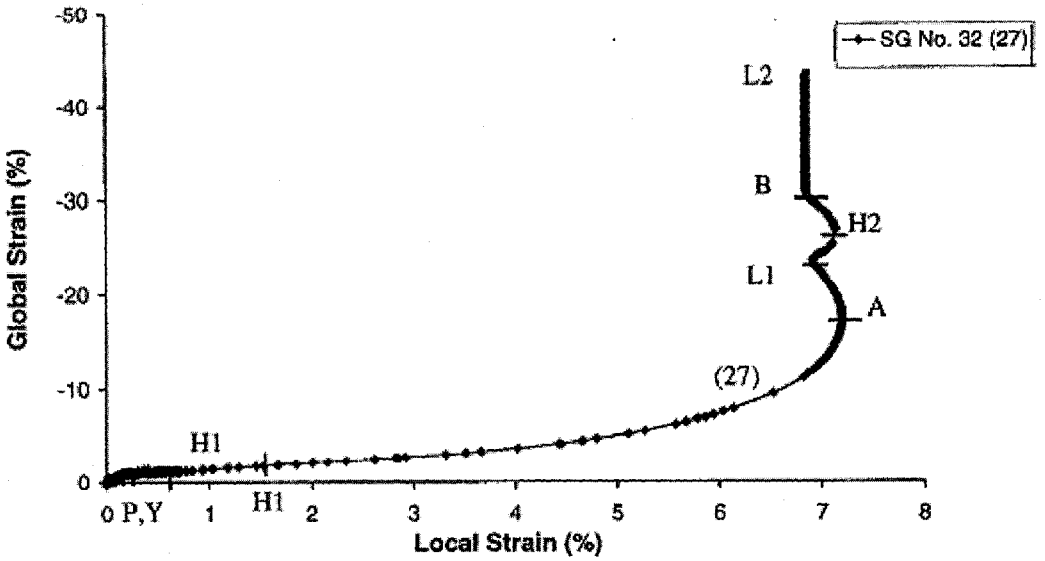

Figure 4.21 Local Circumferential Strain vs. Global Strain for Specimen 2 from test (Das *et al.* (2002))

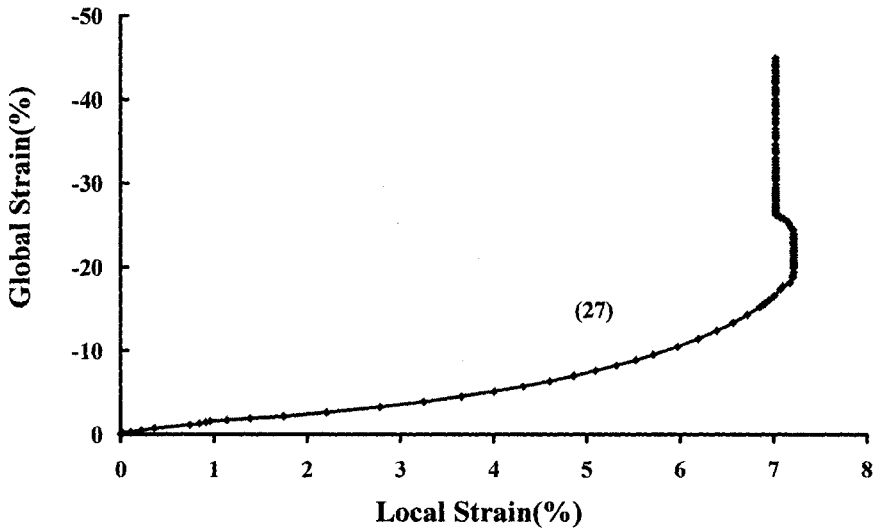

Figure 4.22 Local Circumferential Strain vs. Global Strain for Specimen 2 from FEA

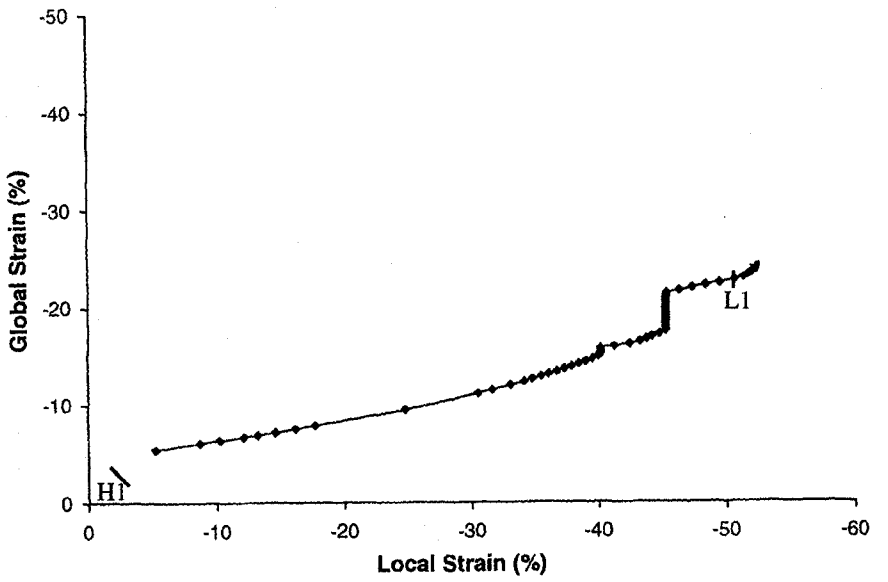

Figure 4.23 Extensometer Strain vs. Global Strain for Specimen 2 from test (Das *et al.* (2002))

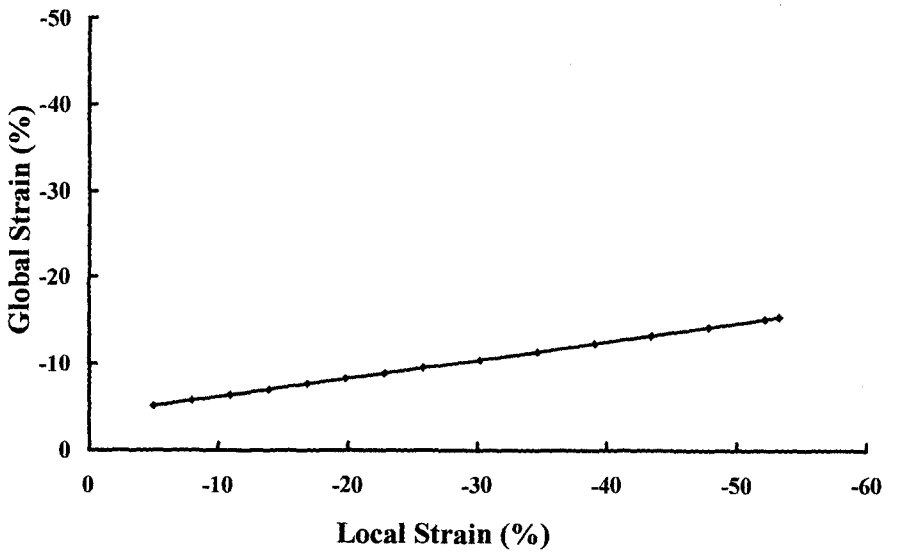

Figure 4.24 Extensometer Strain vs. Global Strain for Specimen 2 from FEA

5 MATERIAL TEST MODELING

This chapter makes a brief description on the material coupon tests and numerical analyses to obtain material properties. Under the scope of this project, numerical simulation and analysis of these material tests were done using same finite element code, ABAQUS. The purpose of the numerical analysis is to set up a fracture criterion for numerical models of pipe specimens.

5.1 TESTS FOR MATERIAL PROPERTIES

The material properties of the two axisymmetric loading specimens discussed in Chapter 4 were obtained by tension coupon tests (Das *et al.* (2002)). The tension coupon specimens were cut from same pipe specimen of *D/t* ratio of 45 and X52 grade steel (SMYS=358 MPa), prepared and tested according to ASTM Standard A370-94 (1994) specifications. Four tension coupon specimens with gauge length of 50 mm and width of 12.5 mm were made. All the specimens were cut from the longitudinal direction of the pipe and from a segment away from the seam and girth welds to avoid any residual stress effect on the material behaviors. Two electrical resistance (120Ω) strain gauges of 5 mm gauge length were installed on either face of the specimen and a clip-on extensometer of 50 mm gauge length was also installed on one face of the specimen to obtain strains.

The load and overall deformation curve was recorded for each specimen throughout the range of deformation until rupture occurred from MTS loading machine. A typical load-deformation curve for a tension coupon specimen is shown in Figure 5.1. Loading was held four times during each test to obtain the static points of the load-deformation curve. The extensometer was taken out before necking became considerable to avoid any damage in it. The strain gauges ceased to function before ultimate load was reached. A typical stress-strain behavior obtained from these tension coupon tests is shown in Table 3.1 and Figure 3.3 in Chapter 3.

5.2 NUMERICAL MODEL FOR MATERIAL TESTS

The numerical analysis models (an ABAQUS/Standard model and an ABAQUS/Explicit model) for simulating material tests used the same commercially available finite element analysis code ABAQUS Version 6.6-2, details of these models are discussed in the following sections.

5.2.1 Material Model

Two material models were used in this numerical modeling and analysis. The middle 50 mm portion of the coupon specimen was modeled as elastic-plastic material based on test data obtained from material tests. The two end portions of the coupon specimen were assumed to be elastic.

5.2.2 Finite Element Mesh

The element used in this model is S4R, which was also used in pipe model. The two ends of the coupon used coarse mesh while the middle of the coupon which has the same length of the 50 mm gauge length used finer mesh. However, for the 50 mm gauge length, a uniform mesh was used in the ABAQUS/Standard model and a non-uniform mesh was used in the ABAQUS/Explicit model as shown in Figure 5.2 and Figure 5.3, respectively. A non-uniform mesh for the ABAQUS/Explicit model was chosen because this type of mesh produced a good correlation to the coupon tests.

5.2.3 Boundary Conditions and Loading Conditions

The nodes of the right end of the coupon specimen were constrained from all rotational and translational degrees of freedom to simulate the real test condition. The nodes on other end (left end) of the coupon specimen had one degree of freedom in x axis direction only (Figure 5.2 and Figure 5.3).

The load was applied through the application of displacement at the left end nodes of the coupon specimen in the x direction.

5.2.4 Failure Model

The shear failure model was used to simulate the coupon fracture failure. This failure model is available in ABAQUS/ Explicit, and it is not available in ABAQUS/Standard. This shear failure model is based on the value of the equivalent plastic strain at element integration points. A failure is assume to occur when the damage parameter (ω) exceeds 1. The damage parameter (ω) is defined as

$$\omega = \frac{\bar{\varepsilon}_0^{pl} + \sum \Delta \bar{\varepsilon}^{pl}}{\bar{\varepsilon}_f^{pl}} \tag{5.1}$$

where, $\bar{\varepsilon}_0^{pl}$ is initial equivalent plastic strain, $\Delta \bar{\varepsilon}^{pl}$ is an increment of the equivalent plastic strain, $\bar{\varepsilon}_f^{pl}$ is the equivalent plastic strain at failure that must be defined. The equivalent plastic strain $\bar{\varepsilon}^{pl}$ is defined as

$$\bar{\varepsilon}^{pl} = \bar{\varepsilon}_0^{pl} + \int_0^t \dot{\bar{\varepsilon}}^{pl} dt \tag{5.2}$$

where, $\dot{\bar{\varepsilon}}^{pl}$ is the equivalent plastic strain rate.

When the shear failure criterion is met at an integration point, all the stress components are set to zero and that particular material point fails. If all of the material points at any one section of an element fail, the element is removed from the mesh by option. For S4R shell elements, all through-the-thickness integration points must fail before the element is considered failed and removed from the mesh.

In the coupon test model, there is no initial plastic deformation, and thus the value of $\bar{\varepsilon}_0^{pl}$ in Equation (5.1) is zero. Because the increment of the equivalent plastic strain ($\Delta \bar{\varepsilon}^{pl}$) increased monotonically, the summation of increment of the equivalent plastic strain

($\sum \Delta\bar{\varepsilon}^{pl}$) is equal to equivalent plastic strain ($\bar{\varepsilon}^{pl}$). Therefore, failure occurs when the equivalent plastic strain ($\bar{\varepsilon}^{pl}$) equals to equivalent plastic strain at failure ($\bar{\varepsilon}_f^{pl}$).

5.3 FAILURE CRITERIA DEFINITION

The shear failure model and the option for deletion of failed elements are available in ABAQUS/Explicit only. However, the parametric study of pipe specimens under axi-symmetric loading and deformation discussed in the following chapter were performed in ABAQUS/Standard. Serious attempts were made for numerical simulations and analysis of pipe specimen using ABAQUS/Explicit. The deformation shapes and load-deformation behavior obtained from these dynamic (explicit) analyses were much different from what were observed from the laboratory tests. A failure criterion that is similar to the one discussed in section 5.2.4 that determines fracture in the pipe specimens was required to be determined. This was done as follows.

First, the material (coupon) tests were simulated and analyzed using ABAQUS/Explicit to obtain the maximum equivalent plastic strain (MEP strain) at failure ($\bar{\varepsilon}_f^{pl}$). Next, the same material (coupon) tests were simulated and analyzed analytically using ABAQUS/Standard and applying same boundary and load conditions to obtain the MEP strain at failure ($\bar{\varepsilon}_f^{pl}$) to check if this value agrees well with that obtained from Explicit solution technique. If the values obtained from Explicit and Standard solution techniques agree well, the MEP strain at failure ($\max \bar{\varepsilon}_f^{pl}$) obtained from ABAQUS/Standard analysis of coupon specimen can be considered as the fracture failure criteria for pipe specimens that were analyzed using ABAQUS/Standard.

5.4 RESUTLS AND DISCUSSIONS

This section discusses the calibration of the numerical models for coupon tests and the final results which will be used to determine the failure criterion of the pipe specimens in parametric study in the next chapter.

The FEA models were validated by comparing the results obtained from the ABAQUS/Standard model and ABAQUS/Explicit model with the results obtained from the coupon tests in forms of MTS load and stroke curves as shown in Figure 5.1, Figure 5.4 and Figure 5.5. Figure 5.1 is the MTS load and stroke curve obtained from coupon tests by Das *et al.* (2002); Figure 5.4 is the MTS load and stroke curve obtained from ABAQUS/Standard model; and Figure 5.5 is the MTS load and stroke curve obtained ABAQUS/Explicit model.

It can be seen that load-deformation behavior obtained from the ABAQUS/Standard model and ABAQUS/Explicit model have good correlation with those obtained from tests, although the behaviors (Figure 5.4 and Figure 5.5) obtained from two numerical models have minor differences as comparing to test behavior (Figure 5.1). The maximum MTS loads from the numerical analyses are slightly higher than experimental value. Figure 5.4 shows that the MTS load from the point of highest load to the fracture point is decreased more quickly than that in Figure 5.1. This may be because the material model for numerical analysis used a linear behavior in stress-strain between ultimate stress point and fracture point as show in Figure 3.4. It is also observed from Figure 5.5 that the load-deformation behavior between yield and ultimate load points is almost linear. The test data, however, shows a non-linear behavior (Figure 5.3). This difference may be due to the dynamic (explicit) solution technique.

The final deformed shapes from both ABAQUS/Standard model and ABAQUS/Explicit model are shown in Figure 5.6 to Figure 5.8. Figure 5.6 shows the final deformed shape of coupon specimen in ABAQUS/Standard model, Figure 5.7 shows the final deformed shape of coupon specimen without deletion of failed (fractured) elements in ABAQUS/Explicit model, and Figure 5.8 shows the final deformed shape of coupon specimen with failed elements deleted in ABAQUS/Explicit model.

It can be seen that the deformed shapes in both models are reasonably similar. The different location of necking in the models is because of the dynamic effect in ABAQUS/Explicit model.

The main objective of modeling and analyses coupon test was to determine the equivalent plastic strain at failure ($\bar{\varepsilon}_f^{pl}$) which could not be obtained from laboratory coupon tests. The equivalent plastic strain at failure ($\bar{\varepsilon}_f^{pl}$) was obtained from numerical analyses of coupon specimen at rupture nominal strain as was applied in the laboratory tests. Two equivalent plastic strain values at failure were obtained from ABAQUS/Standard model and ABAQUS/Explicit model, respectively. The equivalent plastic strain at fracture point from ABAQUS/Standard model is 121.5%, and from ABAQUS/Explicit model is 120.8%, as shown in Table 5.1. The fracture nominal strains applied to the FEA models and test specimen are provided in Table 5.1.

It is observed that the equivalent plastic strains at failure ($\bar{\varepsilon}_f^{pl}$) from both models are very close. Thus, the MEP strain at failure ($\max \bar{\varepsilon}_f^{pl}$) obtained from the coupon specimen using ABAQUS/Standard analysis was considered as the fracture failure criterion for numerical modeling of pipe specimens that were analyzed using ABAQUS/Standard. The numerical analyses of coupon specimens show that fracture occurs when MEP strain at failure ($\max \bar{\varepsilon}_f^{pl}$) is about 120% if a shear failure model as discussed in section 5.2.4 is used. However, for numerical analyses of pipe specimens discussed in Chapter 6, the equivalent plastic strain at failure ($\bar{\varepsilon}_f^{pl}$) has been considered as 100% as a conservative estimate for pipe fracture.

Table 5.1 Results From Coupon FEA Models

Models	Equivalent Plastic Strain at Failure (%)	Nominal Rupture Strain (%)
ABAQUS/Standard Model	121.5	33.16
ABAQUS/Explicit Model	120.8	33.13
Experiment	N/A	33.00

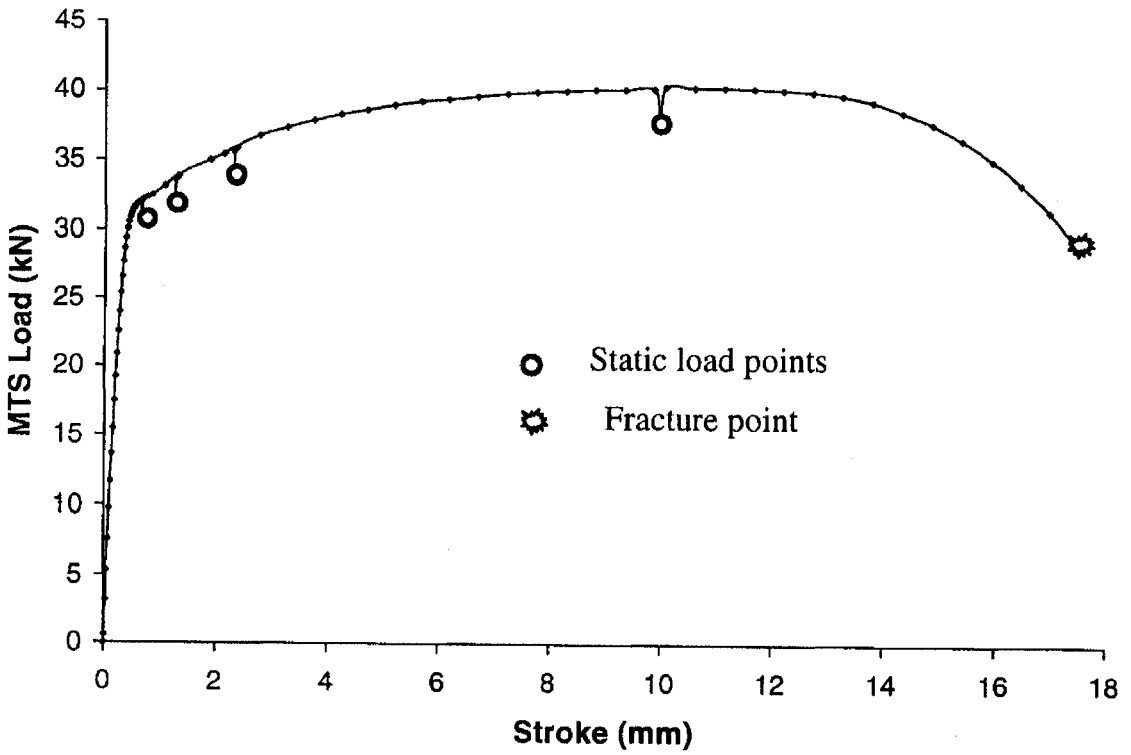

Figure 5.1 Typical Load vs. Stroke plot for a tension coupon specimen (Das *et al.* (2002))

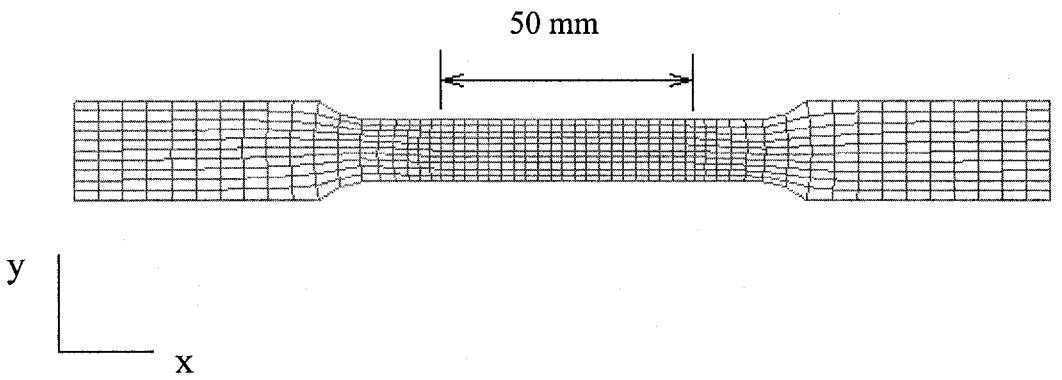

Figure 5.2 Undeformed Finite Element Mesh of ABAQUS/Standard Analysis Model

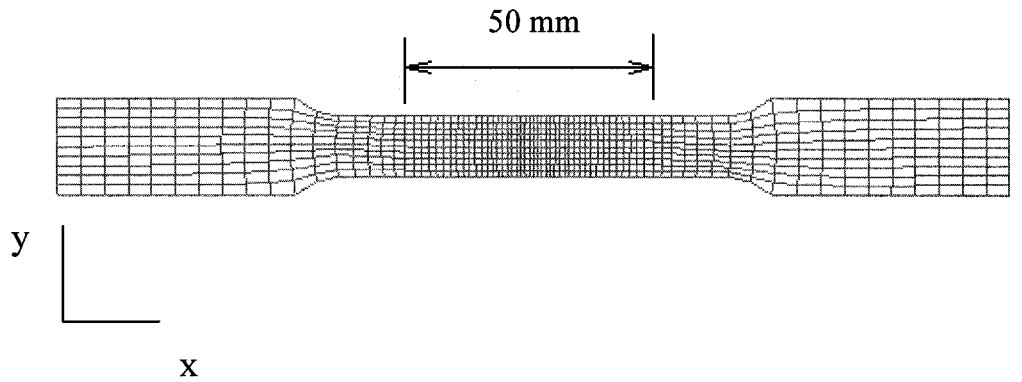

Figure 5.3 Undeformed Finite Element Mesh of ABAQUS/Explicit Analysis Model

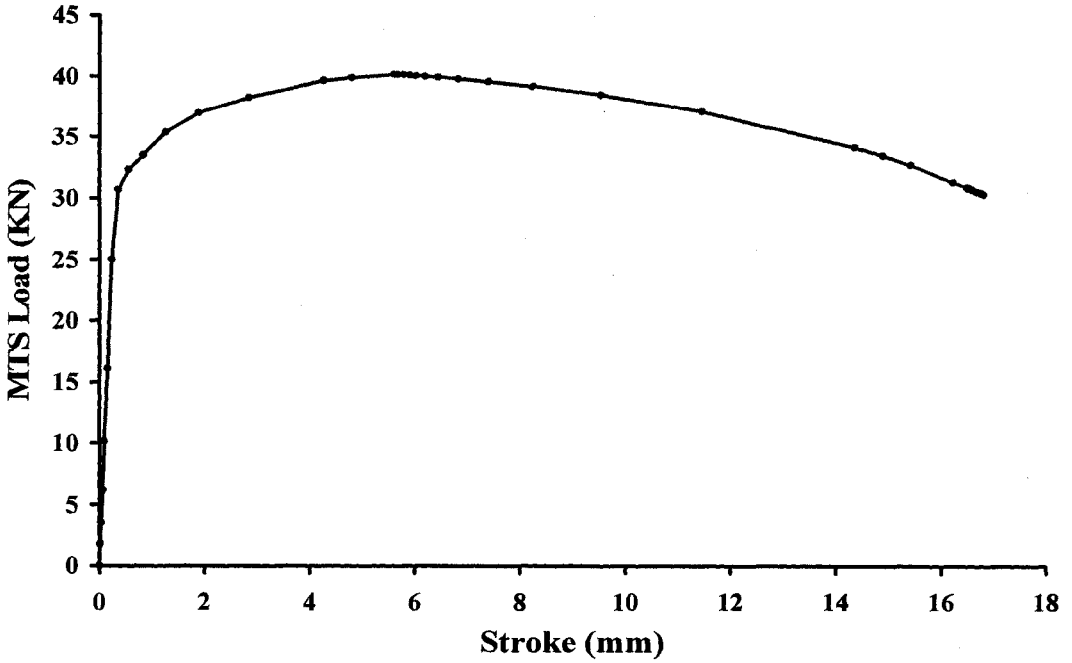

Figure 5.4 Load vs. Stroke plot for a tension coupon specimen from ABAQUS/Standard Analysis Model

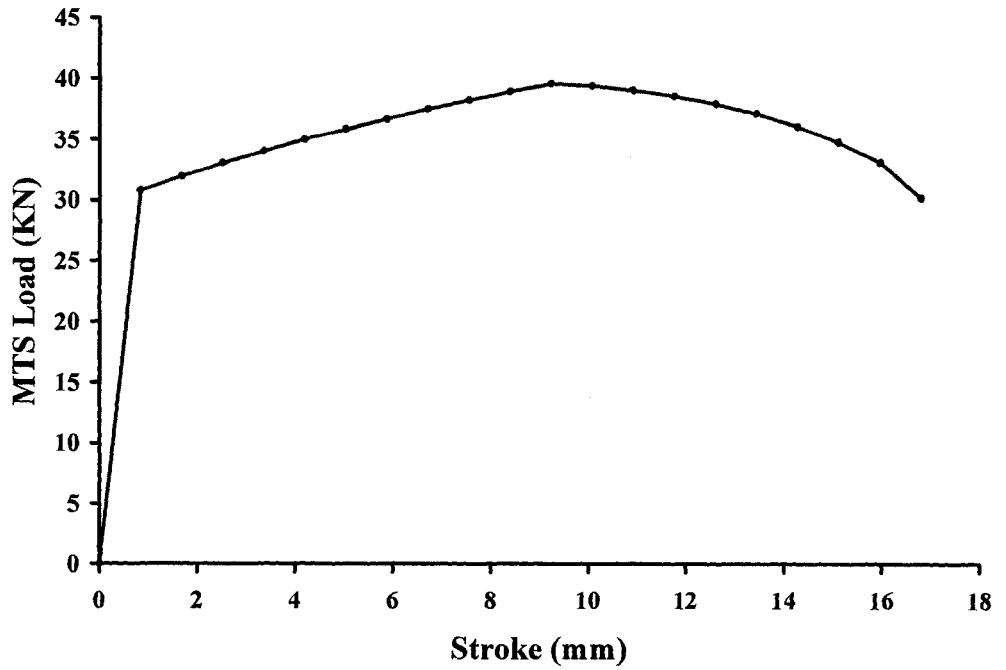

Figure 5.5 Load vs. Stroke plot for a tension coupon specimen from ABAQUS/Explicit Analysis Model

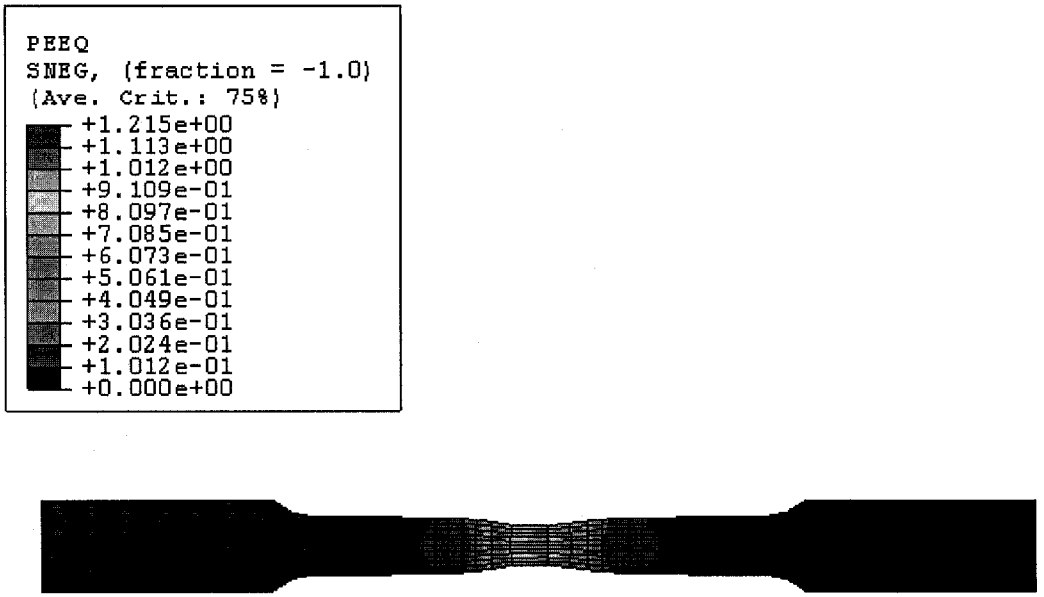

Figure 5.6 Deformed Finite Element Analysis Model (ABAQUS/Standard)

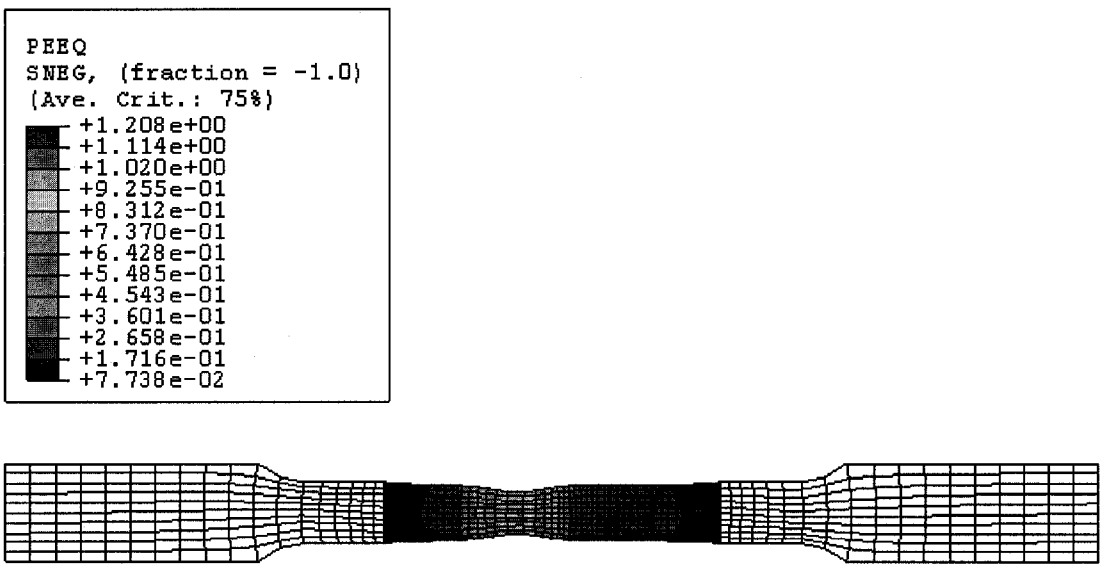

Figure 5.7 Deformed Finite Element Analysis Model (ABAQUS/Explicit)

Figure 5.8 Final Ruptured Coupon Specimen in Finite Element Analysis Model (ABAQUS/Explicit)

6 PARAMETRIC STUDY

In Chapter 3 and Chapter 4, a Finite Element (FE) model which is able to simulate and predict accurately the accordion type wrinkling behaviors of energy pipe has been developed and validated. These behaviors include the load response, buckling configuration, and various strain-stroke responses. However, it may be unrealistic to expect that every pipeline segment will fail due to formation of accordion type of wrinkle and will not experience other failure mode such as rupture. However, an experimental study on every pipeline segment is expensive and time consuming. Therefore, a full spectrum parametric study was performed using the FE model to asses failure modes for various pipelines subjected to axi-symmetric axial monotonic deformation and various internal pressures. Thus, a detailed parametric study was undertaken to determine failure mode and failure conditions for buried steel pipelines with various D/t ratios, various material properties, and various internal pressures. This chapter presents the parameters chosen and the results obtained from the parametric study.

6.1 PARAMTERS

6.1.1 Parameter Selection

From discussion in Chapter 2 and Chapter 4, it is understood that the local buckling is obviously affected by a number of parameters such as pipe diameter D, pipe wall thickness t, material properties such as stress-strain relationship, axial load N, internal pressure P, imperfection, and location of girth weld.

Test procedure for two pipe specimens under monotonic axi-symmetric axial loading and two different internal pressures were discussed in Chapter 4. The geometry and material properties for these specimens were same. The first specimen was subjected to internal pressure of 80% Py, exhibited higher axial load capacity and wrinkle with larger amplitude than the second one which was subjected to about lower internal pressure

(40% *Py*). The amplitude of the bulge buckling seems depending on the magnitude of the internal pressure, it increases internal pressure increases. Therefore, the internal pressure must be an important parameter that affects the axi-symmetric local buckling and should be studied in the parametric study.

Experimental study (Das *et al.* (2002)) shows that the particular pipe specimen did not fracture under axi-symmetric deformation. However, no conclusion on the failure can be made for various other pipelines with various *D/t* ratios and material properties. Thus, the other two parameters: *D/t* ratios and material properties were also chosen for this parametric study.

6.1.2 Parameter Range Selection

6.1.2.1 Range for diameter to thickness ratio (*D/t*)

The field line-pipe currently in-service in Canada have diameter over thickness (*D/t*) ratios ranging from 10 to as high as 120. (Dorey *et al.* (2001)). According to Murray (1996) and Souza and Murray (1999), the typical *D/t* ratio for buried field pipelines are in range of 30 to 100 with diameter in the range 200-1000 mm. Former researchers had conducted studies on local buckling of the pipes with a large range of *D/t* ratios. Mohareb *et al.* (1993, 1994, and 2001) and Yoosef-Ghodsi *et al.* (1995) studied the full sized pipe specimens which had diameter-to-thickness ratios of *D/t* are 64 and 51 with corresponding pipe nominal diameter of 508 mm and 324mm, respectively. DelCol *et al.* (1998) and Dorey *et al.* (2002) investigated full sized pipes with diameter (762 mm) to thickness (8.3 mm) (*D/t*) ratios of 92. Das *et al.* (2002) conducted full-scale NPS12 pipes study with nominal diameter of 324mm and a *D/t* ratio of 47. Smith, M. Q. *et al.* (1998) conducted full size wrinkle test to study the pipes of nominal 48 inch (1219mm) diameter to nominal 0.462inch (11.7mm) thickness and the *D/t* ratio of 104. These researches considered the pipe *D/t* ratio from 47 to 104 for the inland pipeline.

For the lower *D/t* ratios, Vitali, L. *et al.* (1999) created a finite element model to investigate the buckling mechanisms and limit state formulations of pipes of *D/t* ratios 20, 30, 40 and 60. Hauch and Bai (2000) used finite element analysis model to study the ultimate strength and bending moment for the pipes of *D/t* ranged from 10 to 60. Gresnigt *et al.* (2001) carried out four full-scale 20 inch (508 mm) pipe bending tests with *D/t* ratios 45, 27, 22, and 29 to investigate the effect of the manufacturing process on the local buckling behavior of pipe. Two specific cases 24 inch (610 mm) pipe with *D/t* =14.5 and *D/t* =40 were also collected and considered in the research. Vitali, L. *et al.* (2005) also performed four full-scale bending tests on pipes with outer diameter to thickness *D/t* ratios 25.6 and 34.2. The lower range of *D/t* ratios studied covered from 10 to 60. Thus, in the parametric study, the range of *D/t* ratios was chosen from 20 to 110 to consider most of the buried field pipelines.

6.1.2.2 Range for internal pressure ratio (*P/Py*)

The two test specimens used in the previous study as discussed in Chapter 4 had the internal pressure ratio, *P/Py* of 0.8 and 0.4, respectively. Under the field operation condition, the level of the internal pressure in the oil and gas pipelines can range from zero to the maximum operation pressure as indicated in the current design standards. Usually highest internal pressure occurs immediately downstream of the pump station while the lowest internal pressure which is nearly zero can be found immediately upstream of the pump station. As described in the Chapter 1, the internal pressure is controlled by the maximum hoop stress allowed developed in the pipeline. The hoop stress is limited to a portion design factor, *F* to the Specified Minimum Yield Stress (SMYS). According to current design standard, the maximum value of this design factor, *F* is 0.8. (Canadian Standards Association, 2003, CSA-Z662-03, and British Standards, 2004, BSI, PD 8010-1). The internal pressure can be calculated by the equation listed in Equation 3.4. However, the pipeline could expect to endure internal pressure that generate a hoop stress as high as 90% to 105% SMYS during hydrostatic strength test. (British Standards, BSI, PD 8010-1, 2004). Thus, for this study, the highest value of the internal pressure ratio is chosen as 1.0.

The lowest internal pressure could be almost zero. As indicated in Chapter 2, the internal pressure is a major parameter dominant the buckling mode and buckling configurations. There are two distinctly modes of local buckling and the buckling modes are dependent on the internal pressure. When internal pressure is high, an outward bulge shape of local buckling (wrinkling) is usually expected to occur in the pipe wall. If the internal pressure is zero or the pipe is unpressurized, a totally different inward diamond shape of buckling is expected. This second buckling mode is not the major interest in current research, so the lowest limit of the internal pressure ratio was chosen as 0.1.

6.1.2.3 Ranges of material properties

The material used by Das *et al.* (2002) in the experimental test is X52 grade steel and the material property was obtained from coupon (material) tests in forms of nominal stress-strain (or engineering stress-strain) relationship as shown in Table 3.1 and Figure 3.3. This material model will be referred as control material model and its nominal stress-strain curve referred to control stress-strain curve. From the control nominal stress-strain curve, the nominal strain (or engineering strain) at the rupture point was obtained as 33%. Because the purpose of this study is to determine the dependence of rupture or accordion type of wrinkle on the pipe materials behavior, it seems more reasonable to increase and decrease the value of engineering strain at the rupture point to investigate the influence of the rupture strain on pipe failure behavior. The results of this study may not applicable to all kind of steel but can be useful for understanding the influence of the rupture strain of material on pipe failure mode.

Three material models used in parametric study have the same strain-stress relationship until the ultimate stress point in both engineering strain-stress curve and the true strain-stress curve. However, the remaining portions of the three curves are different from each other as shown in Figure 6.1 and Figure 6.2. Three engineering strains at the rupture points of the these material models were chosen as 25%, 30% and 40%, respectively, and the corresponding engineering stresses were obtained by linearly interpolating or

extrapolating the control engineering strain-stress curve (Table 6.1 and Figure 6.1). The corresponding true strain-stress data used in the parametric study for each model were generated by linearly interpolating or extrapolating the controlling true strain-stress behavior (Table 6.2 and Figure 6.2).

6.2 ANALYTICAL MODEL FOR PARAMETRIC STUDY

This section describes choices of various parameters and other important issues related to the parametric study, and the emphasis is to describe three aspects of the model which is the characteristic values describing the load cases, imperfection and location of the wrinkles.

The half-symmetric FE model was used for the parametric studies. It used the same type of elements, material model, boundary conditions, load sequence, contact algorithm, mesh size, and solution strategy that were used in Chapters 3 and 4. Specimens were generated by different diameter to thickness (*D/t*) ratios and internal pressure (*P/Py*) ratios.

6.2.1 Applying of Loads

A total of 190 specimens were generated for various diameter to thickness ratios (*D/t*) and internal pressure ratios (*P/Py*) selected, as shown in Table 6.3. In this parametric study, the diameter is the middle thickness diameter of the pipe specimen, and *Py*, is the internal pressure causing yielding in the circumferential direction of the pipe, was calculated using equation 3.4 based on the yield stress σ_y (367MPa) obtained from the coupon material tests. First, the required internal pressure and axial load were applied. In the next step, the stroke was increased until the wrinkle formed and contacted inside the pipe wall, and this stroke will be called "stroke at contact" later.

6.2.2 Location of the Wrinkles

The wrinkles formed close to the bottom collar of the pipe specimens in the two full scale tests carried out by Das *et al.* (2002) under load of monotonic axi-symmetric axial force, stroke and internal pressure. Therefore, wrinkles were also formed at the same locations in the finite element model for predicting these two tests. However, in the field, because the effect of the collars does not exit, wrinkles may occur anywhere in the pipeline along its length. Based on parametric study, it was observed that the location of the wrinkle close to the collar does have influences on the wrinkle configurations and the value of maximum equivalent plastic strain (MEP strain) at contact ($\bar{\varepsilon}^{pl}_{C\max}$).

The results of this parametric study are presented in Table 6.4, Table 6.5, Figure 6.3 and 6.4. Figure 6.3 presents the effect of wrinkle location on stroke at contact. Figure 6.4 presents the effect of wrinkle location on the value of MEP strain at contact ($\bar{\varepsilon}^{pl}_{C\max}$). The solid curves in both figures represent the results obtained when wrinkles formed near the bottom collar, the dash lines represents the results obtained when wrinkles formed away from the collars. The strokes at contact increases with the increasing internal pressure ratio when keeping *D/t* ratio remain constant (Figure 6.3). The difference between the magnitude of the strokes for lower *D/t* ratio such as *D/t* = 20 is because the collar affects the growth of the wrinkle and wrinkle crest moves downward resulting in higher stroke at contact. The MEP strain at contact ($\bar{\varepsilon}^{pl}_{C\max}$), however do not decrease consistently with increasing internal pressure ratio for a constant *D/t* ratio when the wrinkle formed close to the collar. This is because the growth of the wrinkle was not consistent but differed with the change in the internal pressures. This resulted in the location of MEP strains at contact ($\bar{\varepsilon}^{pl}_{C\max}$) changed as well as the internal pressures changed. This can be observed from Figure 6.5 and Figure 6.6 which are two charts that show MPE strains ($\bar{\varepsilon}^{pl}_{\max}$) for a series of specimens with *D/t* ratios of 20 and 95, respectively. Each plot consists of ten series of specimens in which the only viable that changes among ten curves is the level of internal pressure. Examination of Figure 6.5 and Figure 6.6 shows that the maximum equivalent plastic strain increases with increasing stroke for each level of internal

pressure. However, majority of the MEP strain to stroke relationships shows sharp change in curvature (For example, point A in Figure 6.5) indicates a shift in location of MEP strains. For higher *D/t* ratio (Figure 6.6), some of the MEP strain to stroke relationships (especially for low internal pressure) shows similar quick change in curvature due to the same reason. Therefore, it was decided to force all the wrinkles formed in the middle of the pipe specimen to minimize influence of the collar.

6.2.3 Influence of Imperfection

The main purpose of the parametric study was to obtain the MEP strain during the growth of wrinkle. Since the magnitude of imperfection used to trigger the wrinkle was not same for all the parametric study specimens, it was necessary to study its influence on the magnitude of MEP strains. Thus a detailed parametric study was carried out.

The results of this parametric study are presented in Table 6.6. The imperfection corresponding to the first value in the table is the lowest imperfection needed to trigger the wrinkle formation. It is seen from the table that the MEP strain remains essentially unchanged for a specific specimen, regardless of different imperfection values that were used to trigger the wrinkles. Thus, the imperfection did not influence the MEP strain value. Therefore, the lowest possible value of imperfection was chosen for parametric study.

6.3 RESULTS OF PARAMETRIC STUDY

Once all the analyses for the 190 pipe models were completed for the parametric study, the necessary data (information) was collected and summarized as shown in Table 6.7 and the effects of the different *D/t* ratios, *P/Py* ratios, and material models on the response of the each model were examined. The sensitivity and the effect of different *D/t* ratios, *P/Py* ratios, and material models on the MEP strains ($\bar{\varepsilon}^{pl}_{max}$) were determined. The influence of these parameters is presented in the graphic forms later in this chapter. From

these plots, the general relationship between the *D/t* ratios and MEP strains and relationship between *P/Py* ratios and MEP strains can be observed. These plots will help pipeline industry to determine when and whether rupture failure or accordion type deformation failure will occur for each diameter to thickness ratio (*D/t*) and internal pressure ratio (*P/Py*) knowing the material behavior.

6.3.1 Effects of P/P_y Ratio

6.3.1.1 Effect of P/P_y ratio on maximum equivalent plastic strains

This section investigates the effect of the internal pressure (P/P_y) on MEP strains ($\bar{\varepsilon}^{pl}_{\max}$). The effect of P/P_y on MEP strains will be described in two aspects: (i) the effect of P/P_y on MEP strains at any point of wrinkle formation history, and (ii) the effect of P/P_y on MEP strains at contact.

The effect of P/P_y on MEP strains ($\bar{\varepsilon}^{pl}_{\max}$) at any point of wrinkle forming can be analyzed by plotting MEP strains ($\bar{\varepsilon}^{pl}_{\max}$) as a function of stroke for each specimen. Figure 6.7 to Figure 6.25 present 19 plots showing relationship between stroke and MEP strain at each internal pressure ratio for specimens with *D/t* ratios ranged from 20 to 110 at an increment of 5. The data collected till inside wall of pipe specimens self contacted. Each plot is comprised of a group of ten curves represent ten specimens among which only internal pressure changed.

Examination of Figure 6.7 to Figure 6.25, it can be obviously found that, generally, for each series of curves (one particular *D/t* ratio), the MEP strain ($\bar{\varepsilon}^{pl}_{\max}$) increased nonlinearly as the function of stroke for each internal pressure ratio. Usually the highest equivalent plastic strain observed at the inside wall of the wrinkle crest region. Because at this region, the pipe wall experienced the highest circumferential tensile strain and highest longitudinal compression strain in the specimen, consequently the highest

equivalent plastic strain occurs there. Second observation is that in each D/t ratio plot, the higher the internal pressure the specimen has, the higher the MEP strain ($\bar{\varepsilon}^{pl}_{\max}$) will be observed when the same stroke was applied. The third observation is that the MEP strain and stroke relationships are fairly smooth except at some points the curvature sharply changed which is caused by shift in location of MEP strain ($\bar{\varepsilon}^{pl}_{\max}$). When these relationships increase smoothly, the location of MEP strain is found at exact wrinkle crest tip region, while at the change points, the MEP strain ($\bar{\varepsilon}^{pl}_{\max}$) at the wrinkle tip neighboring area jumps higher than that at the wrinkle tip, causing the location of the MEP strain ($\bar{\varepsilon}^{pl}_{\max}$) moves to tip neighboring area.

The sensitivity of models to the P/P_y ratio can be observed simply by plotting the MEP strain at contact ($\bar{\varepsilon}^{pl}_{C\max}$) as a function of the P/P_y ratio for a particular D/t ratio. Figure 6.26 to Figure 6.31 present effect of P/P_y ratio on MEP strain at contact for different D/t ratios. From these plots, it can be seen that generally the MEP strain at contact decreased as a function of internal pressure ratios (P/P_y) for a particular D/t ratio.

Figure 6.26 presents effect of P/P_y ratio on the MEP strain at contact ($\bar{\varepsilon}^{pl}_{C\max}$) for specimens of D/t = 20 and 25. In these curves, the MEP strain at contact decreased smoothly from P/P_y =0.1 to 0.7, at points P/P_y = 0.8 and 0.9, the MEP at contact ($\bar{\varepsilon}^{pl}_{C\max}$) jumped away from the previous curve because the location of the MEP strain at contact moved symmetrically to neighboring areas from the wrinkle crest. At point P/P_y =1.0, for specimen of D/t = 20, the upper crest neighboring areas have the higher MEP strain at contact. For specimen of D/t = 25, when the P/P_y =1.0, the location of the MEP strain at contact ($\bar{\varepsilon}^{pl}_{C\max}$) moved further away from the wrinkle crest, it was found at the top of the wrinkle. These also can be observed in Figure 6.7 and Figure 6.8 that there are sharply changes in curvature for the MEP strain and stroke relationships representing P/P_y = 0.8, 0.9 and 1.0.

Figure 6.27 presents effect of P/P_y ratio on the MEP strain at contact ($\bar{\varepsilon}^{pl}_{C\max}$) for specimens of D/t =30 and 35. Sharp changes is observed at point P/P_y = 0.8 and 0.9, it is because the MEP strain at contact ($\bar{\varepsilon}^{pl}_{C\max}$) jumped away from the previous curve because the location of the MEP strain at contact ($\bar{\varepsilon}^{pl}_{C\max}$) moved symmetrically to neighboring inside wall areas from the tip of the wrinkle. When P/P_y =1.0, the location of the MEP strain at contact ($\bar{\varepsilon}^{pl}_{C\max}$) moved back to inside wall of the wrinkle crest. These can be observed in Figure 9 and Figure 10 in the MEP strain and stroke relationship for P/P_y = 0.8, 0.9 and 1.0.

Figure 6.28 presents effect of P/P_y ratio on the MEP strain at contact ($\bar{\varepsilon}^{pl}_{C\max}$) for specimens of D/t =40, 45, 50 and 55. Sharp change is observed only at point P/P_y =0.9, because the location of the MEP strain at contact moves to the neighboring inside wall areas of the wrinkle crest. It can be observed in Figure 11 to Figure 14 in the MEP strain and stroke relationship for P/P_y =0.9.

Figure 6.29 presents effect of P/P_y ratio on the MEP strain at contact ($\bar{\varepsilon}^{pl}_{C\max}$) for specimens of D/t =60, 65, 70, 75 and 80. For specimens of D/t =60, the MEP strain drop down since P/P_y =0.7, because from this point, higher imperfections were used to trigger the wrinkle. For specimens of D/t=65, 70, 75, 80, and 0.9, when P/P_y = 0.8 and 0.9, the MEP strain at contact dropped down because of the same reason as specimens of D/t = 60. When P/P_y =1.0, the MEP strain at contact at the wrinkle crest neighboring areas jumped up than that at the wrinkle crest. Same observation can be obtained from Figure 15 to Figure 19.

Figure 6.30 presents effect of P/P_y ratio on the MEP strain at contact ($\bar{\varepsilon}^{pl}_{C\max}$) for specimens of D/t =85, 90, and 95. Figure 31 presents effect of P/P_y ratio on the MEP strain at contact ($\bar{\varepsilon}^{pl}_{C\max}$) for specimens of D/t =100, 105, and110. The MEP strain at contact ($\bar{\varepsilon}^{pl}_{C\max}$) is always observed at inside wall of the wrinkle crest. This can be observed in Figure 20 to Figure 25.

6.3.1.2 Effect of P/P_y ratio on dependence of type of failure

The material model used by Das *et al.* (2002) in the full scale test has the nominal rupture strain 33.0%, and the corresponding equivalent plastic strain at failure was 121.5% from coupon FEA ABAQUS/Standard model described in Chapter 5. Thus, 100% was taken as the rupture failure criterion for the conservative consideration of pipe fracture, the effect of P/P_y ratio on dependence of type of failure (accordion or rupture in pipe wall) will be observed simply by drawing a straight line in internal pressure ratio vs. equivalent plastic strain plots (Figure 26 to Figure 31), the region above the line is the rupture zone, and the region below the line is the accordion type of wrinkle formation zone for this material model. The equivalent plastic strains in those plots referred to the MEP strains at contact observed in the pipe specimens. Therefore, the element assumed to fail when only one integration point failed other than all through-the-thickness points failed, this is also because of conservative consideration for pipe operation safety.

Figure 6.26 presents the effect of P/P_y on the MEP strains at contact ($\bar{\varepsilon}^{pl}_{C\max}$) for pipe specimens with D/t ratio of 20 and 25. It is observed that the pipe specimens with D/t ratio of 20 fail in rupture under the internal pressure less than $0.66Py$, and pipe specimens with D/t ratio of 25 fail in rupture under the internal pressure below $0.55Py$. Figure 6.27 presents the effect of P/P_y on the MEP strains at contact ($\bar{\varepsilon}^{pl}_{C\max}$) for pipe specimens with D/t ratio of 30 and 35. It is observed that the pipe specimens with D/t ratio of 30 fail in rupture under the internal pressure less than $0.38Py$, and pipe specimens with D/t ratio of 35 fail in rupture under the internal pressure less than $0.23Py$. Figure 6.28 presents the effect of P/P_y on MEP strains at contact ($\bar{\varepsilon}^{pl}_{C\max}$) for pipe with D/t ratio of 40, 45, 50 and 55. It is observed that the pipe specimens with D/t ratio of 40 fail in rupture under the internal pressure less than $0.11Py$. The MEP strains for pipe specimens with D/t ratio of 45, 50 and 55 are less than 100% line, therefore pipe specimens with D/t ratio of 45, 50 and 55 will not fail in rupture but fail in accordion type of wrinkles instead. Same results are observed in Figure 6.29 to Figure 6.31. Figure 6.29 presents the effect of P/P_y on the MEP strains at contact ($\bar{\varepsilon}^{pl}_{C\max}$) for pipe specimens with D/t ratio of 60, 65, 70, 75 and 80,

Figure 6.30 presents the effect of P/P_y on the MEP strains at contact ($\bar{\varepsilon}^{pl}_{C\max}$) for pipe specimens with D/t ratio of 85, 90, 95, and Figure 6.31 presents the effect of P/P_y on the MEP strains at contact ($\bar{\varepsilon}^{pl}_{C\max}$) for pipe specimens with D/t ratio 100, 105 and 110. The pipe specimens with D/t ratio ranged from 60 to 100 do not fail in rupture under internal pressure ranged between $0.1Py$ to $1.0Py$, they fail in accordion type of wrinkles instead.

6.3.2 Effects of *D/t* Ratio

6.3.2.1 Effects of *D/t* ratio on maximum equivalent plastic strains

Only the effect of D/t ratio on MEP strains at contact ($\bar{\varepsilon}^{pl}_{C\max}$) is presented in this section. The sensitivity of the model to the D/t ratio can also be observed simply by plotting the MEP strains at contact as a function of the D/t ratio. Figure 6.32 presents the effect of D/t ratio on MEP strains at contact for internal pressure ratio ranged from 0.1 to 0.5. Figure 6.33 presents the effect of D/t ratio on MEP strains at contact for internal pressure ratio ranged from 0.6 to 1.0. Five curves in each figure represent specimens of five different internal pressure ratios.

Observation from Figure 6.32 and Figure 6.33 shows that the magnitude of the MEP strains at contact decreases with the increasing of D/t ratio for specimens with internal pressure ratio ranged from 0.1 to 0.7. This is because the MEP strains at contact were always observed at the wrinkle crest area. For specimens with internal pressure ratio of 0.8 and 0.9, the magnitude of the MEP strains at contact decreased with increasing of D/t ratio, however decreases irregularly. As described in previous section, this is because the location of the MEP strains at contact was observed at the wrinkle crest neighboring area. For specimen with internal pressure ratio of 1.0, for D/t = 65, the MEP strains at contact at wrinkle crest neighboring area jumped higher than that for D/t = 60. Therefore, magnitude of the MEP strains at contact decreased with increasing of D/t ratio except for D/t =65.

6.3.2.2 Effects of *D/t* ratio on dependence of type of failure

The effect of P/P_y ratio on dependence of type of failure (accordion or rupture in pipe wall) is observed simply by drawing a straight line in diameter to thickness ratio vs. equivalent plastic strain plots (Figure 32 and Figure 33), the region above the line is the rupture zone, and the region below the line is the accordion type of wrinkle formation zone for this material model.

Figure 6.32 presents the effect of *D/t* ratio on MEP strains at contact ($\bar{\varepsilon}^{pl}_{C\max}$) for pipe specimens with internal pressure ratio from 0.1 to 0.5. It is observed that pipe specimens with P/P_y ratio of 0.1 and 0.2 fail in rupture when their *D/t* ratio is less than 40 and 37, respectively, pipe specimens with P/P_y ratio of 0.3 and 0.4 fail in rupture when their *D/t* ratio is less than 33 and 29, respectively, and pipe specimens with P/P_y ratio of 0.5 fail in rupture when their *D/t* ratio is less than 26.

Figure 6.33 presents the effect of *D/t* ratio on MEP strain at contact ($\bar{\varepsilon}^{pl}_{C\max}$) for pipe specimens with internal pressure ratio from 0.6 to 1.0. It is observed that pipe specimens with P/P_y ratio of 0.6 fail in rupture when their *D/t* ratio is less than 23, pipe specimens with P/P_y ratio of 0.7, 0.8, 0.9 and 1.0 do not fail in rupture when their *D/t* ratio is in the range of this parametric study but fail in accordion type of wrinkle.

6.3.3 Effects of Material Property

Three material models which have the same engineering stress-strain relationship until ultimate stress points but different rupture stress point as described in section 6.1.2.3 were used in coupon numerical analysis model to obtain the equivalent plastic strain at failure ($\bar{\varepsilon}^{pl}_{f}$) (or rupture equivalent plastic strain). The results of rupture equivalent plastic strain for these material models are shown in Table 6.8 and Figure 6.34. It is

observed that there is a linear increase in rupture equivalent plastic strain with increasing of rupture nominal strain (or rupture engineering strain) (Figure 6.34). For material has nominal rupture strain between 25% and 40%, the corresponding equivalent plastic strain at failure ($\bar{\varepsilon}_f^{pl}$) could be interpolated approximately linearly in this relationship.

Because three different material models were generated by linearly interpolating or extrapolating the rupture points in engineering stress-strain relationship and true stress-strain relationship, the MEP strains at contact obtained from these material models should be same as those obtained from the control material model. The results presented in Table 6.9 indicate clearly that the MEP strains at contact in the pipe numerical analysis are independent on these material models. Therefore, the data obtained from the control material model could be also used to analysis the dependence of the pipe failure mode for these materials. However, each material model has a different rupture failure criterion based on its coupon numerical analysis.

The effect of material models on dependence of type of failure (accordion or rupture) is described from two points of view for each material model, which are same as those discussed for the control material mode: the first one is the equivalent plastic strain vs. internal pressure ratio relationship and the other is the equivalent plastic strain vs. diameter to thickness ratio relationship (Figure 26 to Figure 31). The equivalent plastic strain in these Figures is MEP strain at contact Details of influence of each material model on failure mode are discussed in following sections.

6.3.3.1 Effect of material model 1 on dependence of type of failure

For the material model one which has nominal rupture strain of 25%, the corresponding rupture equivalent plastic strain is 68.65% obtained from coupon FEA model. 55% was taken as the rupture failure criterion as conservative consideration of safety. It can be observed clearly from Figure 6.26 to Figure 6.33, where the region above 55% equivalent

plastic strain line is the rupture zone for material model one, that the effect of material model one on dependence of type of failure.

Figure 6.26 presents the relationship between internal pressure and the MEP strain at contact for pipe with *D/t* ratio of 20 and 25. It is observed that two the curves are all above the 55% line, therefore the pipe specimens with *D/t* ratio 20 and 25 fail in rupture under internal pressure ranged from 0.1 to 1.0 *Py* before they self contacted at inside wall.

Figure 6.27 presents the relationship between internal pressure and MEP strain at contact for pipe specimens with *D/t* ratio of 30 and 35. It is observed that pipe with *D/t* ratio between 30 and 35 fail in rupture except for internal pressure close to 1.0*Py*.

Figure 6.28 presents the relationship between internal pressure and the MEP strain at contact for pipe with *D/t* ratio of 40, 45, 50 and 55. It is observed that pipe specimens with *D/t* ratio of 40 fail in rupture under internal pressure as high as 0.95*Py*, pipe specimens with *D/t* ratio of 45 fail in rupture under internal pressure as high as 0.91*Py*, pipe specimens with *D/t* ratio of 50 fail in rupture under internal pressure as high as 0.82*Py*, and pipe specimens with *D/t* ratio of 55 fail in rupture under internal pressure less than 0.78*Py*.

Figure 6.29 presents the relationship between internal pressure and the MEP strain at contact for pipe specimens with *D/t* ratio of 60, 65, 70, 75, and 80. It is observed that pipe specimens with *D/t* ratio between 60 and 65 fail in rupture under internal pressure less than 0.75*Py* and 0.72*Py*, respectively, pipe specimens with *D/t* ratio of 70 fail in rupture under internal pressure less than or equal to 0.65*Py*, pipe specimens with *D/t* ratio of 75 fail in rupture under internal pressure less than or equal to 0.56*Py*, and pipe specimens with *D/t* ratio of 80 fail in rupture under internal pressure less than or equal to 0.5*Py*.

Figure 6.30 presents the relationship between internal pressure ratio and the MEP strain at contact for pipe specimens with *D/t* ratio of 85, 90, and 95. It is observed that pipe specimens with *D/t* ratio of 85 fail in rupture for internal pressure equal to or less than

0.35y, pipe specimens with D/t ratio of 90 fail in rupture for internal pressure less than or equal to 0.25Py, and pipe specimens with D/t ratio of 95 do not fail in rupture for internal pressure between 0.1Py to 0.1Py.

Figure 6.31 presents the relationship between internal pressure and the MEP strain at contact for pipe specimens with D/t ratio of 100, 105 and 110. It is observed the values MEP strain at contact of three curves are all below 55%, pipe specimens with D/t ratio higher than 100 do not fail rupture under internal pressure ranged between 0.1Py to 0.1Py, but fail in accordion type of wrinkle instead.

Figure 6.32 presents the effect of D/t ratio on MEP strains at contact ($\bar{\varepsilon}^{pl}_{C\max}$) for pipe specimens with internal pressure ratio from 0.1 to 0.5. It is observed that pipe specimens with P/P_y ratio of 0.1 and 0.2 fail in rupture when their D/t ratio is less than 95 and 93, respectively, pipe specimens with P/P_y ratio of 0.3 and 0.4 fail in rupture when their D/t ratio is less than 88 and 85, respectively, and pipe specimens with P/P_y ratio of 0.5 fail in rupture when their D/t ratio is less than 80.

Figure 6.33 presents the effect of D/t ratio on MEP strain at contact ($\bar{\varepsilon}^{pl}_{C\max}$) for pipe specimens with internal pressure ratio from 0.6 to 1.0. It is observed that pipe specimens with P/P_y ratio of 0.6 and 0.7 fail in rupture when their D/t ratio is less than 73 and 67, respectively, pipe specimens with P/P_y ratio of 0.8 and 0.9 fail in rupture when their D/t ratio is less than 52 and 46, respectively, and pipe specimens with P/P_y ratio of 1.0 fail in rupture when their D/t ratio is less than 28.

6.3.3.2 Effect of material model 2 on dependence of type of failure

For the material model two which has nominal rupture strain of 30%, the corresponding rupture equivalent plastic strain is 103.1% from coupon FEA model. 80% was taken as the rupture failure criteria for conservative consideration of safety. It can be observed clearly from Figure 6.26 to Figure 6.33, where the region above 80% equivalent plastic

strain line is the rupture zone for material model one, that the effect of material model one on dependence of type of failure.

Figure 6.26 presents the relationship between internal pressure and the MEP strain at contact for pipe specimens with *D/t* ratio of 20 and 25. It is observed that the pipe specimens with *D/t* ratio of 20 fail in rupture under the internal pressure less than 0.89*Py*, and pipe specimens with *D/t* ratio of 25 fail in rupture under the internal pressure less than 0.80*Py*.

Figure 6.27 presents the relationship between internal pressure and the MEP strain at contact for pipe specimens with *D/t* ratio of 30 and 35. It is observed that the pipe specimens with *D/t* ratio of 30 fail in rupture under the internal pressure less than 0.68*Py*, and pipe specimens with *D/t* ratio of 35 fail in rupture under the internal pressure less than 0.6*Py*.

Figure 6.28 presents the relationship between internal pressure and the MEP strain at contact for pipe specimens with *D/t* ratio of 40, 45, 50 and 55. It is observed that the pipe specimens with *D/t* ratio of 40 fail in rupture under the internal pressure less than 0.52*Py*, pipe specimens with *D/t* ratio of 45 fail in rupture under the internal pressure less than 0.45*Py*, pipe specimens with *D/t* ratio of 50 fail in rupture under the internal pressure less than 0.32*Py*, and pipe specimens with *D/t* ratio of 55 fail in rupture under the internal pressure less than 0.21*Py*.

Figure 6.29, Figure 6.30 and Figure 6.31 present the relationship between internal pressure and the MEP strain at contact for pipe specimens with *D/t* ratio of 60, 65, 70, 75, 80, 85, 90, 95, 100, 105 and 110. It is observed that the values of MEP strain at contact of all these curves are higher than the rupture criterion 80%, hence pipe specimens with *D/t* ratio between 60 and 110 do not fail in rupture under internal pressure ranged between 0.1*Py* to 1.0*Py*, but fail in accordion type of wrinkle instead.

Figure 6.32 presents the effect of *D/t* ratio on MEP strains at contact ($\bar{\varepsilon}^{pl}_{C\max}$) for pipe specimens with internal pressure ratio from 0.1 to 0.5. It is observed that pipe specimens with P/P_y ratio of 0.1 and 0.2 fail in rupture when their *D/t* ratio is less than 59 and 56, respectively, pipe specimens with P/P_y ratio of 0.3 and 0.4 fail in rupture when their *D/t* ratio is less than 51 and 48, respectively, and pipe specimens with P/P_y ratio of 0.5 fail in rupture when their *D/t* ratio is less than 43.

Figure 6.33 presents the effect of *D/t* ratio on MEP strain at contact ($\bar{\varepsilon}^{pl}_{C\max}$) for pipe specimens with internal pressure ratio from 0.6 to 1.0. It is observed that pipe specimens with P/P_y ratio of 0.6 and 0.7 fail in rupture when their *D/t* ratio is less than 35 and 29, respectively, pipe specimens with P/P_y ratio of 0.8 fail in rupture when their *D/t* ratio is less than 20, and pipe specimens with P/P_y ratio of 0.9 and 1.0 do no fail in rupture when their *D/t* ratios in the ranges of this parametric study.

6.3.3.3 Effect of material model 3 on dependence of type of failure

For the material model three which has nominal rupture strain of 40%, the corresponding rupture equivalent plastic strain is 170.2% from coupon FEA model. 135% was taken as the rupture failure criteria for conservative consideration of safety. It can be observed very clearly from Figure 6.26 to Figure 6.33, where the region above 120% equivalent plastic strain line is the rupture zone for material model three, that the effect of material model one on dependence of type of failure.

Figure 6.26 presents the relationship between internal pressure and the MEP strain at contact for pipes specimens with *D/t* ratio of 20 and 25. It is observed that the pipe specimens with *D/t* ratio of 20 fail in rupture under the internal pressure less than $0.21Py$, and pipe specimens with *D/t* ratio of 25 do not fail in rupture under the internal pressure between $0.1Py$ to $1.0Py$. Figure 6.27 to Figure 6.31 present the relationship between internal pressure and the MEP strain at contact for pipes specimens with *D/t* ratio ranged from 30 to 110. It is observed there is no intersection between the 135% rupture criterion

line and these curves, since values of the MEP strain at contact of these pipe specimens are all below the rupture criterion of material model three. Therefore, only accordion type of failure will occur in these pipes.

Figure 6.32 and Figure 6.33 present the effect of *D/t* ratio on MEP strains at contact ($\bar{\varepsilon}^{pl}_{C\max}$) for pipe specimens with internal pressure ratio from 0.1 to1.0. It is observed that pipe specimens with P/P_y ratio of 0.1 and 0.2 fail in rupture when their *D/t* ratio is less than 23 and 21, respectively, and pipe specimens with P/P_y ratio of 0.3 to 1.0 do not fail in rupture when their *D/t* ratio is under the range used in this parametric study, however, fail in accordion type of wrinkles.

6.3.4 Influence on Pipeline Maintenance

Pipes with various *D/t* ratios may not fracture under axi-symmetric loading and deformation on some circumstances, instead, accordion type of failure will occurred in the pipe wall. This may cause other problems such as maintenance problems. As described in Chapter 2, pipeline companies will regularly send maintenance tools such as cleaning pigs and smart pigs to cleaning and inspect inside of pipe. Usually the fitting diameters of these pigs are 5% to 10% less than the pipe inside diameters. If the pipe does not rupture under axi-symmetric loading, it may buckle further once the wrinkle formed and develop accordion type of wrinkle if possible. Once the first wrinkle contacts inside the pipe wall, the second wrinkle may form close to the first one. The pipe wall between two wrinkle crests may fold inside under further loading causing significant decrease of inside pipe diameter as shown in Figure 6.35. In some situation, the internal pipe diameters may decrease more than 5%-10% which is less than the minimum fitting diameters of cleaning or inspecting pigs. If this happens, the pigs can not go through but stick somewhere inside of the pipelines and may cause critical technical and financial problems for the pipeline company.

6.4 SUMMARY

After 190 specimens with diameter to thickness (D/t) ratios ranging from 20 to 110 and internal pressure (P/P_y) ratios ranging between 0.1 and 1.0 and three material models were run with numerical analysis models, it s found that:

(a) The pipe specimens exhibited outward bulge type wrinkle even for the lower internal pressure ratio of 0.1. However, effect of zero internal pressure was not included in this study.

(b) The maximum equivalent plastic strain at contact decreases as internal pressure increases if D/t ratio is kept unchanged.

(c) The maximum equivalent plastic strain at contact also decreases as D/t ratio increases if the lever of internal pressure is not changed.

(d) The material for pipe specimens used in the experimental study is highly ductile. The line pipe made of this material does not fail in rupture for D/t ratios higher than 40 when subjected to monotonically increasing axi-symmetric compressive axial deformation. Rather, an accordion type failure with one or multiple winkles is expected to occur.

(e) The same line pipe does not fail in rupture for internal pressure ratio higher than 0.70. Rather, an accordion type failure with one or multiple winkles is expected to occur.

(f) The pipe specimens made of the same material and with D/t ratio between 20 and 40, the failure mode depends on the internal pressure.

(g) The pipe specimens made of the same material with internal pressure ratio between 0.1 and 0.70, the failure mode depends on the D/t ratio.

(h) The ductility of material has significant influence on modes of failure. Higher the rupture engineering strain (higher the ductility of the material), higher equivalent plastic strain at rupture is expected. As the ductility of pipe material increases, chance of rupture failure mode decreases, and thus the chance accordion type failure mode increases.

(i) The both failure modes (accordion or rupture) should be avoided. The accordion type failure poses maintenance problems for the operating pipeline since the

cleaning and inspecting instrument may not be able to pass through. The rupture failure is even more serious problems since a rupture in the field line pipe wall causes integrity and safety of pipe line structure and also creates environmental disaster.

Table 6.1 Assumed Rupture Points in Engineering Stress-Strain Diagrams of Material Models for Parametric Study

Material Model ID	Nominal Rupture Strain (%)	Nominal Rupture Stress (MPa)
Material Model 1	25	367.48
Material Model 2	30	333.87
Material Model 3	40	266.66

Table 6.2 Assumed Rupture Points in True Stress-Strain Diagrams of Material Models for Parametric Study

Material Model ID	True Rupture Strain (%)	True Rupture Stress (MPa)
Material Model 1	93.74	942.99
Material Model 2	113.90	1048.45
Material Model 3	145.08	1143.78

Table 6.3 Summary of Internal Pressure and Pipe Wall thickness for Specimens Used in Parametric Study

D/t	t	Py	0.1Py	0.2Py	0.3Py	0.4Py	0.5Py	0.6Py	0.7Py	0.8Py	0.9Py	1.0Py
	(mm)	(MPa)	(MPa)	(MPa)	(MPa)	(MPa)	(MPa)	(MPa)	(MPa)	(MPa)	(MPa)	(MPa)
20	16.283	38.632	3.863	7.726	11.589	15.453	19.316	23.179	27.042	30.905	34.768	38.632
25	13.026	30.583	3.058	6.117	9.175	12.233	15.292	18.350	21.408	24.467	27.525	30.583
30	10.855	25.310	2.531	5.062	7.593	10.124	12.655	15.186	17.717	20.248	22.779	25.310
35	9.305	21.588	2.159	4.318	6.476	8.635	10.794	12.953	15.112	17.271	19.429	21.588
40	8.142	18.821	1.882	3.764	5.646	7.528	9.410	11.292	13.174	15.056	16.938	18.821
45	7.237	16.682	1.668	3.336	5.005	6.673	8.341	10.009	11.677	13.345	15.014	16.682
50	6.513	14.980	1.498	2.996	4.494	5.992	7.490	8.988	10.486	11.984	13.482	14.980
55	5.921	13.593	1.359	2.719	4.078	5.437	6.796	8.156	9.515	10.874	12.233	13.593
60	5.428	12.441	1.244	2.488	3.732	4.976	6.220	7.464	8.708	9.953	11.197	12.441
65	5.010	11.469	1.147	2.294	3.441	4.588	5.734	6.881	8.028	9.175	10.322	11.469
70	4.652	10.638	1.064	2.128	3.191	4.255	5.319	6.383	7.446	8.510	9.574	10.638
75	4.342	9.919	0.992	1.984	2.976	3.968	4.959	5.951	6.943	7.935	8.927	9.919
80	4.071	9.291	0.929	1.858	2.787	3.716	4.646	5.575	6.504	7.433	8.362	9.291
85	3.831	8.738	0.874	1.748	2.621	3.495	4.369	5.243	6.117	6.990	7.864	8.738
90	3.618	8.247	0.825	1.649	2.474	3.299	4.124	4.948	5.773	6.598	7.422	8.247
95	3.428	7.809	0.781	1.562	2.343	3.123	3.904	4.685	5.466	6.247	7.028	7.809
100	3.257	7.414	0.741	1.483	2.224	2.966	3.707	4.448	5.190	5.931	6.673	7.414
105	3.102	7.058	0.706	1.412	2.117	2.823	3.529	4.235	4.940	5.646	6.352	7.058
110	2.961	6.734	0.673	1.347	2.020	2.694	3.367	4.040	4.714	5.387	6.061	6.734

Table 6.4 Results of Comparison of Location Effect on Stroke at Contact

Specimen ID	D/t	P/P_y	Stroke at Contact (mm)	
			Wrinkle near Bottom Collar	Wrinkle at Middle
Dt20P10	20	0.1	167.2	175.2
Dt20P20	20	0.2	179.5	179.2
Dt20P30	20	0.3	196.9	184.0
Dt20P40	20	0.4	213.2	190.6
Dt20P50	20	0.5	220.8	199.06
Dt20P60	20	0.6	231.7	210.0
Dt20P70	20	0.7	243.5	222.0
Dt20P80	20	0.8	256.3	237.4
Dt20P90	20	0.9	269.7	254.2
Dt20P100	20	1.9	287.9	270.7
Dt55P10	55	0.1	88.03	85.37
Dt55P20	55	0.2	91.7	88.03
Dt55P30	55	0.3	95.2	90.00
Dt55P40	55	0.4	97.96	94.92
Dt55P50	55	0.5	103.0	100.8
Dt55P60	55	0.6	107.77	106.08
Dt55P70	55	0.7	114.64	111.4
Dt55P80	55	0.8	122.64	122.07
Dt55P90	55	0.9	136.74	132.91
Dt55P100	55	1.9	164.22	161.7
Dt95P10	95	0.1	61.77	61.95
Dt95P20	95	0.2	63.15	63.65
Dt95P30	95	0.3	66.23	66.35
Dt95P40	95	0.4	70.05	68.15
Dt95P50	95	0.5	72.49	74.00
Dt95P60	95	0.6	78.47	78.37
Dt95P70	95	0.7	83.04	80.77
Dt95P80	95	0.8	91.51	85.57
Dt95P90	95	0.9	100.4	93.6
Dt95P100	95	1.9	105.2	102.8

Table 6.5 Results of Comparison of Location Effect on Maximum Equivalent Plastic Strain at Contact

Specimen ID	D/t	P/P_y	Maximum Equivalent Plastic Strain at Contact (%)	
			Wrinkle near Bottom Collar	Wrinkle at Middle
Dt20P10	20	0.1	133.77	143.8
Dt20P20	20	0.2	128.92	136.8
Dt20P30	20	0.3	114.8	129.1
Dt20P40	20	0.4	110.43	121.9
Dt20P50	20	0.5	102.27	114.2
Dt20P60	20	0.6	94.11	105.5
Dt20P70	20	0.7	85.08	95.9
Dt20P80	20	0.8	76.87	88.52
Dt20P90	20	0.9	69.35	79.32
Dt20P100	20	1.9	65.15	68.12
Dt55P10	55	0.1	85.79	83.19
Dt55P20	55	0.2	87.95	80.64
Dt55P30	55	0.3	85	76.06
Dt55P40	55	0.4	80.06	73.28
Dt55P50	55	0.5	76.1	69.91
Dt55P60	55	0.6	70.94	66.29
Dt55P70	55	0.7	66.34	60.71
Dt55P80	55	0.8	63.06	53.64
Dt55P90	55	0.9	63.75	49.45
Dt55P100	55	1.0	69.47	44.79
Dt95P10	95	0.1	54.98	54.47
Dt95P20	95	0.2	58.1	53
Dt95P30	95	0.3	51.83	51.67
Dt95P40	95	0.4	55.18	50.36
Dt95P50	95	0.5	55.02	49.39
Dt95P60	95	0.6	53.17	47.39
Dt95P70	95	0.7	48.93	45.11
Dt95P80	95	0.8	45.46	42.03
Dt95P90	95	0.9	37.13	38.25
Dt95P100	95	1.0	36.78	35.53

Table 6.6 Results of Effect of Imperfections on Maximum Equivalent Plastic Strain at Contact

Specimen ID	D/t	P/P_y	Maximum Equivalent Plastic Strain at Contact (%)					
			2% [1]	3%	4%	6%	7%	8%
Dt90P20	90	0.2	55.9		55.08			54.08
Dt90P50	90	0.5	n/a	51.04	50.41			49.06
Dt90P80	90	0.8				n/a	43.41	43.28
Dt55P20	55	0.2		n/a	80.64	79.25		78.58
Dt55P50	55	0.5			n/a	69.91	69.49	69.1
Dt55P80	55	0.8				n/a	53.64	53.61

1. 2% is the 2% imperfection used to trigger the wrinkle formation.

Table 6.7 Result Summary for Specimens Used in Parametric Study

D/t	Maximum Equivalent Plastic Strain for Internal Pressure Ratio P/P_y (%)									
	0.1Py	0.2Py	0.3Py	0.4Py	0.5Py	0.6Py	0.7Py	0.8Py	0.9Py	1.0Py
20	143.8	136.8	129.1	121.9	114.2	105.5	95.9	88.52	79.32	68.12
25	127.08	121.85	115.9	109.8	103.35	95.7	86.92	80.64	69.01	57.49
30	114.35	109.78	104.35	99.11	93.35	86.77	79.24	72.84	66.36	53.66
35	105.07	101.66	96.91	92.27	86.45	80.39	73.47	66.41	63.23	51.28
40	100.57	96.72	91.59	86.83	81.79	75.59	68.85	61.91	59.68	49.06
45	95.13	90.56	87.18	82.51	77.33	72.1	65.27	58.64	55.71	47.31
50	89.18	84.73	81.04	77.76	73.54	68.91	62.36	55.71	52.94	45.95
55	83.19	80.64	76.06	73.28	69.91	66.29	60.71	53.64	49.45	44.79
60	78.35	75.15	72.02	69.12	65.89	63.3	58.58	51.78	47.09	43.65
65	74.62	71.41	68.51	65.91	62.67	59.67	56.39	50.51	45.55	44.07
70	70.42	68.1	65.08	62.39	59.28	56.43	53.52	49.79	44.23	42.9
75	66.24	64.24	61.95	59.73	57.06	54.06	51.56	48.6	42.85	41.68
80	62.82	61.19	58.99	56.85	54.73	52.15	49.5	47	42.17	40.04
85	59.72	58.31	56.31	54.47	52.74	50.31	47.4	45.34	41	37.71
90	57.24	55.9	54.12	52.37	51.04	49.09	46.6	43.41	38.63	36.36
95	54.47	53	51.67	50.36	49.39	47.39	45.11	42.03	38.25	35.53
100	52.41	51.22	49.63	48.22	46.87	45.41	43.56	40.71	37.6	34.56
105	50.59	48.96	47.71	46.2	45.12	43.4	42.16	39.56	37.31	33.68
110	49.16	47.49	46.05	44.99	43.61	42	40.68	38.58	36.81	33.07

Table 6.8 Results of Coupon Analysis of Material Models

Material Model ID	Engineering Rupture Strain (%)	Equivalent Plastic Strain at Rupture (%)
Material Model 1	25	68.65
Material Model 2	30	100.3
Control Model	33	1215
Material Model 3	40	170.2

Table 6.9 Results of Comparison Maximum Equivalent Plastic Strain at Contact Using Different Material Models for Specimens with D/t=20, 60 and 90

Specimen ID	D/t	P/P_y	Material Model	Maximum Equivalent Plastic Strain at Contact (%)
Dt20P20	20	0.2	Control Model	138.0
Dt20P50	20	0.5	Control Model	114.23
Dt20P80	20	0.8	Control Model	88.52
Dt20P20M1	20	0.2	Material Model 1	136.76
Dt20P50M1	20	0.5	Material Model 1	114.80
Dt20P80M1	20	0.8	Material Model 1	87.69
Dt20P20M3	20	0.2	Material Model 3	138.10
Dt20P50M3	20	0.5	Material Model 3	116.02
Dt20P80M3	20	0.8	Material Model 3	89.82
Dt60P20	60	0.2	Control Model	75.15
Dt60P50	60	0.5	Control Model	65.89
Dt60P80	60	0.8	Control Model	51.78
Dt60P20M1	60	0.2	Material Model 1	74.54
Dt60P50M1	60	0.5	Material Model 1	65.46
Dt60P80M1	60	0.8	Material Model 1	51.60
Dt60P20M3	60	0.2	Material Model 3	76.31
Dt60P50M3	60	0.5	Material Model 3	66.67
Dt60P80M3	60	0.8	Material Model 3	52.10
Dt90P20	90	0.2	Control Model	55.90
Dt90P50	90	0.5	Control Model	51.04
Dt90P80	90	0.8	Control Model	43.40
Dt90P20M1	90	0.2	Material Model 1	55.35
Dt90P50M1	90	0.5	Material Model 1	50.62
Dt90P80M1	90	0.8	Material Model 1	42.95
Dt90P20M3	90	0.2	Material Model 3	55.88
Dt90P50M3	90	0.5	Material Model 3	51.03
Dt90P80M3	90	0.8	Material Model 3	43.39

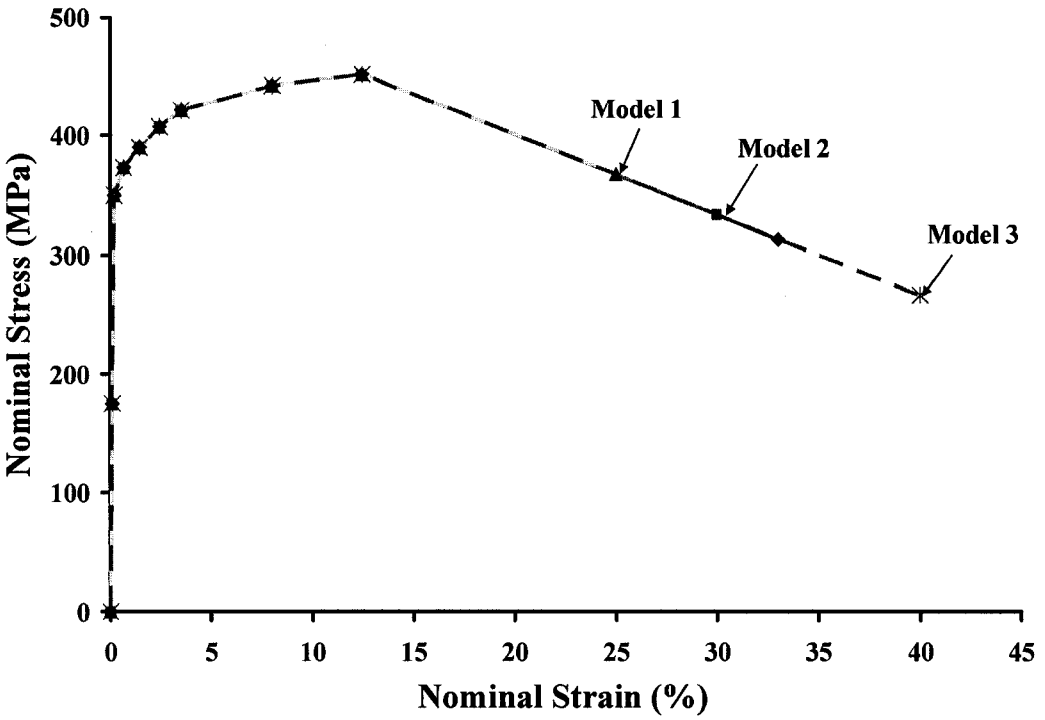

Figure 6.1 Nominal Strain vs. Nominal Stress for Material Models

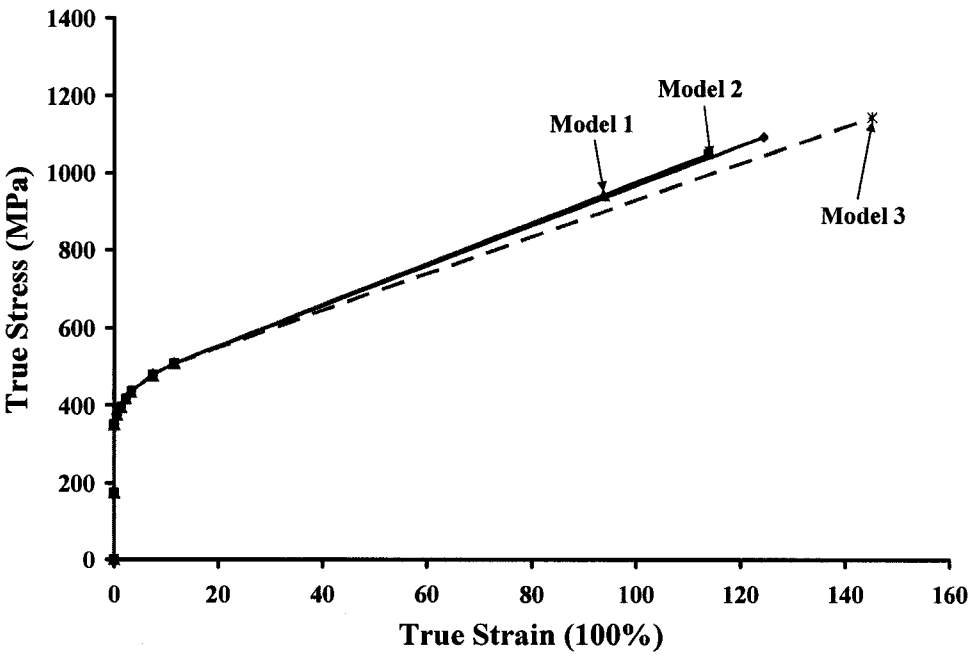

Figure 6.2 True Strain vs. True Stress for Material Models

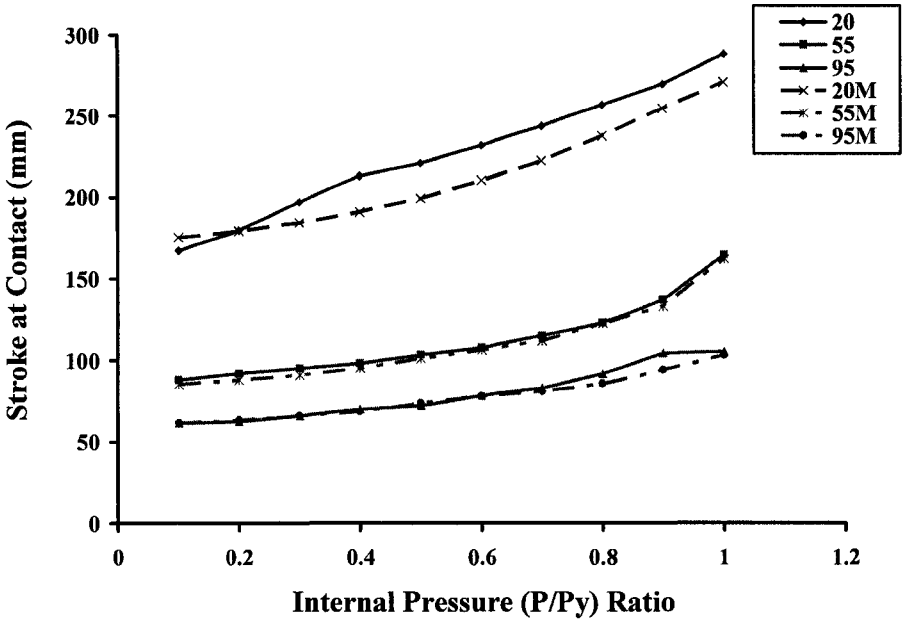

Figure 6.3 Results of Effect of Location on Stroke at Contact

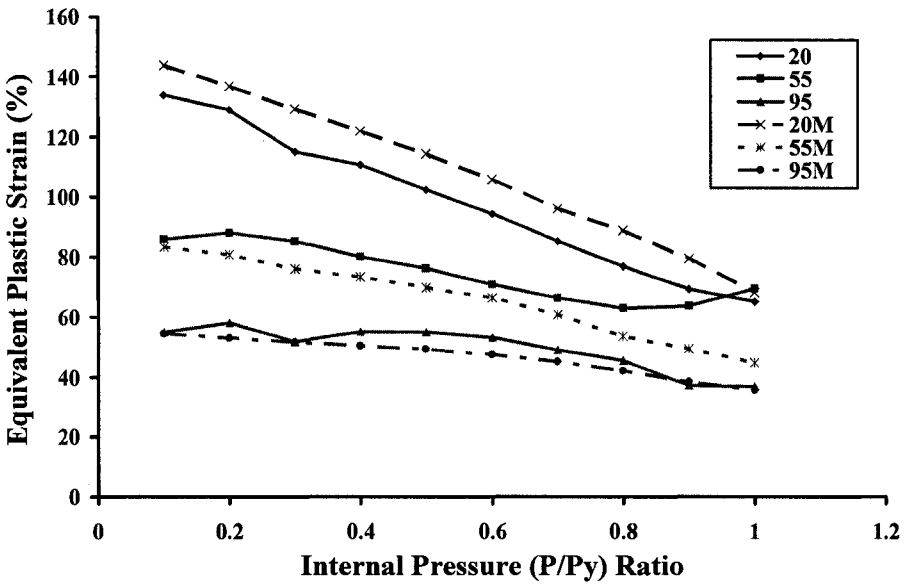

Figure 6.4 Results of Effect of Location on Maximum Equivalent Plastic Strains at Contact

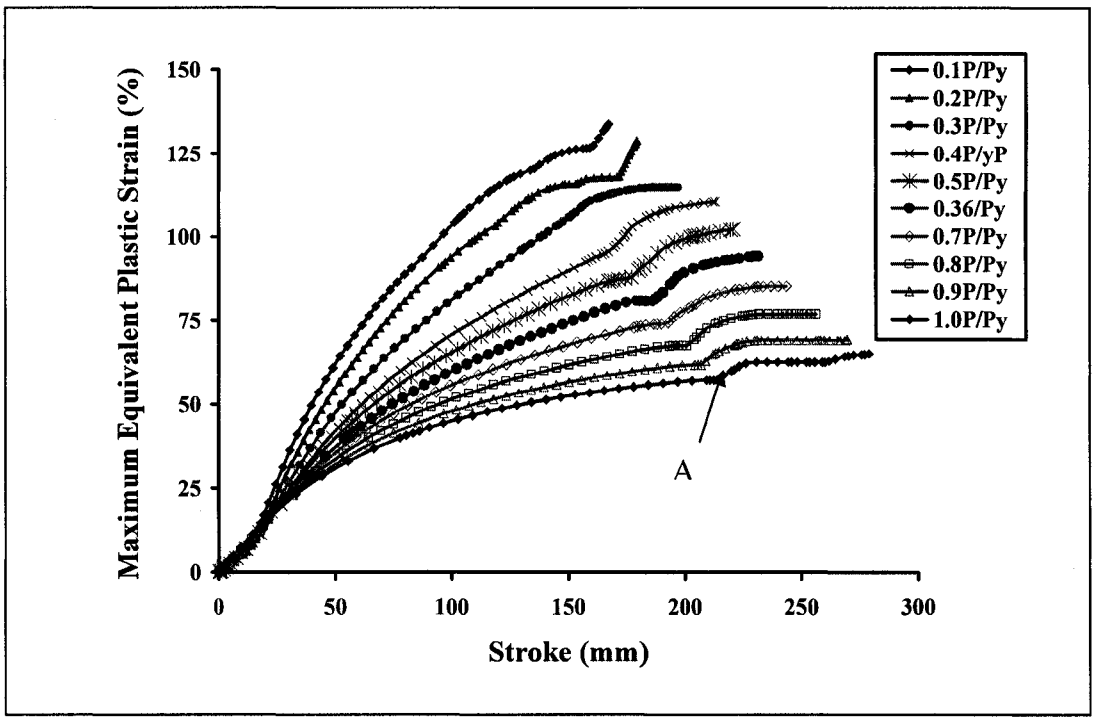

Figure 6.5 Maximum Equivalent Plastic Strain vs. Stroke for D/t=20 Specimens When Wrinkles Form near Bottom Collar

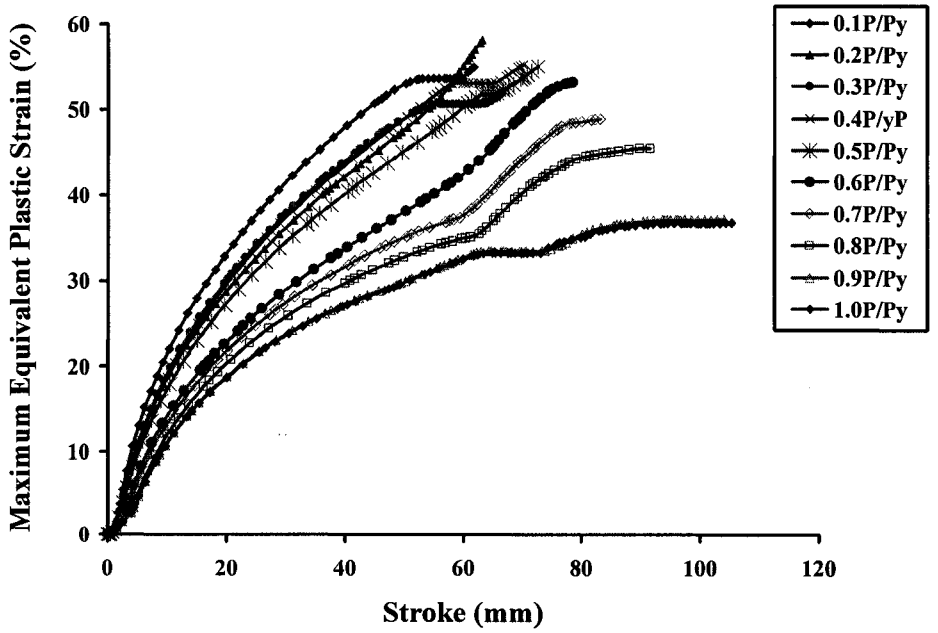

Figure 6.6 Maximum Equivalent Plastic Strain vs. Stroke for D/t=95 Specimens When Wrinkles Form near Bottom Collar

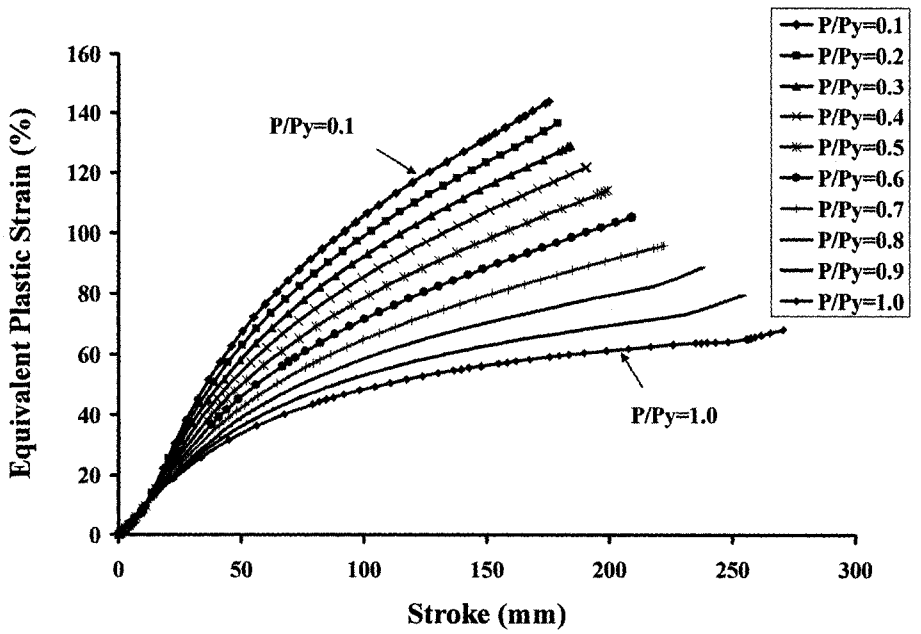

Figure 6.7 Equivalent Plastic Strain vs. Stroke for D/t=20 Specimens

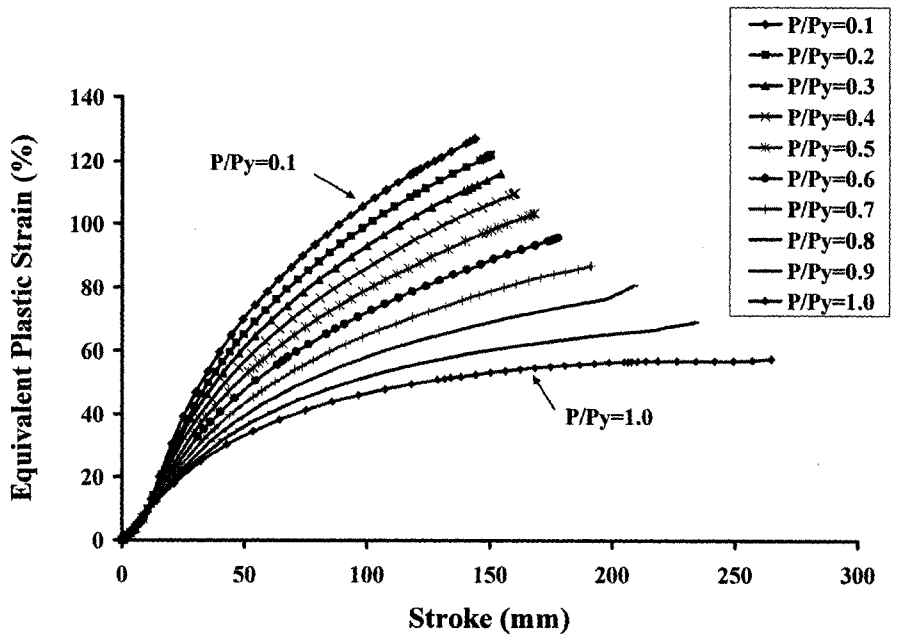

Figure 6.8 Equivalent Plastic Strain vs. Stroke for D/t=25 Specimens

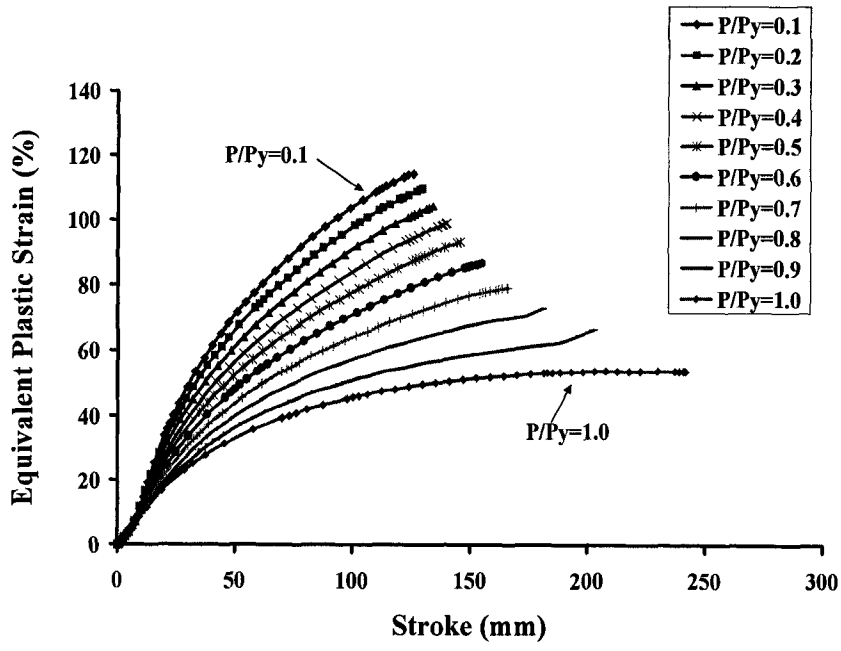

Figure 6.9 Equivalent Plastic Strain vs. Stroke for D/t=30 Specimens

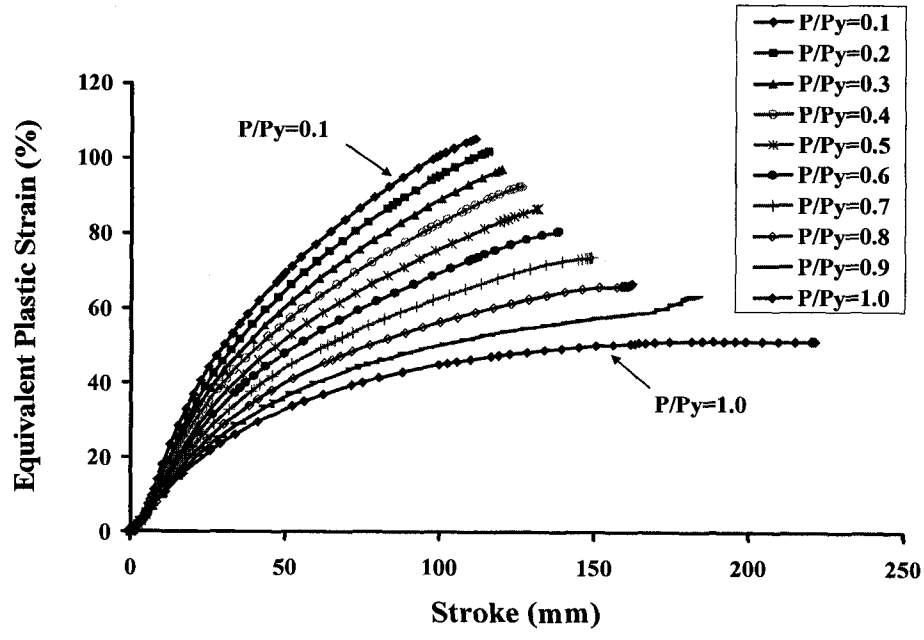

Figure 6.10 Equivalent Plastic Strain vs. Stroke for D/t=35 Specimens

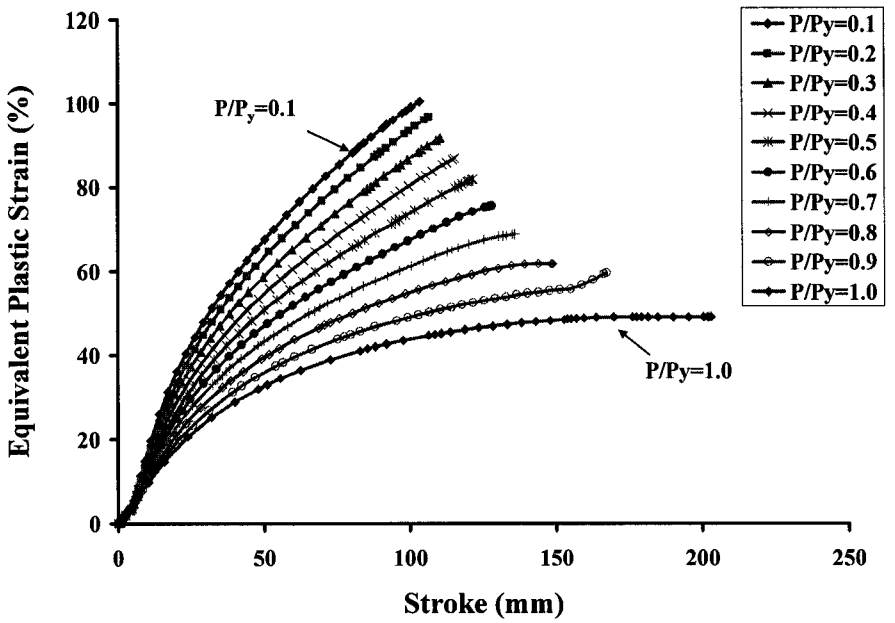

Figure 6.11 Equivalent Plastic Strain vs. Stroke for D/t=40 Specimens

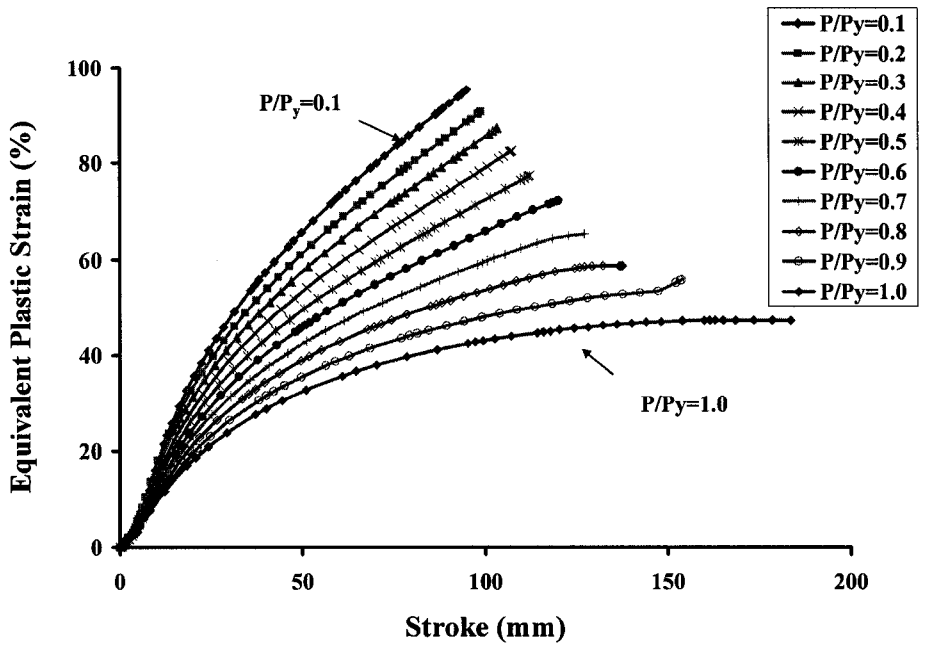

Figure 6.12 Equivalent Plastic Strain vs. Stroke for D/t=45 Specimens

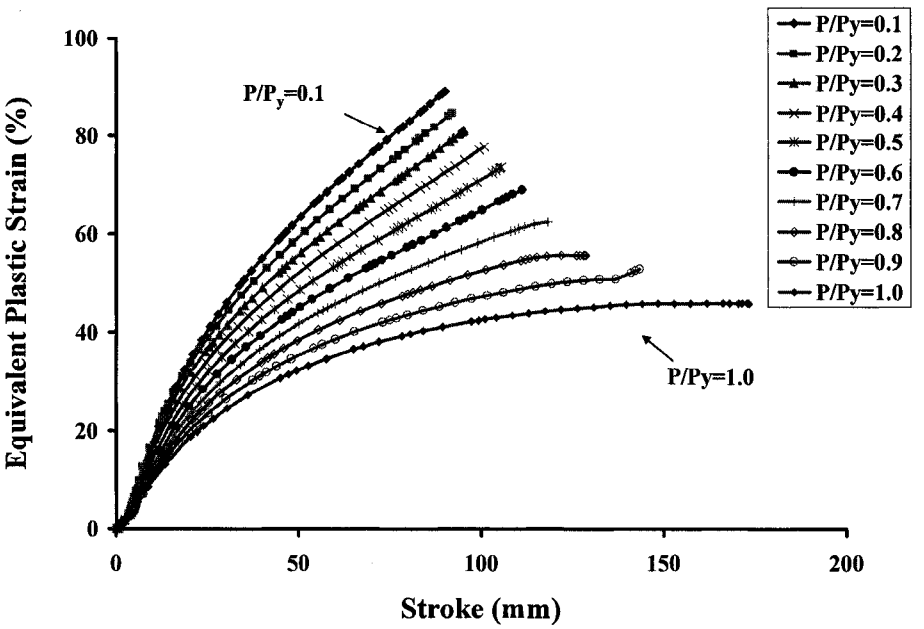

Figure 6.13 Equivalent Plastic Strain vs. Stroke for D/t=50 Specimens

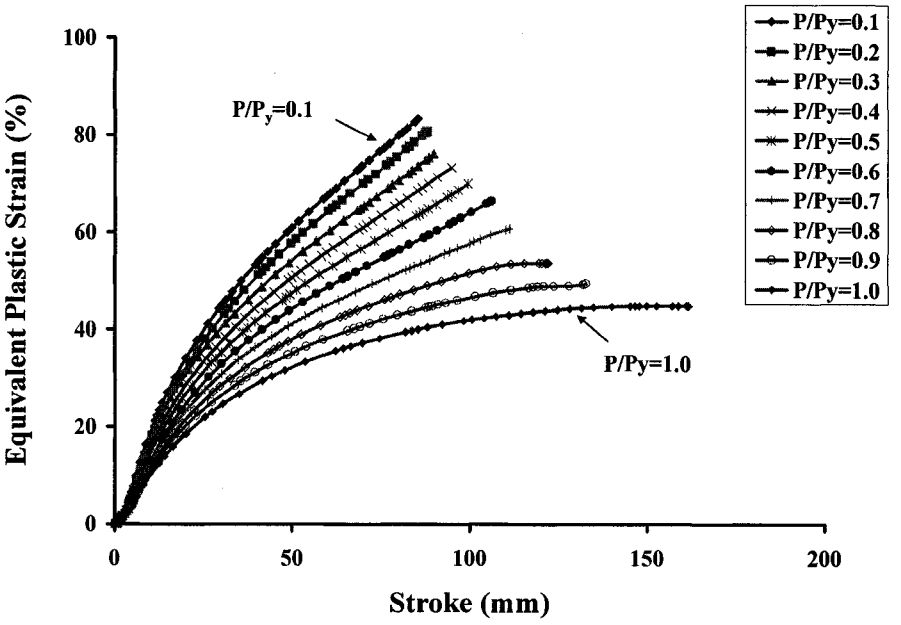

Figure 6.14 Equivalent Plastic Strain vs. Stroke for D/t=55 Specimens

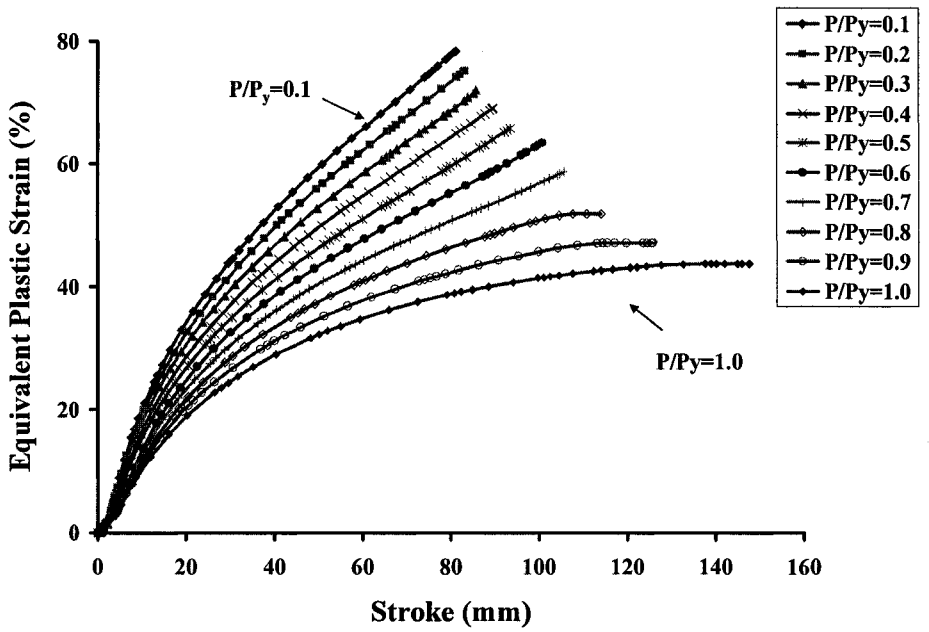

Figure 6.15 Equivalent Plastic Strain vs. Stroke for D/t=60 Specimens

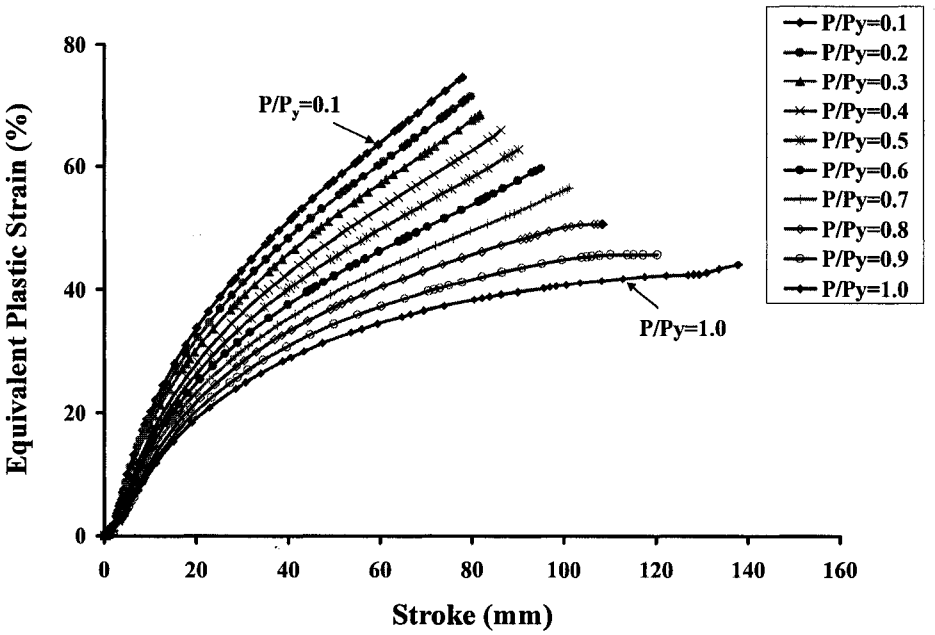

Figure 6.16 Equivalent Plastic Strain vs. Stroke for D/t=65 Specimens

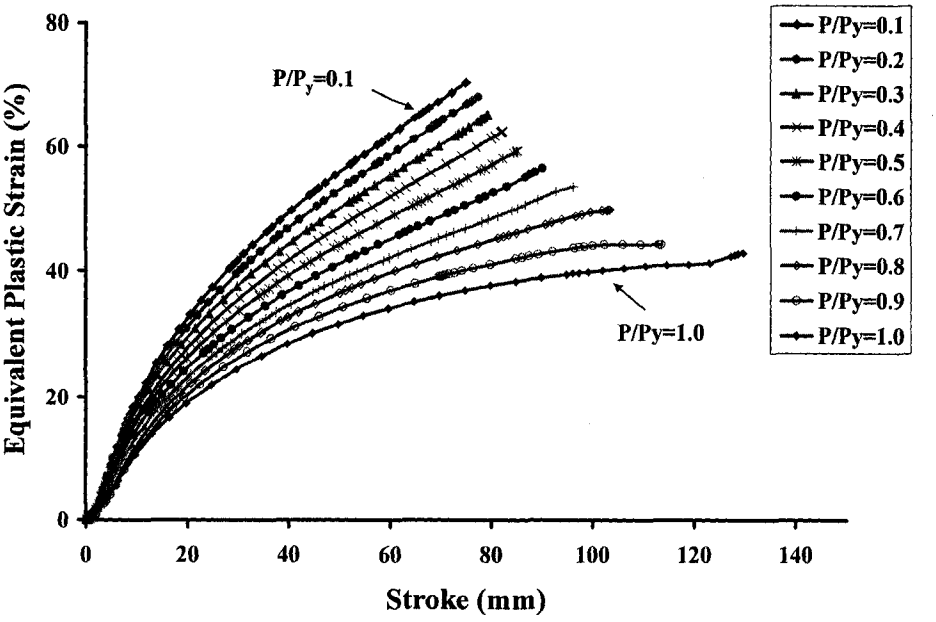

Figure 6.17 Equivalent Plastic Strain vs. Stroke for D/t=70 Specimens

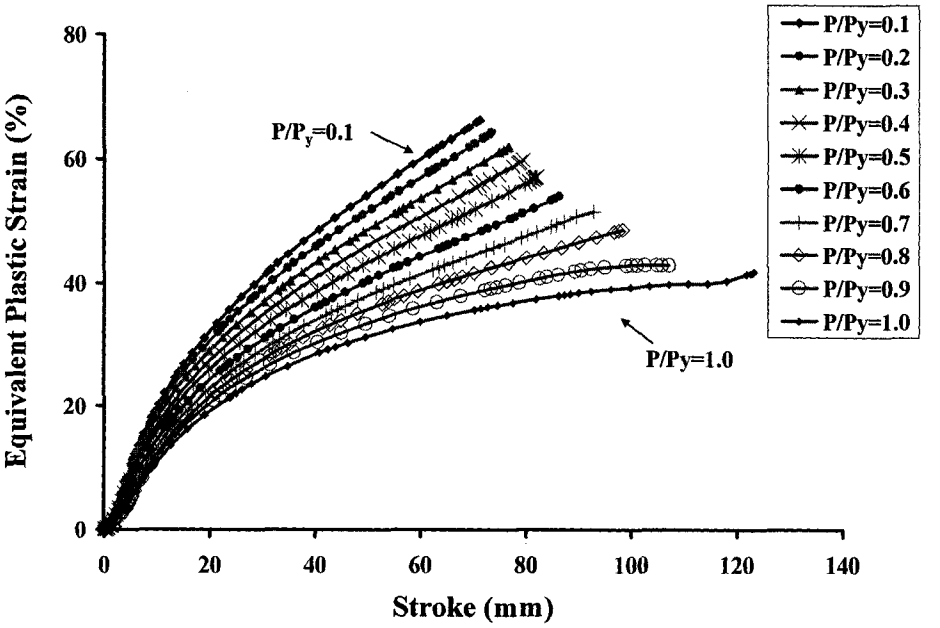

Figure 6.18 Equivalent Plastic Strain vs. Stroke for D/t=75 Specimens

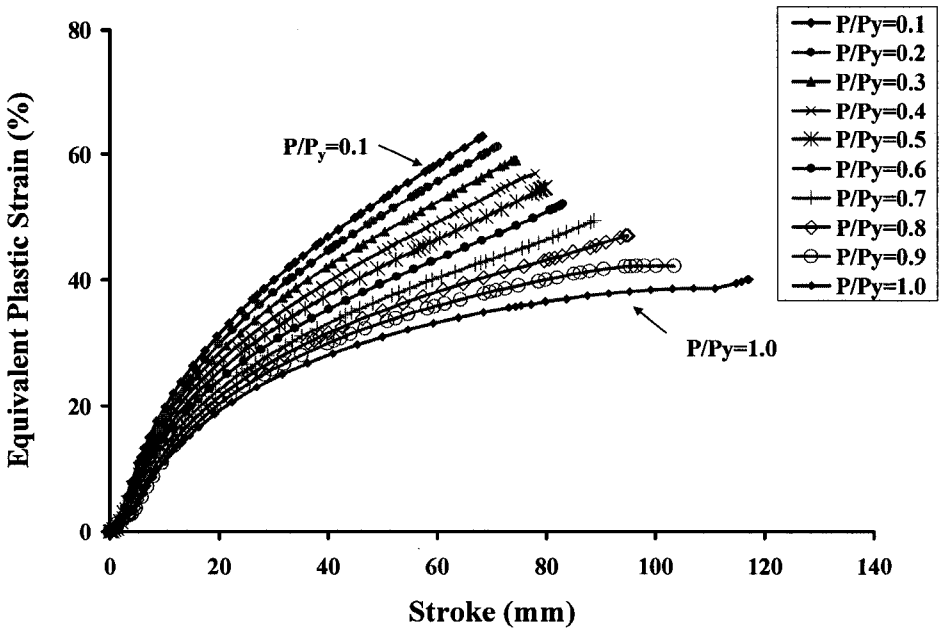

Figure 6.19 Equivalent Plastic Strain vs. Stroke for D/t=80 Specimens

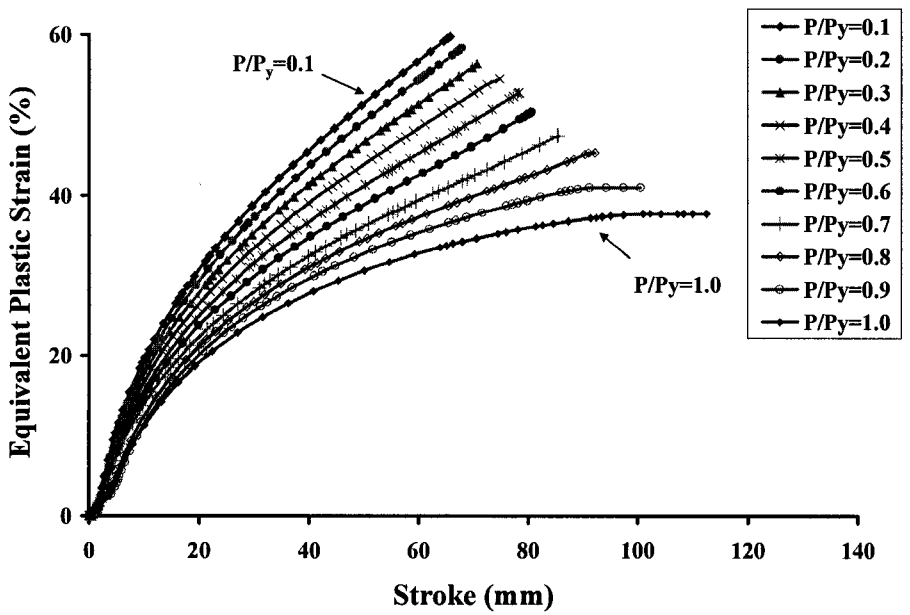

Figure 6.20 Equivalent Plastic Strain vs. Stroke for D/t=85 Specimens

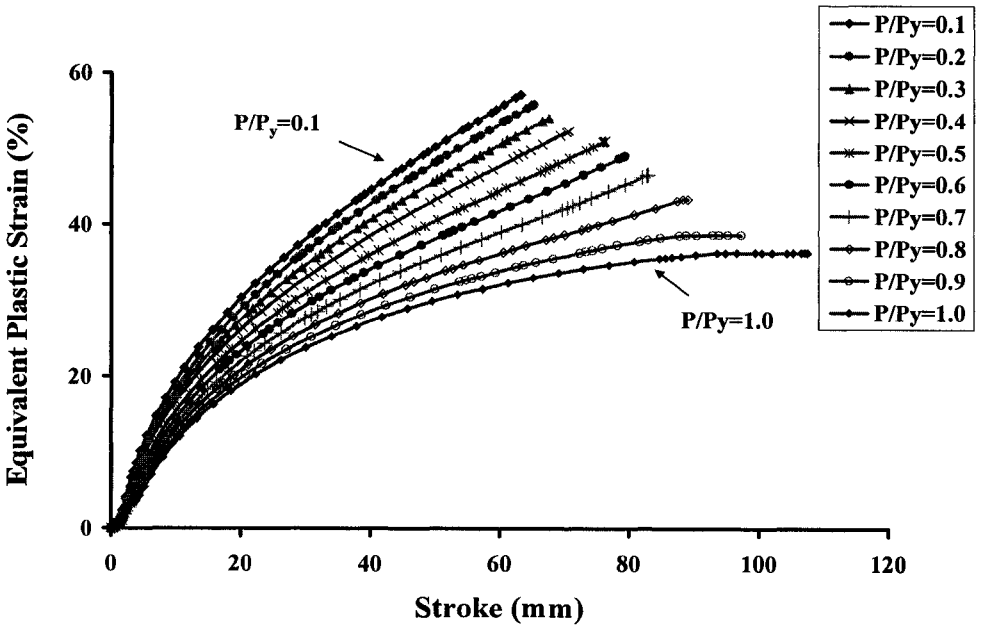

Figure 6.21 Equivalent Plastic Strain vs. Stroke for D/t=90 Specimens

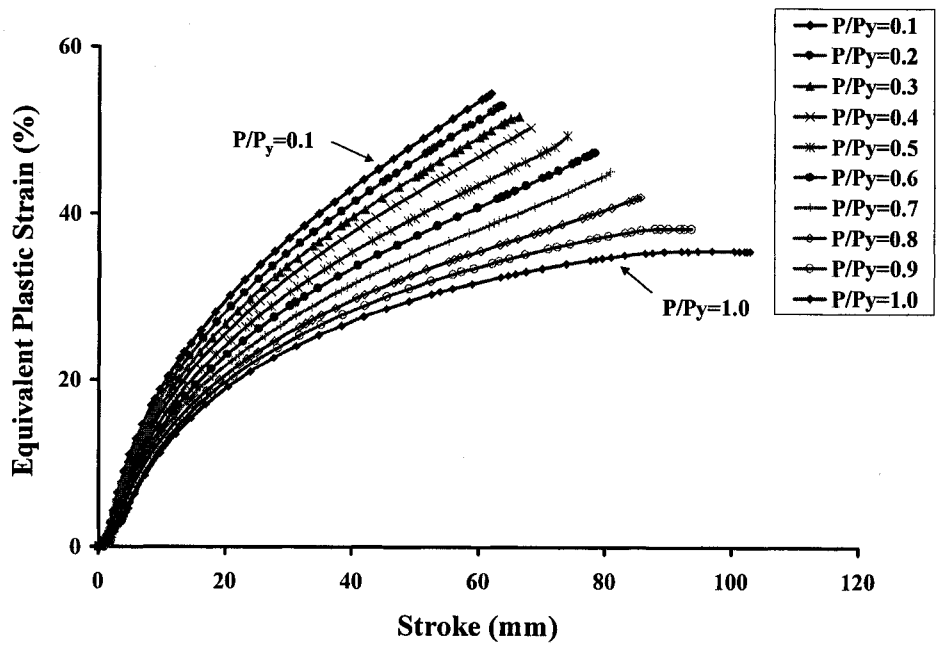

Figure 6.22 Equivalent Plastic Strain vs. Stroke for D/t=95 Specimens

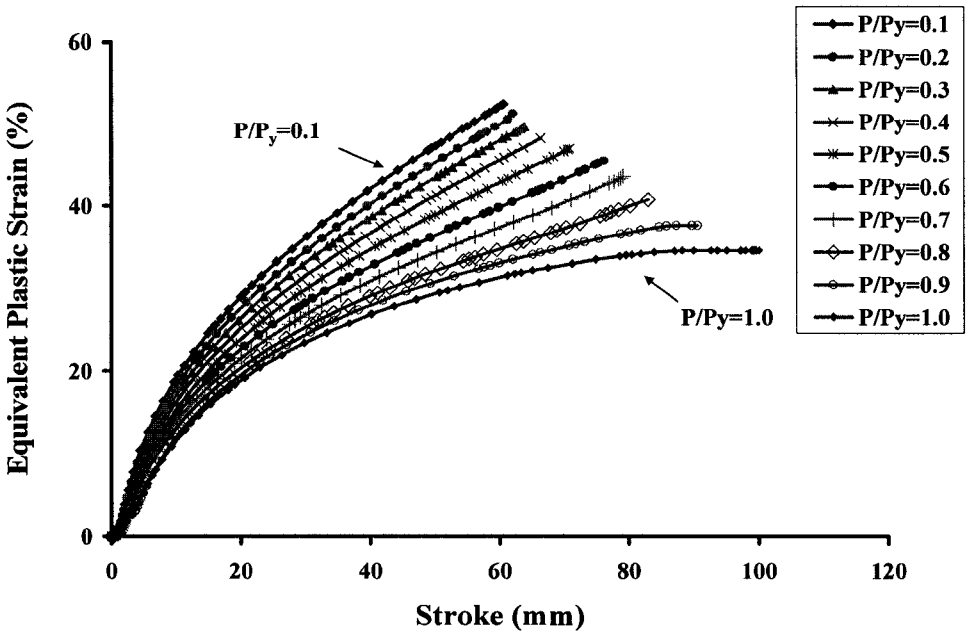

Figure 6.23 Equivalent Plastic Strain vs. Stroke for D/t=100 Specimens

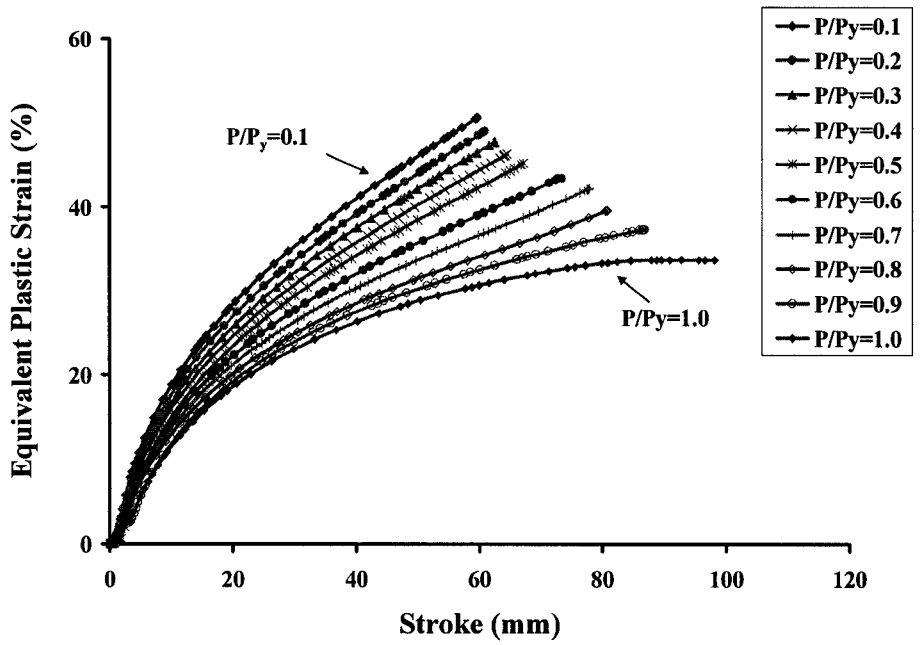

Figure 6.24 Equivalent Plastic Strain vs. Stroke for D/t=105 Specimens

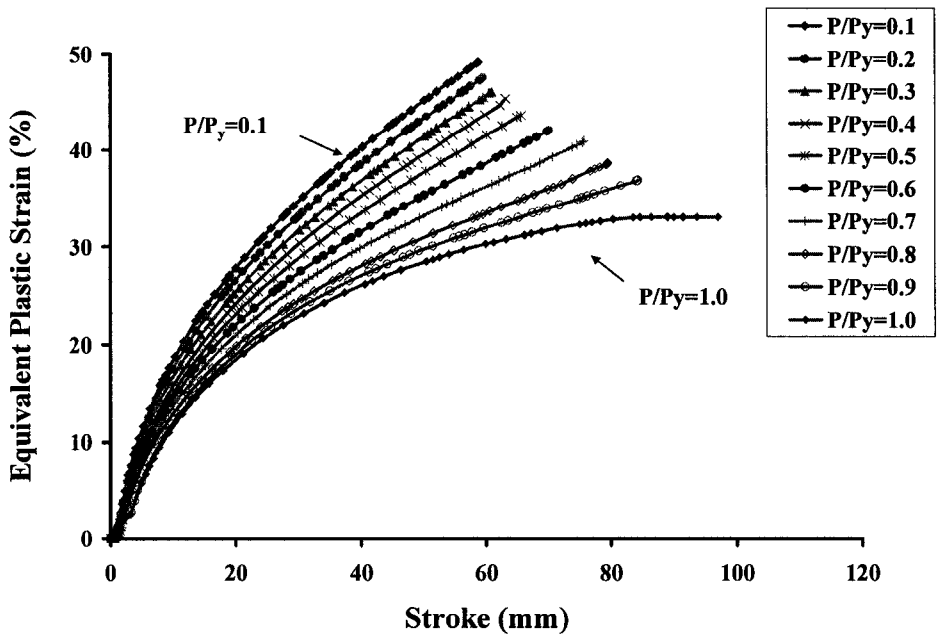

Figure 6.25 Equivalent Plastic Strain vs. Stroke for D/t=110 Specimens

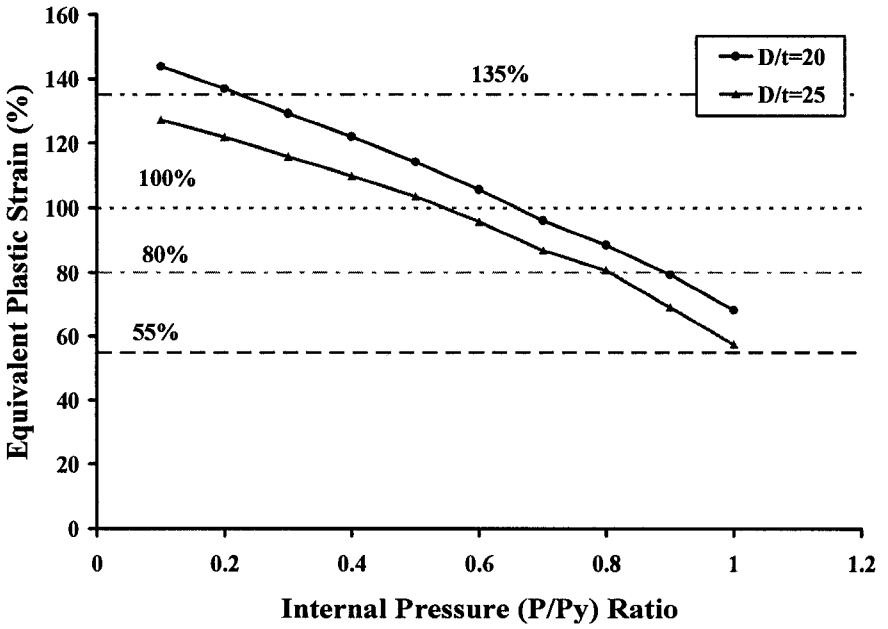

Figure 6.26 Equivalent Plastic Strain vs. Internal Pressure (P/Py) Ratio for D/t=20 and 25 Specimens

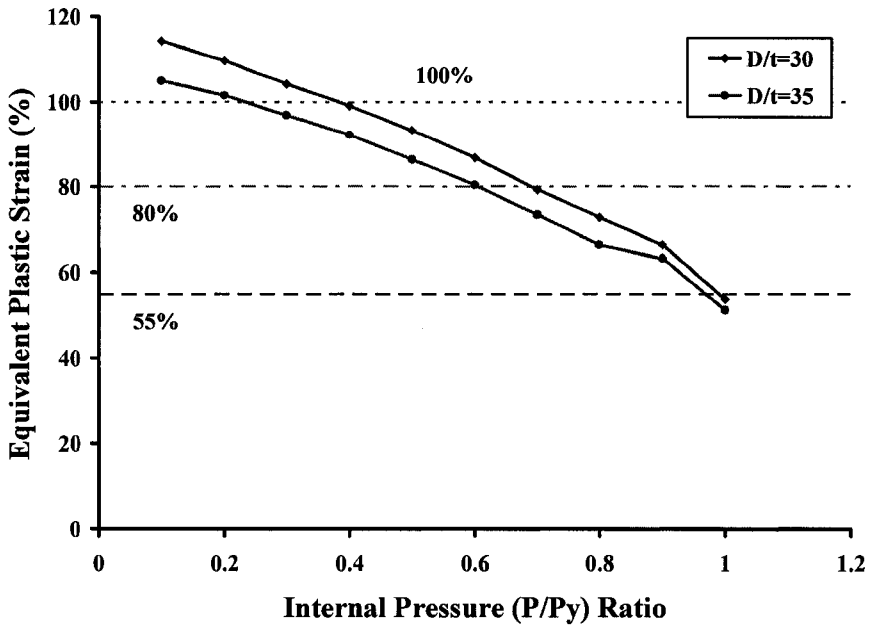

Figure 6.27 Equivalent Plastic Strain vs. Internal Pressure (P/Py) Ratio for D/t=30 and 35 Specimens

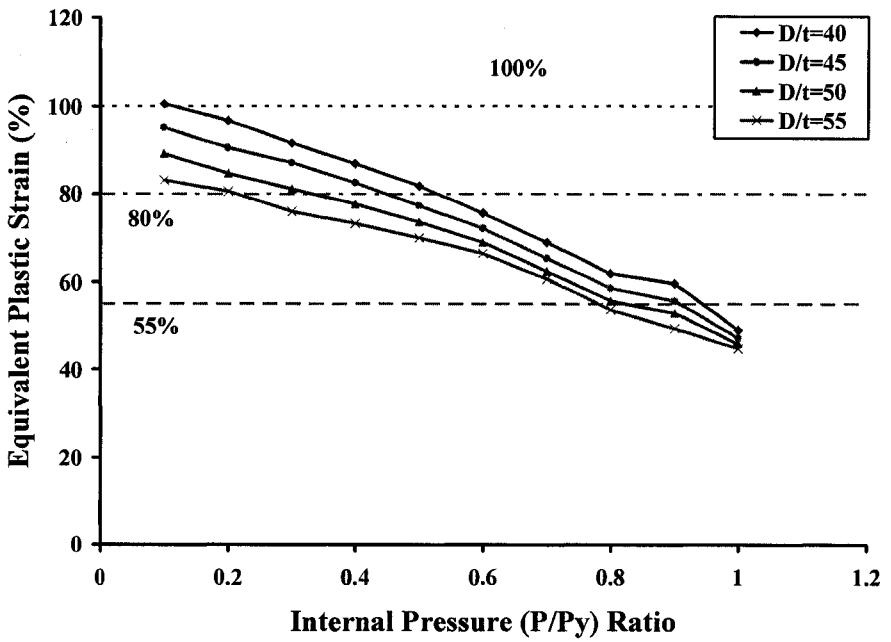

Figure 6.28 Equivalent Plastic Strain vs. Internal Pressure (P/Py) Ratio for D/t=40, 45, 50 and 55 Specimens

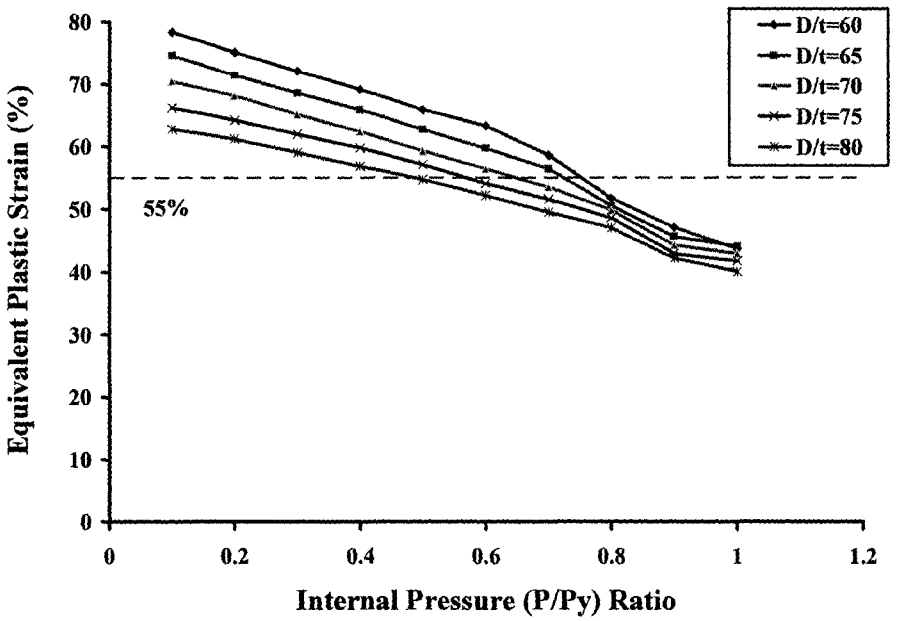

Figure 6.29 Equivalent Plastic Strain vs. Internal Pressure (P/Py) Ratio for D/t=60,65, 70,75and 80 Specimens

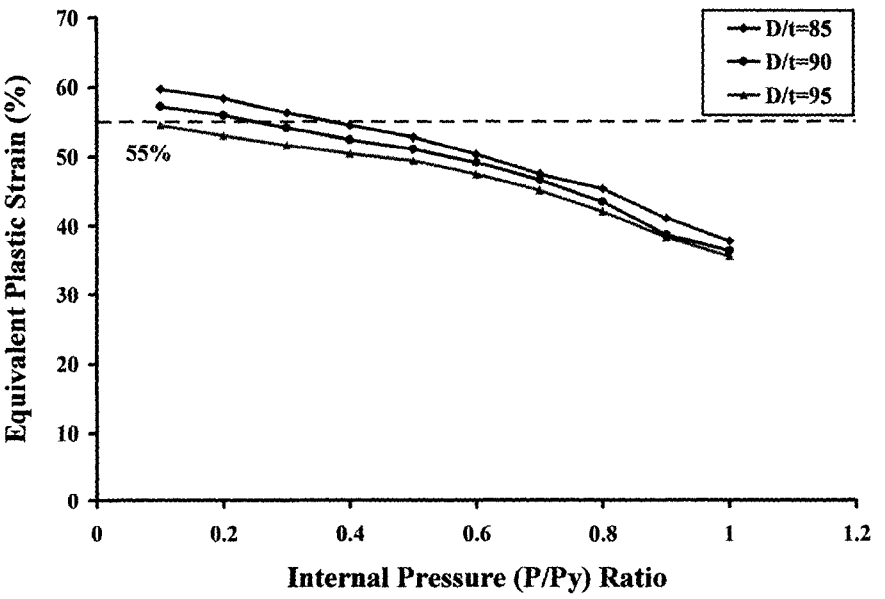

Figure 6.30Equivalent Plastic Strain vs. Internal Pressure (P/Py) Ratio for D/t=85, 90 and 95 Specimens

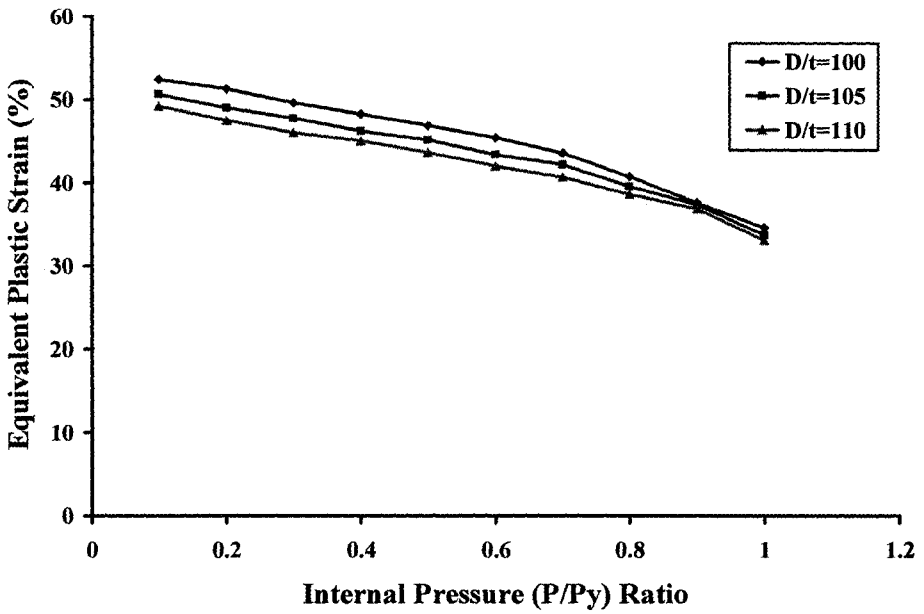

Figure 6.31 Equivalent Plastic Strain vs. Internal Pressure (P/Py) Ratio for D/t=100, 105 and 110 Specimens

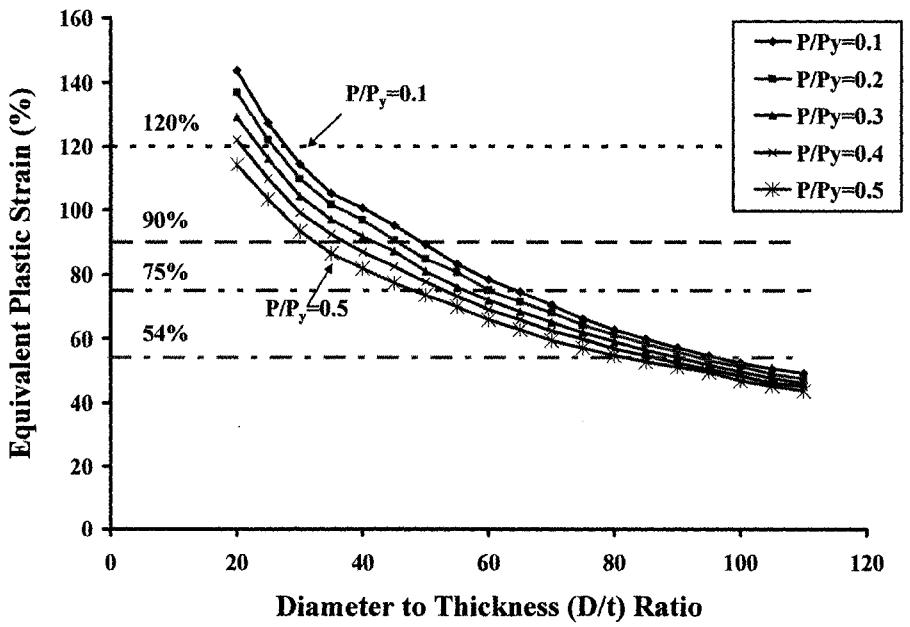

Figure 6.32 Equivalent Plastic Strain vs. Diameter to Thickness (D/t) Ratio for Internal Pressure (P/Py) Ratio = 0.1 to 0.5 Specimens

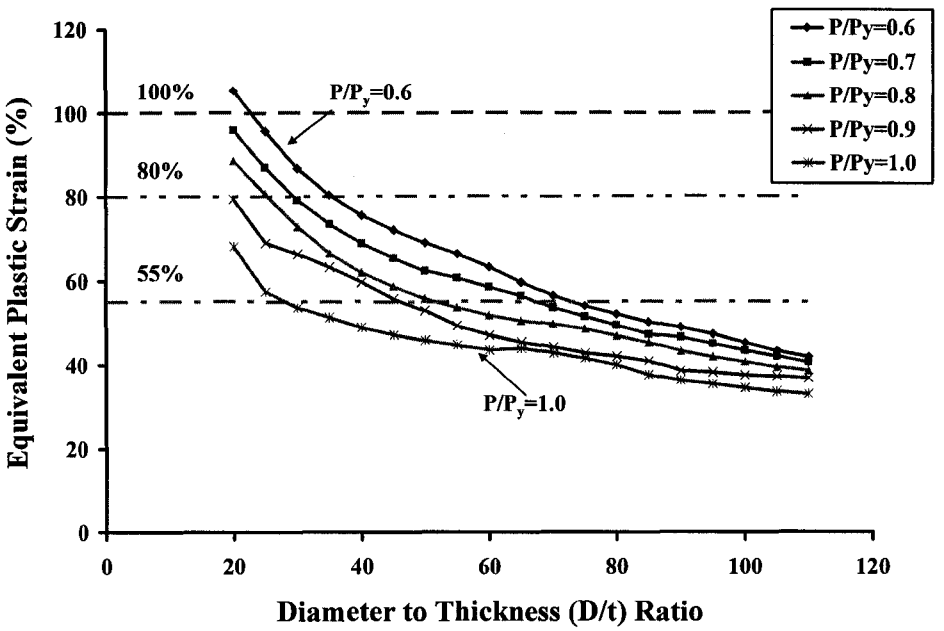

Figure 6.33 Equivalent Plastic Strain vs. Diameter to Thickness (D/t) Ratio for Internal Pressure (P/Py) Ratio = 0.5 to 1.0 Specimens

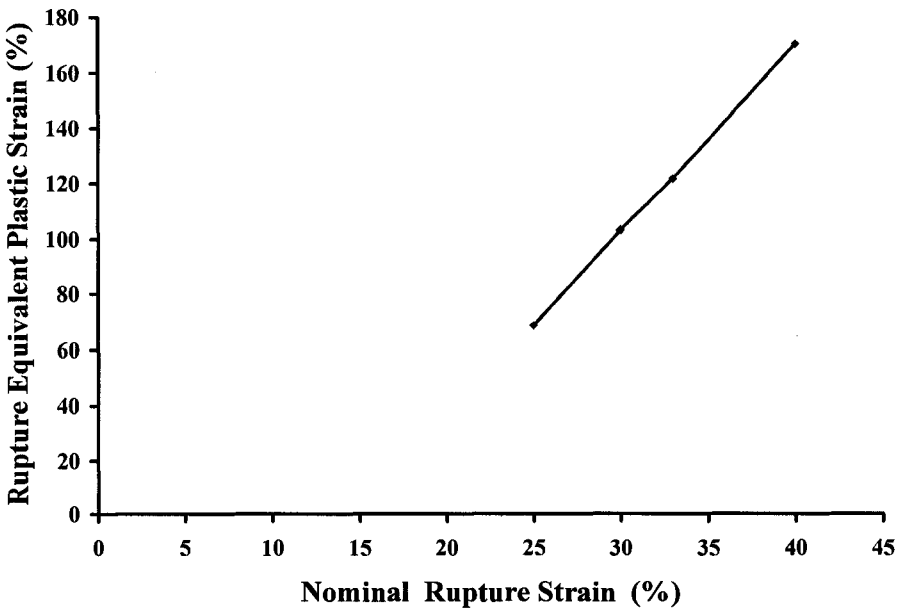

Figure 6.34 Rupture Equivalent Plastic Strain vs. Nominal Rupture Strain for Different Material Models

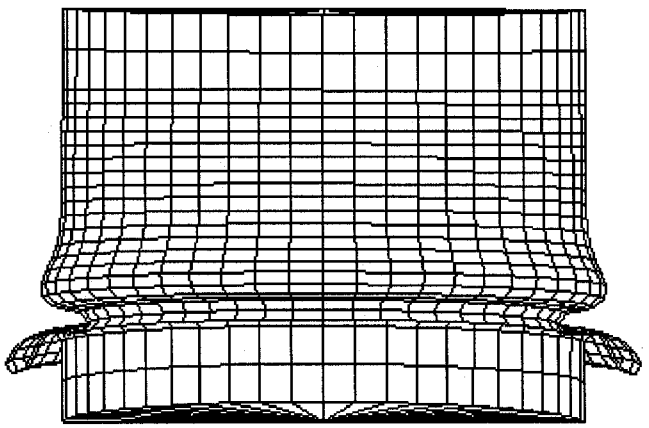

Figure 6.35 One Example of Reduction in Internal Diameter due to Accordion Type of Wrinkling

7 SUMMARY, CONCLUSIONS AND RECOMMENDATIONS

This chapter summarizes the research and findings, provides conclusions on the work that has been achieved under the scope of the thesis, and recommends further work that is necessary and can be undertaken in future research.

7.1 SUMMARY

The main objective of this project was to determine the dependence of type of failure (accordion type severe wrinkling deformation or rupture in the pipe wall) on the operating internal pressure of the fluid, the *D/t* ratio, and material behavior of pipe steel.

A detailed parametric study using finite element (FE) method was conducted to accomplish the objectives of this research project. General purpose FE codes, ABAQUS/Standard and ABAQUS/Explicit, version 6.6-2 (ABAQUS (2006)) was used for numerical modeling, analyses, and parametric study. The FE models for pipe specimens and coupon (material) specimen were validated using the laboratory test data (Das *et al.* (2002)).

7.2 CONCLUSIONS

Based on the this study, a number of conclusions are drawn.

(j) The pipe specimens exhibited outward bulge type wrinkle even for the lower internal pressure ratio of 0.1. However, effect of zero internal pressure was not included in this study.

(k) The maximum equivalent plastic strain at contact decreases as internal pressure increases if *D/t* ratio is kept unchanged.

(l) The maximum equivalent plastic strain at contact also decreases as *D/t* ratio increases if the lever of internal pressure is not changed.

(m) The material for pipe specimens used in the experimental study is highly ductile. The line pipe made of this material does not fail in rupture for *D/t* ratios higher than 40 when subjected to monotonically increasing axi-symmetric compressive axial deformation. Rather, an accordion type failure with one or multiple winkles is expected to occur.

(n) The same line pipe does not fail in rupture for internal pressure ratio higher than 0.70. Rather, an accordion type failure with one or multiple winkles is expected to occur.

(o) The pipe specimens made of the same material and with *D/t* ratio between 20 and 40, the failure mode depends on the internal pressure.

(p) The pipe specimens made of the same material with internal pressure ratio between 0.1 and 0.70, the failure mode depends on the *D/t* ratio.

(q) The ductility of material has significant influence on modes of failure. Higher the rupture engineering strain (higher the ductility of the material), higher equivalent plastic strain at rupture is expected. As the ductility of pipe material increases, chance of rupture failure mode decreases, and thus the chance accordion type failure mode increases.

(r) The both failure modes (accordion or rupture) should be avoided. The accordion type failure poses maintenance problems for the operating pipeline since the cleaning and inspecting instrument may not be able to pass through. The rupture failure is even more serious problems since a rupture in the field line pipe wall causes integrity and safety of pipe line structure and also creates environmental disaster.

7.3 RECOMMENDATIONS

This study provided a number of significant enhancements toward the objectives of the project. To the best of author's knowledge, this study is the first of its kind and no other similar works have been done. In order to achieve more confidence in the understanding

the behaviors and risk assessment of wrinkled pipes, more research works as follows are recommended.

(a) Collars need to be modeled separately from the actual pipe wall, and hence proper interaction between collar and pipe wall needs to be modeled.

(b) More realistic imperfection may be used to trigger wrinkle formation in the numerical models.

(c) A similar study to determine the influence of material behavior in circumferential and longitudinal directions is necessary.

REFERENCES:

ABAQUS, 2006, "ABAQUS/Standard and ABAQUS/ Explicit Version 6.6-2", ABAQUS, Inc.

ASME B31.4, 2002, "Pipeline transportation system for liquid hydrocarbons and other liquids", American Society of Mechanical Engineering.

ASME B31.8, 2003, "Gas transmission and distribution piping systems", American Society of Mechanical Engineering.

ASTM, 1994, "ASTM Specification A 370-94: Standard Test methods and Definitions for Mechanical Testing of Steel Products." ASTM, March, 1994.

Bai,Y., Igland, R. and Moan, T., 1993, "Tube Collapse nder Combined Pressure, Tension and Bending", Journal of Offshore Mechanics and Arctic Engineering, Volume 3(2), pp.121-129.

Bai, Y. and Hauch, S. 1998, "Analytical Collapse Capacity of Corroded Pipes", Proceedings of ISOPE'98.

Ballet, J. P., Hobbs, R. E, 1992, "Asymmetric Effects of Prop Imperfections on the Upheaval Buckling of Pipelines", Thin-Walled Structures, Vol. 13, No. 5, pp 355-373.

Bathe, K. J., 1996 "Finite Element Procedures", Prentice-Hall, Englewood Cliffs.

Bouwkamp J. G. and Stephen R. M., 1973, "Large Diameter Pipe under Combined Loading", Journal of Transportation Engineering, Vol. 99, No.TE3, pp. 521-536.

Bruschi, R., Monti, P., Bolzoni, G. and Tagliaferri, R. 1995, "Finite Element methods as numerical laboratory for analyzing pipeline response under inter pressure, axial load, bending", proceedings of Offshore Mechanics and Arctic Engineering.

CERI, 2001, "Introduction to the Canadian Oil Sands and Heavy Oil Industries", Canadian Energy Research Institute.

Cook, R. D., 1981, "Concepts and Applications of Finite Element Analysis", Second Edition, John Wiley and Sons, New York.

Crig, W.H., P.W. Rowe, 1981, "Operation of Geotechnical Centrifuge from 1970 to 1979", Geotechnical Testing Journal, No. 4, pp 19-25.

CSA-Z662-03, 2003, "Oil and Gas Pipeline Systems", Canadian Standards Association.

Czyz, Jaroslaw A.; Fraccaroli, Constantino; Sergeant, Alan P., 1996, "Measuring Pipeline Movement in Geotechnical Unstable Area Using Inertial Geometry Pipeline Inspection Pig". ASME 1st International Pipeline Conference, Calgary, June 1996.

Czyz, Jaroslaw A.; Wainselboin, Sergio E., 2003, "Monitoring Pipeline Movement and Its Effect on Pipe Integrity Using Inertial/Caliper In-line Inspection". Rio Pipeline Conference & Exposition.

Das, Sreekanta, Cheng J.J.R. and Murray, D. W., 2002, " Fracture of Wrinkled Energy Pipelines" , Structural Engineering Report No. 247, Department of Civil Engineering, University of Alberta, Edmonton, Canada.

Dinovitzer, A. ;Fred, A.; Lazor, R.; Doblanko, R. 2004 "Development and validation of a pipeline buckle and wrinkle assessment model", Proceedings of the Biennial International Pipeline Conference, IPC, v 2, Proc. of the 5th Biennial Int. Pipeline Conf., p 1219-1228.

Dorey, A.B., Cheng J.J.R. and Murray, D. W., 2002, "Critical Buckling Strains for Energy pipelines", Structural Engineering Report No. 237, Department of Civil Engineering, University of Alberta, Edmonton, Canada.

DVN-OS-F101, 2000, Offshore Standard, "Submarine pipeline system", amended latest in October 2005.

Einsfield, R. A.; Murray, D. W.; Yoosef-Ghodsi, N., 2003, "Buckling analysis of high-temperature pressurized pipelines with soil-structure interaction", Journal of the Brazilian Society of Mechanical Sciences and Engineering, v.25 n.2 Rio de Janeiro abr./jun. 2003

EWI, "Strain-Based Design of Pipelines", Edison Welding Institute Report on Project No. 45892GTH, 2003

Hauch, S; Bai, Y, 1998, "Use of finite element analysis for local buckling design of pipelines", 17th International Conference on Offshore Mechanics and Arctic Engineering (USA), pp. 9, July 1998.

Hauch, S. R. and Bai, Y, 2000, "Bending Moment Capacity of Pipes", Journal of Offshore Mechanics and Arctic Engineering, November 2000, Volume 122, Issue 4, pp. 243-252

Hobbs, Roger E., 1981, "Pipeline buckling caused by axial loads", Journal of Constructional Steel Research ,Volume 1, Issue 2 , January 1981, Pages 2-10.

Hobbs, Roger E., 1984, "In-service buckling of heated pipelines", Journal of Transportation Engineering, ASCE, Vol, 110, P175-189.

Gresnigt, A; van Foeken, R J, 2001, "Local buckling of UOE and seamless steel pipes", ISOPE-2001: Proceedings of the Eleventh (2001) International Offshore and Polar Engineering Conference; pp. 131-142.

Gresnigt, A. M. 1986, "Plastic Design of Buried Steel Pipelines in Settlement Areas", HERON, Vol. 31, No. 4, edited by Stevin-Laboratory and TNO-Institute for Building Materials and Structures.

ISO 13623, 2000, "petroleum and natural gas industries; Pipeline transportation system", International Standard Organization.

Michailides, Phil; Deis, Todd, 1998, "NPS 8 Geopig: Inertial Measurement and Mechanical Caliper Technology", Proceedings of the International Pipeline Conference, IPC, VI, p373-378.

Mohareb, M. ; Alexander, S.D.B., Kulak, G.L.; Elwi, A.; Murray, D.W. 1993, "Laboratory Testing of Line pipe to Determine Deformational Behavior", Proceedings of the International Conference on Offshore Mechanics and Arctic Engineering - OMAE, Vol. V, Pipeline Technology, p109-114.

Mohareb, M. ; Elwi, A. E.; Kulak, G.L.; Elwi, A.; Murray, D.W., 1994, "Deformational behavior of line pipe", Structural Engineering Report No. 202, Department of Civil Engineering, University of Alberta, Edmonton, Canada.

Mohareb, M. ; Kulak, G.L.; Elwi, A.; Murray, D.W. 2001, "Testing and analysis of steel pipe segments", Journal of Transportation Engineering, v 127, n 5, Sep/Oct, 2001, p 408-417.

Moradi, Majid; Craig, William H., 1998, "Centrifuge model simulation of buckling of buried pipelines", Proceedings of the International Conference on Offshore Mechanics and Arctic Engineering - OMAE, OMAE98-3908, 7pp.

Murphy, C and Langner, C, 1985, "Ultimate pipe strength under bending, collapse and fatigue", proceedings of the 4th International Conference on Offshore Mechanics and Arctic Engineering (OMAE) 1985.

Murray, David W., 1997, "Local buckling, strain localization, wrinkling and postbuckling response of line pipe", Engineering Structures, v 19, n 5, May, p 360-371.

Myrholm, B. W., 2001, "Local buckling and fracture behavior of line pipe under cyclic loading", Master of Science Thesis, Structural Engineering, Department of Civil Engineering, University of Alberta, Edmonton, Canada.

Ohata, M., Tanaka, N., Ohamasa, M., and Tooda, M., 1999, "Control of Mechanical Preperties for the Improvement fo Deformability of Structural Components" J. Constr. Steel 7, pp 379-386 (in Japanese).

PCF, 2000, "Canada's Pipelines", Petrolum Communication Foundation.

PESC, 1999, "Distributor Manual-Design and Application Manual", Pipeline Engineering & Supply Co. Ltd, Unite Kingdom.

PD 8010-1: 2004, "Code of Practice for Pipelines, Part 1, Steel pipelines on land", British Standards Institution.

Rice, J. R., 1975, "Continuum Mechanics and Thermodynamics of Plasticity in Relation to Microscale Deformation Mechanisms," Constitutive Equations in Plasticity, Argon, A. S., Editor, MIT Press, Cambridge, Massachusetts.

Sherman D. R., 1976, "Tests of Circular Steel Tubes in Bending", Journal of the Structural Division, Vol. 102, No. ST11, pp 2181-2195.

Smith, Marina Q.; Nicolella, Daniel P.; Waldhart, Christopher J.,1998, "Finite element simulations of wrinkling in large diameter corroded pipes", American Society of Mechanical Engineers, Petroleum Division (Publication) PD, Pipeline Engineering and Operations, 8pp.

Song, Xuejun, 2003, "Numerical solutions for pipeline wrinkling", University of Alberta (Canada).

Souza, L.T.; Murray, D. W., 1999, "Analysis for wrinkling behavior of girth-welded line pipe", Journal of Offshore Mechanics and Arctic Engineering, Vol.121, February 1999, P53-61.

Taylor, N., and Ben Gan, A. 1986, "Submarine pipeline buckling – imperfection studies", Thin-Walled Structure, V.4, PP 295-323.

Taylor, N., Tran, V., 1994, "Prop-Imperfection Subsea Pipelines Buckling", Marine Structure, 6, pp. 325-358.

Taylor, N., Tran, V., 1996, "Experimental and Theoretical Studies in Subsea Pipelines Buckling", Marine Structure, 9, pp. 211-257.

Torselletti, Enrico; Vitali, Luigino; Bruschi, Roberte, 2005, "Bending capacity of girth-welded pipes" Proceedings of the International Conference on Offshore Mechanics and Arctic Engineering - *OMAE*, v 3, p 619-627.

Vitali, L.; Bruchi,R.; Mork K. J.; Levold E., Verley R. 1999, "Hotpipe project:Capacity of pipes subject to internal pressure, axial force and bending moment", Proceedings of the 9th International Offshore and Polar Engineering Conference, Brest, France.

Vitali, Luigino; Bartolini, Lorenzo; Askheim, Dag; Reek, Ralf; Levold, Erik , 2005, "Hotpipe Jl project experimental test and FE analyses", Proceedings of the 24th International Conference on Offshore Mechanics and Arctic Engineering, - OMAE2005, v 3, p 715-729.

Yatabe, Hiroshi; Fukuda, Naoki; Masuda, Tomoki; Masao Toyoda, 2004, "Effect of Material Stress-Strain Behavior and Pipe Geometry on the Deformability of High-Grade Pipelines", Journal of Offshore Mechanics and Arctic Engineering, February 2004, Volume 126, Issue 1, pp. 113-119.

Yoosef-Ghodsi, Nader and Murray, D. W., 2002, " Analysis of Buried Pipelines with Thermal Application", Structural Engineering Report No. 246, Department of Civil Engineering, University of Alberta, Edmonton, Canada.

Yoosef-Ghodsi, Nader; Kulak, G. L; and Murray, D. W., 1994, "Behavior of girth welded line pipe", Structural Engineering Report No. 203, Department of Civil Engineering, University of Alberta, Edmonton, Canada.

Yoosef-Ghodsi, Nader; Kulak, G. L; and Murray, D. W., 1995, " Some test results for wrinkling of girth-welded line pipe", *Proceedings of the International Conference on Offshore Mechanics and Arctic Engineering - OMAE*, Vol. V, Pipeline Technology, p379-388.

Zhou Z, Murray, D. W., 1993, "Numerical Structural Analysis of Buried Pipelines" , Structural Engineering Report No. 181, Department of Civil Engineering, University of Alberta, Edmonton, Canada.

VITA AUCTORIS

1968 Born in October in Changzhou, China

1990 Graduated with B.E. degree from Shanghai Jiao Tong University, China

2004 Enrolled in the Department of Civil and Environmental Engineering in the University of Windsor as a Master of Applied Science candidate